

Contents — E through F

The Chemical Composition of Martian Samples — Final Results from the Pathfinder Alpha Proton X-Ray Spectrometer <i>T. E. Economou, C. N. Foley, and R. N. Clayton</i>	3155
Operation of MRO's High Resolution Imaging Science Experiment (HiRISE): Maximizing Science Participation <i>E. Eliason, C. J. Hansen, A. McEwen, W. A. Delamere, N. Bridges, J. Grant, V. Gulick, K. Herkenhoff, L. Keszthelyi, R. Kirk, M. Mellon, P. Smith, S. Squyres, N. Thomas, and C. Weitz</i>	3212
Detecting Near-Surface Water and Hydrate Minerals on Mars from a Rover, Penetrator, or Borehole: The HYDRA Instrument <i>R. C. Elphic, D. J. Lawrence, W. C. Feldman, R. C. Wiens, R. L. Tokar, K. R. Moore, T. H. Prettyman, and H. O. Funsten</i>	3057
A Novel Approach to Modeling Emissivity and Albedo of the Martian Seasonal Caps <i>J. Eluszkiewicz and T. N. Titus</i>	3046
Spectral and Chemical Characteristics of Lake Superior Banded Iron Formation: Analog for Martian Hematite Outcrops <i>A. Fallacaro and W. Calvin</i>	3067
THEMIS Observations of Pitted Cones in Acidalia Planitia and Cydonia Mensae <i>W. H. Farrand and L. R. Gaddis</i>	3094
The Global Distribution of Near-Surface Hydrogen on Mars <i>W. C. Feldman, T. H. Prettyman, W. V. Boynton, S. W. Squyres, D. L. Bish, R. C. Elphic, H. O. Funsten, D. J. Lawrence, S. Maurice, K. R. Moore, R. L. Tokar, and D. T. Vaniman</i>	3218
Temporal Invariance of Wind Orientations as Recorded by Aeolian Features in Proctor Crater <i>L. K. Fenton, M. I. Richardson, and A. D. Toigo</i>	3267
Characteristics and Distribution of the Mars North Polar Basal Unit <i>K. E. Fishbaugh and J. W. Head III</i>	3137
Mars North Polar Stratigraphy and Implications for Geologic History <i>K. E. Fishbaugh and J. W. Head III</i>	3141
Tungsten Isotopic Compositions of the SNC Meteorites: Further Implications for Early Differentiation History of Mars <i>C. N. Foley, M. Wadhwa, and P. E. Janney</i>	3163
Scenarios to Explain the Formation of Gullies on Mars: Numerical Simulation with a Climate Model <i>F. Forget, N. Mangold, and F. Costard</i>	3192
Buried Impact Basins and the Earliest History of Mars <i>H. V. Frey</i>	3104

THE CHEMICAL COMPOSITION OF MARTIAN SAMPLES—FINAL RESULTS FROM THE PATHFINDER ALPHA PROTON X-RAY SPECTROMETER. T. E. Economou^{1,3}, C. N. Foley², and R. N. Clayton³, ¹Laboratory for Astrophysics and Space Research, University of Chicago, 933 East 56th Street, Chicago, IL 60637, tecon@tecon.uchicago.edu, ²Isotope Geochemistry Laboratory, Department of Geology, The Field Museum, Chicago, IL 60605, ³Enrico Fermi Institute, University of Chicago, Chicago, IL 60637.

Introduction: The Alpha Proton X-ray Spectrometer (APXS) on the Pathfinder mission to Ares Vallis on Mars in July, 1997, provided data that were used to determine the geochemistry and infer the petrology of the rocks and soils at the landing site. The previously reported preliminary X-ray results [1] were based on calibration data before instrumental biases were determined and before a minor instrumental difference between the laboratory and flight instrument was corrected. Also, these preliminary results [1] did not include alpha and proton results. The alpha mode in particular reveals the amounts of carbon and oxygen, important for understanding of the volatile contents of the Pathfinder samples. In order to determine the abundances from the alpha-proton modes, a technique for atmosphere subtraction from the spectra was developed [2]. The flight duplicate has been used to determine the accuracy of analysis under Martian conditions with all three modes of the APXS [2, 3]. We have now finished the re-analysis of all the Pathfinder APXS data, both the alpha-proton and the x-ray modes. Two papers, one on the calibration of the APXS [4] and another one on the final results of the martian samples at the Pathfinder landing site [5], have been written and sent for publication to JGR. This work was also the basis for a Ph.D. degree awarded at the University of Chicago [6].

Pathfinder Chemical Results: Pathfinder sample abundances as now determined by the X-ray mode are listed in table I. The alpha-proton modes yield similar bulk abundances, on a volatile free basis (table II) to the X-ray mode for Pathfinder rocks. However, the alpha-proton mode abundances for soils, on a volatile free basis, are approximately 20 relative % lower than X-ray for iron and approximately 2 relative % higher for silicon. The preferred Pathfinder sample abundances, as determined from all modes, are listed in table III. Similar results to our X-ray values have been obtained independently by analyses of the X-ray mode of the instrument by the group at Mainz [7].

The accuracy of our chemical results is supported by the agreement of the three modes of the instrument for most samples on a volatile-free basis. Since the X-ray mode is the most independent of the three modes, its elemental abundances are used together with the carbon, sodium, and water contents from the alpha-proton joint mode to derive the final preferred bulk sample abundances. These results, normalized to 100%, are listed in table III. The errors listed were derived from the laboratory measurements of accuracy and from counting statistics.

Alpha-Proton Mode Carbon and Oxygen: No carbon is detected in the Pathfinder samples. Therefore, the abundance of sample carbon is below the APXS detection limit of 0.3 wt% [3, 7]. The bulk oxygen determination from the alpha mode has yielded some excessive amounts of oxygen possibly indicating the presence of chemically bound water.

Excess oxygen: The bulk oxygen content of most soils is accounted for by assuming that all iron is in the 3+ oxidation state and all sulfur is in the 6+ oxidation state. In some rocks, however, the oxygen excess remains unaccounted for even if we assume the highest oxidation state for all detected elements. Our ability to detect excess oxygen (above stoichiometry for the measured elements), due to oxygen from water (for which the APXS can not detect H), is illustrated in figures 1 and 2. Clearly there is a significant difference in the spectra within figures 1 and 2 if no sample water is present. Figure 3 shows a typical Pathfinder soil (A-15) which appears to have no excess oxygen, while figure 4 shows a rock (A-17) which appears to have a significant amount of excess oxygen.

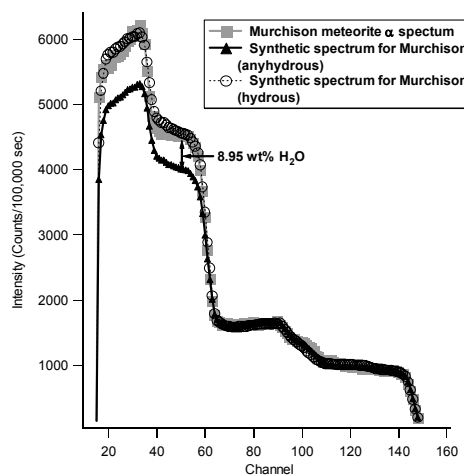


Figure 1

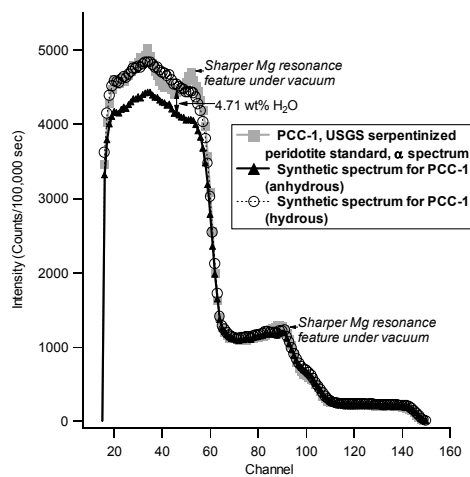


Figure 2

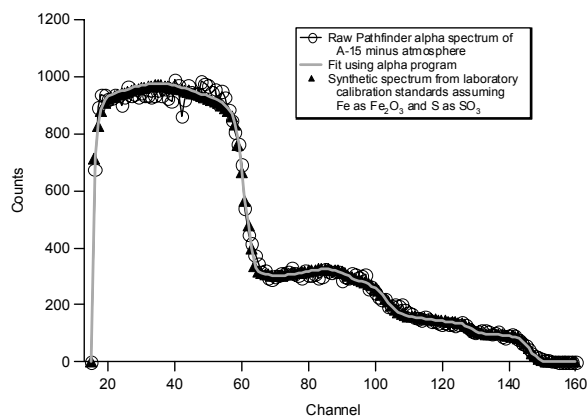


Figure 3

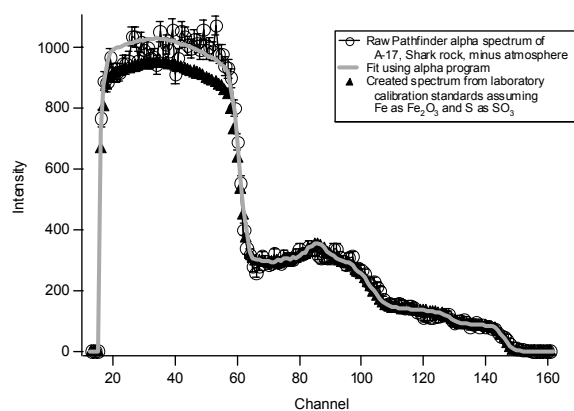


Figure 4

Significant effort went into taking into account all other sources that could contribute to such oxygen excesses in some samples, but none was significant enough to explain it.

Inferred sample-water contents: The excess oxygen detected in some Pathfinder samples cannot then be accounted for by any major rock-forming element measured with the APXS, including carbon and nitrogen, which therefore rules out the presence of detectable carbonate or nitrate. It is probable that this excess oxygen is bound to hydrogen, which is the only major rock-forming element not measured with the APXS. Using the abundances measured from the α mode, the amount of excess oxygen detected can be converted to an amount of mineral-bound water possibly present in the samples with different assumptions of the oxidation states of iron and sulfur as listed in table I. The range of water content for the soils, based on these analyses is between -3.7 ± 1.7 and 0.3 ± 1.7 wt%, (assuming SO_3 and Fe_2O_3). These negative values are closer to zero if some iron is assumed to be in the +2 oxidation state. However, regardless of oxidation state, none of the soil water contents are significantly different from zero. The range of water content for the rocks, assuming SO_3 and FeO , is between 0.1 ± 1.3 and 4.3 ± 1.3 wt. Furthermore, it is the rocks with the least soil-cover which have the most water. This implies that other Pathfinder rocks may also have higher water contents which may be masked by their covering anhydrous soil.

Proton mode in the laboratory: The most important contribution from the proton mode is the more accurate determination of the Pathfinder sodium abundances. This is due to better counting statistics for the proton mode than the alpha or X-ray modes as discussed in more detail by [4, 5, 6]. The proton spectra have several peaks due to (α, p) reactions occurring within samples at different energies for each proton-producing element. The computed and/or measured values for the proton library spectra of Na_2O , MgO , Al_2O_3 , SiO_2 , and S were derived. This proton library consists of the collected intensities from analyzing standards of chemically pure and homogeneous fine-grained simple compounds (NaCl , MgO , Al_2O_3 and SiO_2) and elemental sulfur (figure 5). There is no proton signal from the oxygen within these oxides. The proton intensity is proportional to the concentration of the proton emitters: Na, Mg, Al, Si, and S. The spectrum for Na_2O is computed using the proton spectrum of NaCl for which there is no significant chlorine contribution. The only significant effect of the Martian atmosphere on the proton spectra is to introduce a small contribution from the 2.7% of atmospheric nitrogen. This nitrogen contribution was measured by pointing the APXS toward the Martian sky to measure only atmosphere during a period of comparable atmospheric number density to the Pathfinder sample measurements.

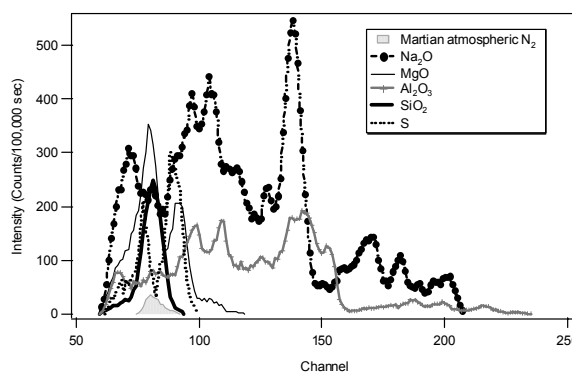


Figure 5

Conclusions: The new chemical analyses derived from the X-ray and α -proton modes yield somewhat different results from the preliminary analyses based on the X-ray mode alone. The final bulk abundances from the X-ray mode are different and include minor element abundances not reported earlier, due to further calibration of the duplicate instrument under Martian conditions. Furthermore, these results include analyses of the α -proton joint mode of the instrument, not reported in the preliminary results.

The new chemical abundances imply that the Pathfinder rocks may have been altered to enhance their water content. It may be useful to compare the water contents acquired by the APXS with those acquired by the gamma-ray and neutron monitors on the Mars Odyssey. Although the instruments determine the water contents within different sample depths, there may be interesting information gathered about surface processes by comparing these data sets.

TABLE I. X-RAY MODE RESULTS ($\pm 1\sigma$).

Soils	Na ₂ O*	MgO	Al ₂ O ₃	SiO ₂	P ₂ O ₅	SO ₃	Cl	K ₂ O	CaO	TiO ₂	Cr ₂ O ₃	MnO	Fe ₂ O ₃
A-2 Deploy	3.2±0.7	8.7±2.0	10.4±0.8	40.9±0.8	0.9±0.2	6.0±1.2	0.7±0.2	0.50±0.04	6.1±0.4	0.7±0.2	0.3±0.1	0.5±0.1	21.2±0.9
A-4 Next to Yogi	3.2±0.7	8.0±1.9	10.6±0.8	41.0±0.9	1.2±0.2	6.9±1.4	0.8±0.2	0.50±0.07	5.6±0.4	1.0±0.3	0.4±0.1	0.4±0.1	20.4±0.8
A-5 Dark Next to Yogi	3.2±0.6	7.1±1.7	10.4±0.8	40.7±0.9	0.6±0.1	5.7±1.1	0.8±0.2	0.50±0.05	6.1±0.4	0.6±0.1	0.5±0.1	0.20±0.06	23.7±1.0
A-9 Disturbed Soil by Scooby	2.6±2.4	6.4±1.6	10.2±0.9	41.7±0.9	0.8±0.2	6.6±1.4	1.2±0.3	0.70±0.09	6.4±0.5	0.8±0.2	0.2±0.1	0.1±0.1	22.2±1.0
A-10 Lamb	1.8±0.7	7.5±1.7	9.8±0.7	41.3±0.9	0.6±0.1	6.4±1.3	0.8±0.2	0.40±0.04	6.0±0.4	0.8±0.2	0.3±0.1	0.4±0.1	24.0±1.0
A-15 Mermaid	2.7±0.8	6.7±1.6	9.9±0.8	43.2±1.0	0.6±0.1	5.2±1.1	0.8±0.2	0.70±0.07	5.5±0.4	0.8±0.2	0.3±0.1	0.3±0.1	23.2±1.0
Indurated													
Soil													
A-8 Scooby Doo	3.1±0.8	6.4±1.5	10.5±0.8	45.0±1.0	0.5±0.1	5.5±1.1	0.9±0.2	0.80±0.06	7.0±0.5	0.7±0.2	0.1±0.1	0.3±0.1	19.1±0.8
Rocks													
A-3 Barnacle	3.2±0.5	2.1±0.5	12.8±0.9	54.1±1.1	0.7±0.1	2.0±0.4	0.5±0.1	1.1±0.07	5.7±0.4	0.6±0.1	0.10±0.04	0.3±0.1	16.7±0.7
A-7 Yogi	4.9±0.8	5.2±1.2	11.2±0.9	47.4±1.1	0.5±0.1	4.4±0.9	0.8±0.2	0.70±0.06	6.6±0.5	0.7±0.2	0.10±0.1	0.4±0.1	17.1±0.7
A-16 Wedge	4.9±0.9	4.1±1.0	11.5±0.8	48.0±1.1	0.6±0.1	3.0±0.6	0.6±0.1	0.80±0.07	6.9±0.5	0.7±0.2	0.00±0.04	0.3±0.1	18.6±0.8
A-17 Shark	3.6±0.8	3.9±1.0	10.7±0.8	53.9±1.2	0.5±0.1	1.7±0.4	0.5±0.1	0.80±0.09	7.7±0.6	0.5±0.2	0.10±0.1	0.4±0.1	15.8±0.7
A-18 Half Dome	4.0±0.7	3.4±0.8	12.3±0.9	50.0±1.1	0.6±0.1	3.0±0.6	0.7±0.2	1.0±0.08	6.0±0.5	0.7±0.2	0.10±0.1	0.4±0.1	17.9±0.7

Key: All X-ray Na₂O* values are calculated from α -proton mode Na₂O/SiO₂ values except for A-9, disturbed soil by Scooby Doo, which is derived from X-ray. Errors are the statistical and laboratory combined error, at the 1 σ level. Sulfur is assumed to have +6 oxidation state because of its high abundance, and because of the Viking soil analyses which support this oxidation state [8]. Fe is assumed to have +3 oxidation state in the soils and +2 oxidation state in the rocks based on

IMP (Imager for Mars Pathfinder) red/blue ratios which indicate more oxidized iron in the soils than the rocks [9].

TABLE II. ALPHA/PROTON MODE RESULTS ($\pm 1\sigma$).

Soils	Na ₂ O	MgO*	Al ₂ O ₃ *	SiO ₂	P ₂ O ₅ *	SO ₃ *	Cl*	K ₂ O*	CaO	TiO ₂ *	Cr ₂ O ₃ *	MnO*	Fe ₂ O ₃	O [†]
A-2 Deploy	3.2±0.9	8.8±2.1	10.6±0.9	41.7±1.3	1.0±0.2	6.1±1.2	0.7±0.2	0.5±0.1	6.5±0.5	0.6±0.2	0.3±0.1	0.5±0.1	20.3±2.5	-0.8±1.5
A-4 Next to Yogi	3.3±0.8	8.2±1.9	10.8±0.9	42.0±1.3	1.2±0.2	7.1±1.5	0.8±0.2	0.6±0.1	6.7±0.5	0.9±0.3	0.3±0.1	0.4±0.1	18.8±2.3	-1.1±1.5
A-5 Dark Next to Yogi	3.5±0.8	7.9±1.9	11.6±1.0	45.4±1.4	0.6±0.1	6.4±1.3	0.9±0.2	0.4±0.1	5.0±0.4	0.5±0.1	0.4±0.1	0.1±0.1	20.6±2.5	-3.5±1.5
A-10 Lamb	1.9±0.7	7.9±1.9	10.3±0.9	43.6±1.6	0.7±0.1	6.6±1.4	0.9±0.2	0.5±0.1	7.8±0.8	0.6±0.2	0.2±0.1	0.3±0.1	18.6±2.3	0.1±1.6
A-15 Mermaid	2.8±0.9	7.0±1.6	10.3±0.9	44.7±1.4	0.6±0.1	5.4±1.1	0.8±0.2	1.0±0.2	7.9±0.7	0.7±0.2	0.3±0.1	0.3±0.1	19.5±2.4	-1.2±1.4
Indurated														
Soil														
A-8 Scooby Doo	3.1±0.9	6.4±1.5	10.5±0.9	45.3±1.6	0.5±0.1	5.4±1.1	0.8±0.2	0.9±0.1	7.8±0.7	0.7±0.2	0.10±0.05	0.3±0.1	17.4±2.2	0.7±1.4
Rocks														
A-3 Barnacle	3.1±0.6	2.1±0.5	12.5±1.0	52.5±1.7	0.7±0.1	1.9±0.4	0.5±0.1	1.1±0.1	5.6±0.4	0.7±0.2	0.10±0.05	0.4±0.1	18.8±2.3	0.2±1.2
A-7 Yogi	4.6±1.0	4.9±1.2	10.6±0.9	44.6±1.4	0.5±0.1	4.2±0.9	0.7±0.2	0.8±0.1	7.9±0.7	0.7±0.2	0.10±0.05	0.4±0.1	17.1±2.1	2.9±1.3
A-16 Wedge	4.7±1.1	3.9±0.9	11.0±0.9	46.1±1.5	0.5±0.1	3.0±0.6	0.6±0.1	0.9±0.1	8.2±0.7	0.7±0.2	0.00±0.05	0.3±0.1	18.7±2.3	1.2±1.2
A-17 Shark	3.3±0.9	3.6±0.9	9.9±0.8	50.0±1.6	0.4±0.1	1.6±0.4	0.5±0.1	0.9±0.1	8.5±0.7	0.6±0.2	0.10±0.10	0.4±0.1	16.4±2.0	3.7±1.2
A-18 Half Dome	3.9±0.8	3.3±0.8	12.0±1.0	48.7±1.5	0.6±0.1	3.0±0.6	0.6±0.1	1.3±0.2	8.1±0.8	0.7±0.2	0.05±0.07	0.4±0.1	17.3±2.1	-0.1±1.2

Key: *Oxides or elements are values determined from X-ray ratios of Mg/Si, Al/Si, P/Si, S/Si, Cl/Si, K/Ca, Ti/Fe, Cr/Fe, and Mn/Fe. Na₂O, SiO₂, CaO, Fe₂O₃ or FeO, and O[†] are those measured independently with the α -proton mode. O[†] is the residual oxygen from the measured total oxygen minus the assumed stoichiometrically bound oxygen as listed. Errors are the statistical and laboratory combined error, at the 1 σ level. Sulfur is assumed to have +6 oxidation state because of its high abundance, and because of the Viking soil analyses which support this oxidation state [8]. Fe is assumed to have +3 oxidation state in the soils and +2 oxidation state in the rocks based on IMP (Imager for Mars Pathfinder) red/blue ratios which indicate more oxidized iron in the soils than the rocks [9].

TABLE III. PREFERRED BULK CHEMICAL ABUNDANCES (α , X-RAY, PROTON) FOR ALL ELEMENTS WITHIN PATHFINDER SAMPLES BASED UPON X-RAY RESULTS NORMALIZED TO CONTAIN THE WATER CONTENT INFERRED FROM THE ALPHA-PROTON MODE.

Soils	H ₂ O	Na ₂ O*	MgO	Al ₂ O ₃	SiO ₂	P ₂ O ₅	SO ₃	Cl	K ₂ O	CaO	TiO ₂	Cr ₂ O ₃	MnO	Fe ₂ O ₃
A-2 Deploy	-	3.2±0.7	8.7±2.0	10.4±0.8	40.9±0.8	0.9±0.2	6.0±1.2	0.7±0.2	0.50±0.04	6.1±0.4	0.7±0.2	0.3±0.1	0.5±0.1	21.2±0.9
A-4 Next to Yogi	-	3.2±0.7	8.0±1.9	10.6±0.8	41.0±0.9	1.2±0.2	6.9±1.4	0.8±0.2	0.50±0.07	5.6±0.4	1.0±0.3	0.4±0.1	0.4±0.1	20.4±0.8
A-5 Dark	-	3.3±0.7	7.3±1.6	10.6±0.8	41.7±0.9	0.6±0.1	5.8±1.1	0.8±0.2	0.5±0.05	6.2±0.4	0.6±0.1	0.5±0.1	0.2±0.1	21.8±1.0
Next to Yogi**														
A-9 Disturbed Soil by Scooby	n.d.	2.6±2.4	6.4±1.6	10.2±0.9	41.7±0.9	0.8±0.2	6.6±1.4	1.2±0.3	0.70±0.09	6.4±0.5	0.8±0.2	0.2±0.1	0.1±0.1	22.2±1.0
A-10 Lamb	0.3±1.7	1.8±0.8	7.5±1.7	9.7±0.7	41.2±0.9	0.6±0.1	6.3±1.2	0.8±0.2	0.4±0.04	6.0±0.4	0.8±0.2	0.3±0.1	0.4±0.1	23.9±1.0
A-15 Mermaid	-	2.7±0.8	6.7±1.6	9.9±0.8	43.2±1.0	0.6±0.1	5.2±1.1	0.8±0.2	0.70±0.07	5.5±0.4	0.8±0.2	0.3±0.1	0.3±0.1	23.2±1.0
Indurated														
Soil														
A-8 Scooby Doo	1.0±1.6	3.1±0.8	6.3±1.5	10.4±0.7	44.6±1.0	0.5±0.1	5.4±1.1	0.9±0.2	0.8±0.1	6.9±0.5	0.7±0.2	0.1±0.1	0.3±0.1	18.9±0.8
Rocks														
A-3 Barnacle	0.3±1.3	3.2±0.5	2.1±0.5	12.8±0.9	53.9±1.1	0.7±0.1	2.0±0.4	0.5±0.1	1.1±0.1	5.7±0.4	0.6±0.1	0.1±0.04	0.3±0.1	16.7±0.7
A-7 Yogi	3.4±1.4	4.7±0.8	5.1±1.2	10.8±0.8	45.7±1.0	0.5±0.1	4.3±0.9	0.7±0.2	0.7±0.1	6.3±0.5	0.7±0.2	0.1±0.1	0.4±0.1	16.5±0.7
A-16 Wedge	1.5±1.5	4.8±1.0	4.0±0.9	11.3±0.8	47.2±1.0	0.5±0.1	3.0±0.6	0.6±0.1	0.8±0.1	6.8±0.5	0.7±0.2	0.0±0.04	0.3±0.1	18.3±0.7
A-17 Shark	4.3±1.3	3.4±0.8	3.7±0.9	10.2±0.8	51.5±1.2	0.4±0.1	1.6±0.4	0.5±0.1	0.8±0.1	7.3±0.5	0.5±0.2	0.1±0.1	0.4±0.1	15.1±0.6
A-18 Half Dome	0.1±1.3	4.0±0.7	3.4±0.8	12.3±0.9	50.0±1.1	0.6±0.1	3.0±0.6	0.7±0.1	1.0±0.1	6.0±0.5	0.7±0.2	0.1±0.1	0.4±0.1	17.9±0.7

Key: All X-ray Na₂O* values are calculated from α -proton mode Na₂O/SiO₂·H₂O values listed as (-) are those which are negative (by a magnitude similar to the total water 1 σ error), and are therefore assumed to be zero. A-9 H₂O abundance was not calculated because it was measured at a significantly greater distance.

Errors are the combined statistical and laboratory error, at the 1 σ level. **Dark Yogi Soil Fe is assumed to be in the +2 oxidation state because of the large negative value obtained for “excess oxygen” when it is assumed to be in the 3+ state.

References: [1] Rieder R., H. Wänke, T. Economou, and A. Turkevich (1997), *J. Geophys. Res.* **102**: No. E2, 4027-4044. [2] Foley, C. N., T. E. Economou, and R. N. Clayton (2001), *LPSC XXXII*, abstract #1979. [3] Foley, C. N., T. E. Economou, and R. N. Clayton (2002), *LPSC XXXIII*, abstract #2073. [4] Foley, C. N., T. E. Economou, and R. N. Clayton (2002), *Submitted for publication to JGR Planets*. [5] Foley, C. N., T. E. Economou, and R. N. Clayton (2002), *Submitted for*

publication to JGR Planets. [6] Foley, C. N., (2002) *Ph.D. Dissertation, University of Chicago*. [7] Wänke, H., J. Brückner, G. Dreibus, R. Rieder, and I. Ryabchikov (2001), *Space Sci. Rev.* **96**, 317-330. [8] Toulmin et al. (1977), *J. Geophys. Res.* **82**, 4625-4634. [9] McSween et al. (1999), *J. Geophys. Res.* **104**: No.E4,8679-8715.

OPERATION OF MRO'S HIGH RESOLUTION IMAGING SCIENCE EXPERIMENT (HiRISE): MAXIMIZING SCIENCE PARTICIPATION. E. Eliason¹, C. J. Hansen², A. McEwen³, W.A. Delamere⁴, N. Bridges², J. Grant⁵, V. Gulick⁶, K. Herkenhoff¹, L. Keszthelyi¹, R. Kirk¹, M. Mellon⁷, P. Smith³, S. Squyres⁸, N. Thomas⁹, and C. Weitz¹⁰. ¹USGS, ²JPL, ³LPL, University of Arizona, ⁴Ball Aerospace and Tech. Corp., ⁵CEPS, Smithsonian Ins., ⁶NASA Ames/SETI, ⁷University of Colorado, ⁸Cornell University, ⁹University of Bern, Switzerland, ¹⁰PSI/NASA

Introduction: Science return from the Mars Reconnaissance Orbiter (MRO) High Resolution Imaging Science Experiment (HiRISE) will be optimized by maximizing science participation in the experiment. MRO is expected to arrive at Mars in March 2006, and the primary science phase begins near the end of 2006 after aerobraking (6 months) and a transition phase. The primary science phase lasts for almost 2 Earth years, followed by a 2-year relay phase in which science observations by MRO are expected to continue.

We expect to acquire ~10,000 images with HiRISE over the course of MRO's two earth-year mission. HiRISE can acquire images with a ground sampling dimension of as little as 30 cm (from a typical altitude of 300 km), in up to 3 colors, and many targets will be re-imaged for stereo [1, 2]. With such high spatial resolution, the percent coverage of Mars will be very limited in spite of the relatively high data rate of MRO (~10x greater than MGS or Odyssey). We expect to cover ~1% of Mars at ~1m/pixel or better, ~0.1% at full resolution, and ~0.05% in color or in stereo. Therefore, the placement of each HiRISE image must be carefully considered in order to maximize the scientific return from MRO.

We believe that every observation should be the result of a mini research project based on pre-existing datasets. During operations, we will need a large database of carefully researched "suggested" observations to select from. The HiRISE team is dedicated to involving the broad Mars community in creating this database, to the fullest degree that is both practical and legal. The philosophy of the team and the design of the ground data system are geared to enabling community involvement. A key aspect of this is that image data will be made available to the planetary community for science analysis as quickly as possible to encourage feedback and new ideas for targets.

Selection of targets: In order to make sure that the best possible targets are imaged, the HiRISE Co-Investigators (Co-I's) will take on responsibility for a particular science theme (e.g. volcanism, fluvial processes, polar geology, etc). For each theme, key issues will be identified along with the particular targets that could advance our understanding of Mars if imaged at high resolution. The Co-I in charge of a given theme will evaluate and prioritize suggested targets from the

community, then advocate these targets through the sequence planning process. Workshops in conjunction with large science meetings will be held to facilitate science community input.

The community will be invited to propose image investigations that address our understanding of processes on Mars. The web portal to the data base of potential HiRISE targets will be open to the community for their direct input. This software, "HiWEB," will be based on the successful "Marsoweb" site developed for the '03 Mars Exploration Rovers' landing site evaluation. A scientist will be able to input the suggested target coordinates and describe their objectives. Potential landing site targets will be supplied by Mars Exploration Program representatives to the project, also via a process that solicits input from the science community.

Operations Concept: The operation concept features scientists monitoring the entire uplink planning process. Co-I's will make sure that the big picture view of what we're trying to learn about Mars is present in every decision, including prioritization of targets, resource negotiations, and optimization of the camera configuration. They will be assisted by operations staff knowledgeable about the software tools used to plan command sequences, and camera and spacecraft limitations. The targeting tool, named "HiPLAN," is based on the JMARS tool developed by Mars Odyssey's THEMIS team to target THEMIS images.

The MRO spacecraft is nominally pointed nadir, but may be maneuvered up to 30 degrees off-nadir to acquire a target. The Context Imager (CTX) and CRISM instruments will also have desired targets. The MRO Project Scientist, working with scientists from each team and representatives from the Mars Exploration Program, will plan timelines of all off-nadir images approximately 3 weeks ahead of their acquisition. Updates to the ephemeris will be used to adjust the actual off-nadir angle and timing. Co-I's will take turns participating in this process to advocate investigations and to work with CTX and CRISM on joint investigations.

Nadir targets of opportunity will be planned ~1 week before acquisition. These are selected by the rotating Co-I from the data base of suggested observations. The camera has a number of configuration parameters [2] which will be set by the Co-I based on the science

requirements associated with a given image, the atmospheric opacity of Mars, and the data volume available.

In the same distributed operations architecture used by Mars Global Surveyor and Odyssey, MRO science teams will operate their instruments from their home institutions. The Operations Center (HiROC) in Tucson, Arizona, will be the hub of uplink planning and downlink data processing. The vision for HiROC is shown in Figure 1. Requests for targets come in from the Co-I's, outside scientists, scientists from other MRO instrument teams, and the general public (filtered through NASA Quest, [3]) via HiWEB and are stored in the "HiCAT" target data base. The actual orbits on

which targets will be imaged are planned using HiPLAN. A final piece of software, "HiCOMMAND," is used to format instrument commands for uplink to the spacecraft.

Closure of the loop is also illustrated in Figure 1, showing the routing of data and reporting back through HiCAT. HiWEB will be used to access acquired images. This is designed deliberately to encourage and facilitate the incorporation of feedback into the planning process, again underscoring our philosophy that each image should be viewed as a mini-research effort, potentially leading to new avenues of investigation.

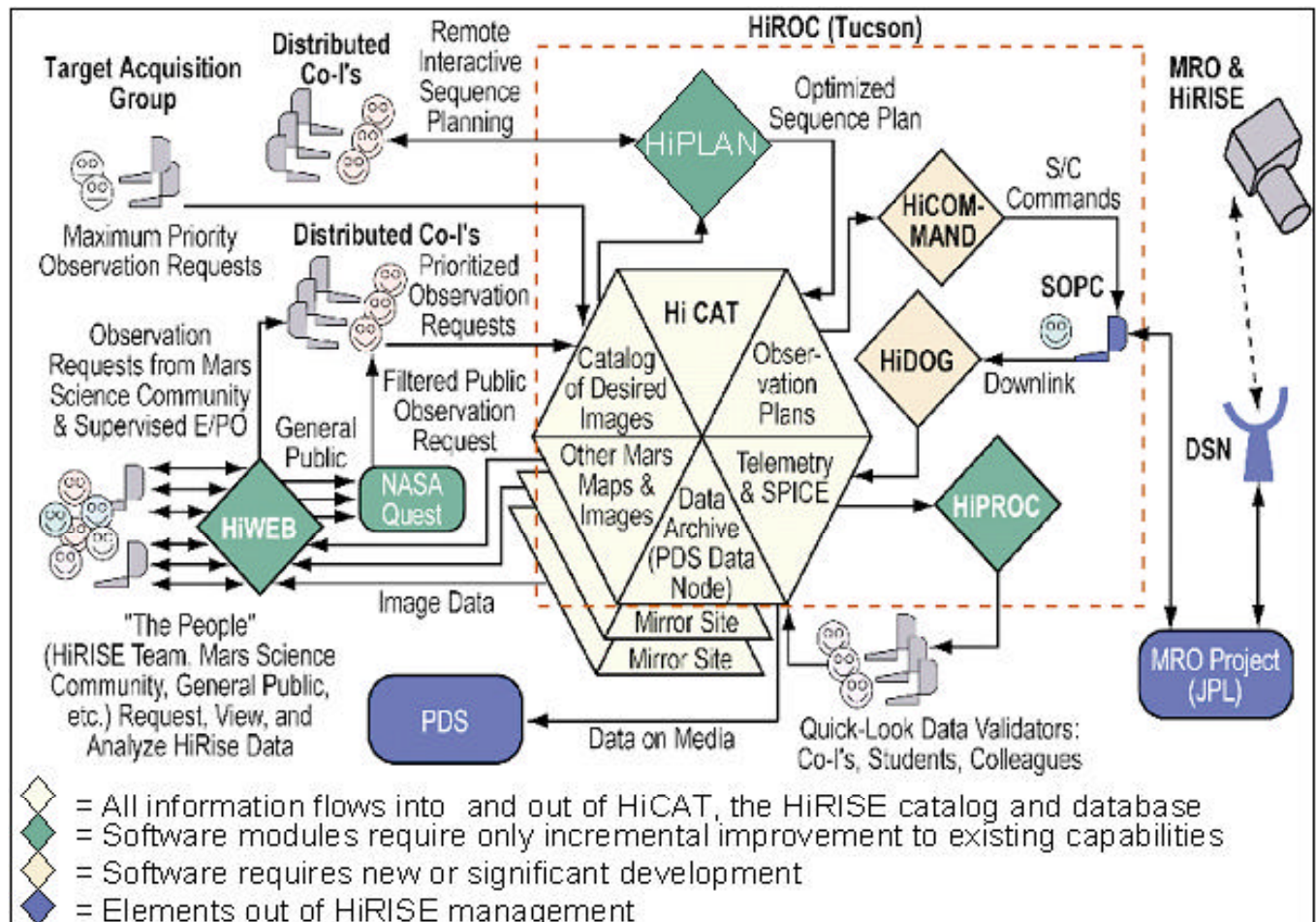


Figure 1 – HiRISE Ground Operations System designed to optimize Mars science, exploration, and E/PO. Observations can be requested and images viewed by anyone via the user-friendly web interface, HiWEB. Co-Is will plan observation sequences with HiPLAN, and instrument commands generated by HiCOMMAND will be sent to the secure Science Operations and Planning Computer (SOPC) for uplink to the spacecraft. Images returned from the spacecraft flow back through the downlink organizer (HiCAT) and are stored in the HiCAT database via a dedicated line to the MRO Operations Center at JPL. The images are processed by the HiPROC procedure and checked by student validators and others to verify processing results. The processed and validated images will be made available to scientists through HiWEB. Periodic deliveries of the HiRISE standard data products are provided to the PDS on hard media.

Image Processing: The goal of the data processing system is to provide timely access to the imaging and to keep up with the high volume (minimum of 9.1 Tb) of instrument data expected to be collected over the nominal two year primary science phase (PSP). To meet this goal HiROC will employ automated event-driven methods for downloading and processing HiRISE instrument science data. The data processing begins when the downlink organizer, "HiDOG" (Figure 1), retrieves instrument data from the MRO operations center at JPL and delivers it to HiCAT. "HiPROC," the automated processing engine, will decompress the data if compressed by the onboard FELICS compressor [4], perform radiometric and geometric processing, and format data products according to PDS standards [5].

Raw spacecraft images (EDRs) will be created within days of the telemetry reaching the ground. The output of each CCD detector array is stored as an individual EDR file resulting in as many as 14 EDR files per observation depending on how many CCD detectors were commanded to operate. Data processing staff will visually validate the EDR products to identify problem images and potential instrument performance problems.

The radiometric calibration process normalizes for global camera operational modes, corrects for the variable sensitivity across the CCD detector arrays, and converts pixel values to radiometric units. The result is an "ideal" image where pixel values are proportional to scene brightness.

The geometric processing applied to HiRISE imaging will depend on the instrument's pixel binning modes [2] used in an observation. Image observations with no pixel binning, offering the highest resolution capability of the instrument, are vulnerable to the effects of spacecraft jitter requiring an analysis (see below) to improve the instrument pointing history and model the point-spread function (PSF).

Processing on Binned Imaging: HiPROC will create radiometrically corrected geometrically processed images (RDRs) of the binned images within several weeks of data acquisition. The geometric processing includes correcting camera optical distortion and transformation from spacecraft viewing coordinates to map coordinates. Because of the minimal effects from spacecraft jitter on binned imaging, the geometric processing will use the mission-produced reconstructed spacecraft navigation and instrument pointing data to model the observation's viewing geometry. Three-color observations are processed to create color registered images using the blue-green, panchromatic red, and

NIR filter data. The RDR color products will be scaled to the largest binning mode used in the color observation (typically the blue-green and NIR filter imaging will be binned).

Processing on Full-Resolution Imaging: With the instrument's 1 microradian instantaneous field-of-view, the full-resolution (unbinned) imaging is sensitive to spacecraft jitter resulting from the spacecraft's reaction wheel rotation and other moving parts. High-frequency spacecraft jitter broadens the PSF and reduces spatial resolution. Lower frequency spacecraft jitter distorts the image geometry. We have been exploring methods for internally characterizing the jitter effects on imaging. The CCD layout on the detector array [2] allows for 48-pixel overlap among adjacent detectors in the orbit cross-track direction. In the down-track direction the CCDs are offset by different amounts ranging from 608 (the minimum offset) to 640 lines. Ground features in the image data can be correlated between the 48-pixel overlapping pairs or triplets of CCDs to characterize the divergence between actual and predicted spacecraft motion. Based on the spacecraft jitter analysis a more accurate model of the instrument pointing history can be constructed to improve the geometric processing. The high-frequency component of the jitter analysis is used to construct a varying PSF model throughout an observation. The PSF model is used to perform image sharpening through an adaptive PSF deconvolution.

The Integrated Software for Imagers and Spectrometers (ISIS) [6] will be used for image processing and analysis. ISIS offers image analysis, cartographic processing and mosaicking capabilities, control to geodetic networks, and data archive preparation tools (see URL: <http://www.flag.wr.usgs.gov/isis-bin/isis.cgi>). The HiRISE processing capabilities added to ISIS will be freely available to the science community through periodic distribution of ISIS, allowing scientists to perform specialized cartographic and image processing on HiRISE data at their home institutions.

Data Products: The standard data products produced by the team will be the EDR and binned RDR products (panchromatic and color). The standard data products will be made available to the general science community within weeks of data acquisition through HiWEB's data distribution capability and periodically delivered to NASA's permanent archiving institution. The standard data products do not rely on specialized processing techniques, such as jitter analysis and adaptive point-spread function deconvolution, that may require intensive work by an image processing analyst.

Special Data Products: The special data products produced by the team will include full-resolution RDR products (panchromatic and color) and Digital Elevation Models (DEMs) generated by application of digital photogrammetric methods applied to stereo-pair imaging. Special data products will be created on a limited basis to support landing site assessment and analysis of observations of special interest.

Full-Resolution DEMs and registered ortho-mosaics will be produced using a Leica commercial digital photogrammetric workstation and the SOCET SET® software system. The automatic terrain extraction software uses multi-resolution area-based correlation to generate DEMs from stereo images in batch mode. An interactive process allows analysts to view images, find correlation errors, and edit the DEM model. For full-resolution images the DEM models are expected to have horizontal resolution of ~1.5 m and vertical precision of ~0.2 meter.

PDS Delivery: The MRO Project requires instrument teams to maintain an updated dataset of the best version of data until meaningful changes in data calibration no longer occur and support the timely processing and distribution of data including their final deposition to the permanent archive facility at the Planetary

Data System (PDS) [7]. The distribution of data products to the PDS will be coordinated through the Project's Data Archive Working Group (DARWG) made up of representatives from the MRO project, science payload teams, and the PDS. The DARWG provides the oversight for data product preparation, acceptance, validation and delivery to the archive facility. PDS deliveries of HiRISE EDR products start 6 months from the beginning of PSP and 12 months for RDR products. Subsequent deliveries occur at 3 month intervals. The later delivery schedule for RDR products is intended to allow the team to refine the instrument's radiometric and geometric camera models using in-orbit Mars observation data.

References: [1] McEwen, A. this conference. [2] Delamere, W. A. this conference. [3] Gulick, V. this conference. [4] Howard, P.G. and J.S. Vitter (1993) *Proc. Data Compression Conference*, J.A. Storer & M. Cohn, eds., Snowbird, Utah, 351-360. [5] Planetary Data System Standards Reference (2002) JPL Document D-7669. [6] Eliason, E.M. (1997) LPS XXVIII, 331-332. [7] McMahon, S.K. (1996) *Planetary and Space Sciences*, 44,1, 3-11.

DETECTING NEAR-SURFACE WATER AND HYDRATE MINERALS ON MARS FROM A ROVER, PENETRATOR, OR BOREHOLE: THE HYDRA INSTRUMENT. R. C. Elphic¹, D. J. Lawrence¹, W. C. Feldman¹, R. C. Wiens¹, R. L. Tokar¹, K. R. Moore¹, T. H. Prettyman¹, H. O. Funsten¹, ¹Los Alamos National Laboratory, MS D466, NIS-1, Los Alamos, NM, 87545, USA (relphic@lanl.gov)

1. Introduction: One of the major goals of near term NASA Mars exploration is to identify exact locations of near-surface water or hydrated minerals on Mars. Evidence for the existence of recent near-surface water on Mars [1] underscores the need for developing instrumentation that can identify water or hydrated minerals very near the surface. Further encouraging evidence of surface and near-surface water and hydrate minerals on Mars comes from neutron spectrometer measurements aboard Mars Odyssey. Preliminary results show very large regions of high hydrogen content poleward of 60° latitude, as well as interesting features closer to the equator [2]. However, spatial resolution from orbit is very poor, ~400 km. The next logical step is to use in-situ or near-surface investigations to map in detail some of the most interesting features. Relatively simple instrumentation based on ³He gas proportional counters were shown to be highly successful on the Lunar Prospector mission in identifying even low levels of enhanced hydrogen abundances [3,4,5].

Here we discuss “HYDRA,” a water- and hydrate-sensing instrument currently being developed under the NASA Mars Instrument Development Program (MIDP). HYDRA is based on Lunar Prospector technology, and is intended as a rover body-mounted instrument, or an instrument on an aerobot, penetrator, hard lander on the surface of Mars, or for borehole stratigraphy applications. Our proposed instrument would be ideal for such platforms as it would be small (<7 cm diameter by 10 cm long), low mass (<500 g), low power (< 1W), and have a low data volume per measurement. We use neutron spectrometry (a) because of its proven ability to uniquely detect and quantify hydrogen abundance, and (b) because the resources required by this approach (weight, power, size, telemetry bandwidth, and measurement time) are extremely low. This compact neutron spectrometer package, comprised of two small ³He gas proportional counters, offers superior sensitivity, extensive flight heritage, and inherent ruggedness. These tubes have survived ~1500 g’s of acceleration in penetrator tests.

In a landed application, HYDRA would help address many topics of interest to the Mars Exploration and Astrobiology communities: (a) nature and origin of stratified deposits; (b) water cycle(s) and temporal changes; (c) early water — oceans, aquifers, precipitation; (d) current extent/location/state of water; (e) polar cap processes and temporal changes; (f) where extre-

meophiles could survive on Mars; (g) paleoclimate — surface signatures and modeling; (h) strategies for future Mars exploration.

2. Science Background: Liquid water is considered to be fundamentally important for the genesis, nurture and sustenance of life. Evidence is mounting that Mars still has near-surface groundwater activity. Though very water-poor by terrestrial igneous standards, the SNC meteorites were found to contain evaporite minerals suggestive of groundwater activity within the past 1.3 Ga [6]. Further evidence has been found in the SNC meteorites indicating that Martian magmas carried significant amounts of water to the surface of Mars [7]. In the last few years there has been great interest in surface features indicative of near-surface water [8,9,10,11,12]. Much of this interest was generated by Mars Global Surveyor images of geologically young seepage and outflow channels attributed to liquid water. The sources of these channels were suggested to be only a few hundred meters or less below the surface [1].

Calculations have typically shown that the region equatorward of ~45 - 50° should be dry near the surface, and regions poleward of this latitude should (and apparently do) support near-surface ice in the present climate [13,14]. However, other studies have suggested water might also exist close to the surface near the equator. By considering the effect of recondensation of water vapor as it diffuses to the surface, models predicted the persistence of porous interstitial ice to relatively shallow depths even at the equator [15]. Models are strongly dependent on the thermal inertia of the surface material. For particulate material (soil), predicted depths of the steady-state ice table were as little as ~4 m at the equator on a broad scale. One could easily imagine variations with terrain, thermal inertia, etc. which might cause the depth to be even shallower in localized regions. On the other hand, predicted ice table depths in dense rock are 200 m or more near the equator.

Figure 1 shows a preliminary epithermal neutron count rate map made using data from the LANL-built neutron spectrometer aboard Mars Odyssey. The epithermal flux is inversely related to the concentration of hydrogen (in the form of hydrate minerals or water or both) in the soils and rocks. Dark blue areas are hydrogen rich, red and yellow areas are hydrogen poor. The epithermal flux observed from orbit varies by a large factor over the planet, denoting the huge range of

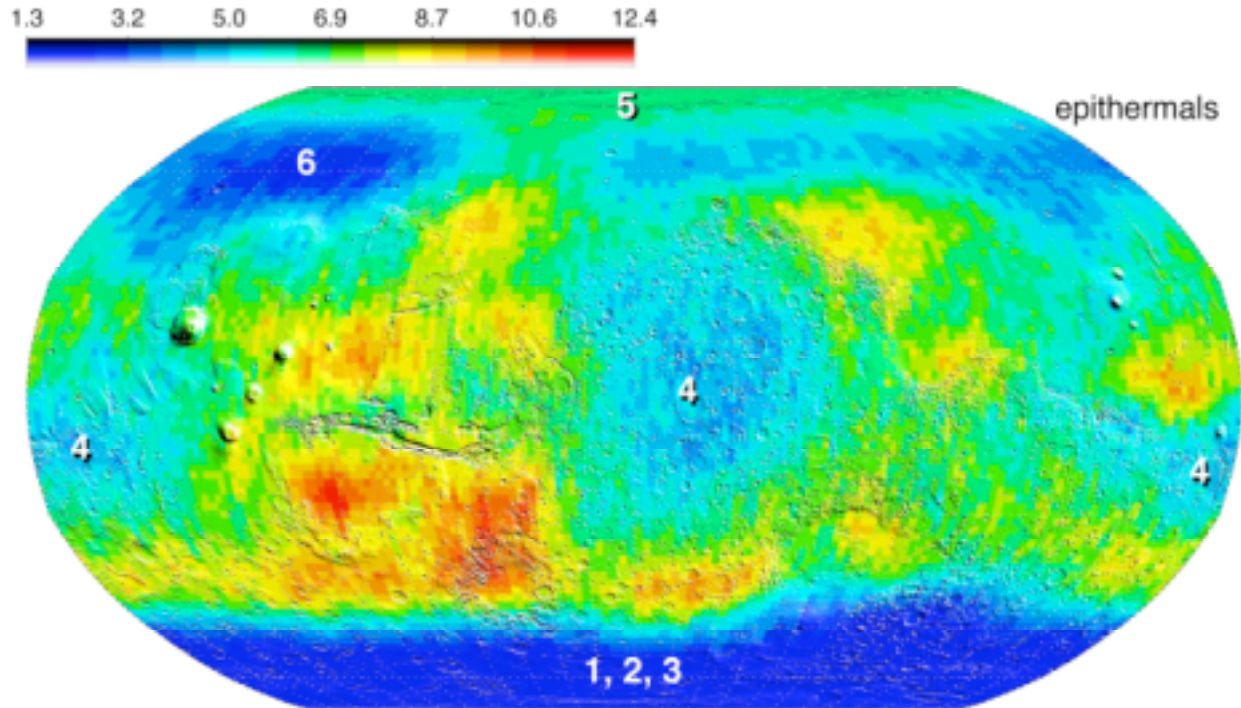


Fig. 1. Mars Odyssey epithermal count rate map for late northern winter at Mars. Low (blue) count rates correspond to regions rich in hydrogen (water), and high (red) count rates denote regions of reduced hydrogen content. Numbers are discussed in the text (see Feldman et al. this conference).

water/hydrate concentrations from location to location. According to [2], several regions can be identified in Figure 1. (1) the region south of -60° latitude is very rich in hydrogen, (2) it is buried beneath a relatively hydrogen-poor overburden, (3) the residual south polar cap is covered by a thick layer of CO_2 , (4) large portions of near-equatorial highlands terrain may contain buried deposits of hydrogen-rich material, (5) the central portion of the north polar cap extending down to about $+60^\circ$ latitude is covered (in northern winter) by a thick layer of CO_2 , (6) the equatorward margins of the north polar cap extending at places down to about $+45^\circ$ latitude contain buried deposits of hydrogen-rich material. Clearly hydrogenous materials at and near the surface of Mars are very prevalent, and hold clues to Mars' past history and present state.

The search for extant or fossil life on Mars will almost certainly concentrate on areas where abundant water is or was present. The identification of sedimentary rocks and in particular, hydrous minerals is of great importance for the astrobiology program. However, our experience so far shows that such an identification is not a simple task. The orbiting Thermal Emission Spectrometer (TES) found evidence for abundant, large-grained hematite in the Sinus Meridiani region [16], suggesting again that liquid water existed at some point on the surface of Mars. However, there is no evidence of hydrated minerals in the

TES spectra. Unfortunately, *actual hydrated minerals are very unlikely to be found close enough to the surface to be revealed by imaging techniques*, given the desiccating effect of the Mars atmosphere and the reactive nature of the Martian soil [17]. Thus, the very minerals of greatest interest (as well as water) will most likely be found only at some depth below the surface. The best way to identify them directly is to drill for them. However, drilling is highly energy- and time-intensive. It is absolutely essential to know a priori where to drill.

An ultracompact neutron spectrometer is the perfect tool to determine the presence of buried hydrate minerals, or water at presently accessible depths, as its depth range is approximately 1 m.

3. Feasibility of Using Neutrons for Water and Hydrate Detection: Planetary neutron spectrometry is most easily carried out on airless or nearly airless bodies because of the large numbers of neutrons that are produced at the surface by energetic galactic cosmic rays (GCR). Specifically, when a planetary body has no or a very thin atmosphere, galactic cosmic rays constantly impinge on the surface and produce high-energy neutrons (~ 10 MeV) through nuclear charge-exchange, knock-on, and spallation reactions. The high-energy neutrons can lose energy either by elastically or inelastically scattering in the planetary material or they can be absorbed by neutron capture reac-

tions. As demonstrated by various simulations and measurements [18,19,20], an equilibrium neutron flux develops which covers over nine orders of magnitude in energy from 0.01 eV to 10 MeV. The equilibrium neutron leakage flux out of the surface is naturally divided into three energy bands: thermal neutrons ($E = 0.01 - 0.4$ eV), epithermal neutrons ($E = 0.4$ eV – 0.5 MeV) and fast neutrons ($E \sim 0.5 - 10$ MeV). For thermal neutrons the dominant reaction is neutron capture and for epithermal neutrons the dominant reaction is energy loss (moderation) from elastic and inelastic scattering. In the presence of hydrogen (i.e., hydrated minerals or water), elastic scattering is an extremely efficient energy loss mechanism for epithermal neutrons. Enhanced hydrogen abundances lead to a large decrease (up to nearly two orders of magnitude) of the epithermal neutron flux from otherwise dry soil. Second-order epithermal flux variations can be caused by neutron capture reactions, but are tracked with the thermal neutron flux which is dominated by the neutron capture reactions.

The technique of using thermal and epithermal neutrons to detect hydrogen abundances on a planetary surface was first demonstrated with the Lunar Prospector Neutron Spectrometer (LP-NS) [3]. Orbital neutron spectrometers are also being used to measure hydrogen abundances on Mars (Mars Odyssey 2001), Mercury (MESSENGER), and the main belt asteroids Vesta and Ceres (DAWN). The LP-NS used two ^3He gas proportional counters to measure thermal and epithermal neutrons. A ^3He proportional counter works by unambiguously identifying the 765 keV reaction products that are emitted when a neutron is absorbed in the ^3He gas. One counter is wrapped in 0.63 mm of Cd and is sensitive only to epithermal neutrons (Cd absorbs all neutrons having energies less than about 0.4 eV). The other counter is wrapped in 0.63 mm of Sn and is sensitive to both thermal and epithermal neutrons [21]. The epithermal neutron flux is obtained by measuring the count rate in the Cd covered counter and the thermal neutron flux is obtained by measuring the count rate difference between the Sn and Cd covered detectors. While each ^3He tube of the LP-NS was relatively large (5.7 cm diameter by 20 cm length), the physics of thermal and epithermal neutrons permits their detection by very small packages. ^3He proportional counters are routinely made quite small (1.2 cm diameter by 4 cm long) while retaining very simple operational characteristics. For these reasons, ^3He counters make ideal instruments

for use on a rover, penetrator, or other landed Mars application.

3.1 Feasibility of HYDRA on a Rover or Lander:

We have carried out Monte Carlo simulations using MCNPX to determine the neutron signal levels that would be measured by HYDRA over soils of various water contents and at various depths. The MCNPX simulations were carried out for bare Cd and Sn tubes at the soil surface, and for tubes mounted on a rover [22]. The rover is simulated as a 150 kg mass 50x50x50cm in size, consisting of 90% Al and 10% PC board material (60% fiberglass, 40% epoxy). The soil composition was average Pathfinder soil [23]. The ^3He tube sizes for these simulations were 1 cm diameter by 16 cm long. Figure 2 shows the count rate (per minute) of the Cd-covered epithermal neutron detector as a function of both H_2O content and depth of burial of the water. Note first of all that the count rates are substantial, showing that cosmic rays are clearly a sufficient source for neutrons even with a very small detector. The top curve shows that even a 1% H_2O content buried beneath 70 cm of desiccated soil still shows a 10% reduction in the epithermal count rate. Higher water contents at shallower depths produce very marked reductions in count rate. Above ~20 wt% H_2O the sensitivity to actual water concentration saturates. Moreover, from epithermal fluxes alone it is not possible to distinguish between a higher concentration of water buried at a greater depth, or a lower concentration buried at a shallow depth. However, the thermal neutrons (not shown) also respond to the presence of buried water, and help remove the ambiguity. In any case, the HYDRA instrument serves as an effective prospecting tool for rapidly and simply locating hydrates or buried water to depths of many tens of

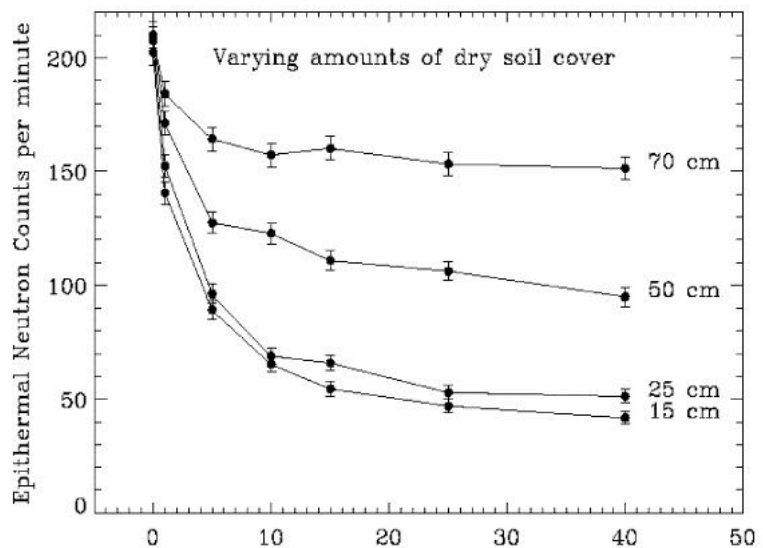


Figure 2. Epithermal neutron count rate for a Cd-covered ^3He tube carried by a rover over buried deposits of different water wt% and burial depths. [22]

centimeters even when the compact instrument is body-mounted on a rover platform.

Rovers or landers powered by an RTG actually enhance HYDRA's water-detection capabilities in the near-surface regions. An RTG provides a steady source of fast (~ 1 MeV) neutrons which penetrate the soil and are moderated by the hydrogen there [24]. Simulations confirm that HYDRA will perform very efficiently in such a configuration, which is promising for future exploration scenarios.

3.2 Feasibility of HYDRA for a Down-Hole Application: HYDRA can be a very sensitive and accurate means of obtaining a depth profile of water, water ice or hydrate minerals. Simulations have been run of the expected epithermal and thermal count rates as a function of depth for several different burial scenarios [25]. Figure 3 shows one set of results: three cases of a layer of 19wt% H₂O about 15 cm thick centered at roughly 17 cm depth, 23 cm depth, and 47 cm depth (all assuming a soil density of 2 g/cm³), and an unlayered soil having 1wt% H₂O (short dashed lines). Both thermal and epithermal neutron count rates are shown assuming ³He tube dimensions of 1 cm x 16 cm and a tube pressure of 10 atm. The thermal neutron count rate (upper left) goes up within the water-rich layer because thermal neutrons are wicked up from neighboring hydrogen-poor materials owing to the reduced scattering length in the hydrogen-rich layer. The epithermal count rates (upper right) drop within the layer because these neutrons are rapidly being downscattered out of the epithermal energy range. Finally, the ratio of thermal to epithermal count rates (lower left)

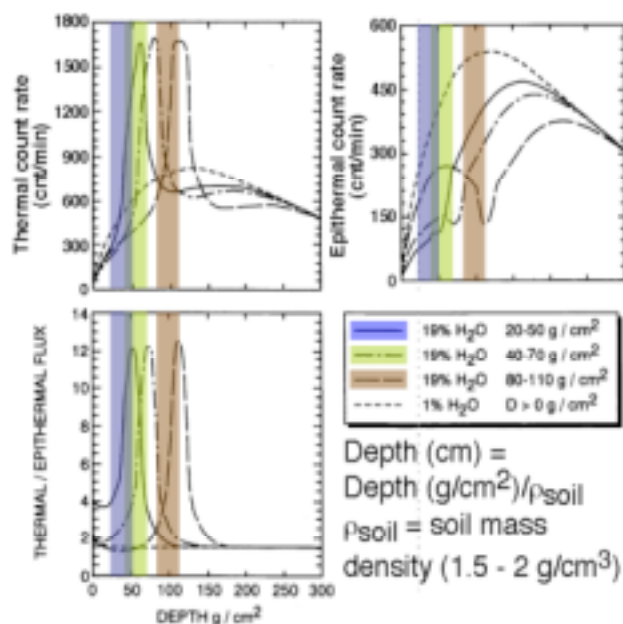


Figure 3. Thermal and epithermal neutron count rate as a function of depth for three H₂O-rich layers buried at different depths. Adapted from [24].

provides a very clear and unambiguous indicator of the depth, thickness, and water abundance in the layer. Consequently, a HYDRA sensor (configured to fit within a drill string segment) placed down a borehole can obtain a depth profile, a stratigraphic sequence of where wet and dry layers are found. This information is useful for sample extraction, providing both a stratigraphic context and promising locations for sample collection. Note that the neutron count rates shown in Figure 3 assume only cosmic rays as the source of neutrons; there is no need for the instrument to carry a neutron generator. In fact, cosmic rays will provide sufficient neutron count rates for useful measurements down to nearly 10 m. HYDRA also lends itself to use with an RTG-powered lander and drill [24].

HYDRA on a rover provides 2-dimensional near-sub-surface water and hydrate prospecting, while HYDRA in the borehole application provides the third dimension of depth.

References: [1] Malin M.C. and Edgett K.S. (2000) *Science* 288, 2330-2335. [2] Feldman, W. C. et al. (2002), *Science*, 10.1126/science.1073541. [3] Feldman, W. C. et al. (1998), *Science*, 281, 1496 – 1500. [4] Feldman, W. C. et al. (2000), *J. Geophys. Res.*, 105, 4175 – 4195. [5] Feldman, et al. (2001), *J. Geophys. Res.*, 106, 23231-23251. [6] Bridges J.C. and Grady M.M. (2000) *Earth Planet. Sci. Lett.* 176, 267-279. [7] McSween H.Y., et al. (2001) *Nature* 409, 487-490. [8] Haberle R.M., et al. (2001) *J. Geophys. Res. Planets*, 106, 23317-23326. [9] Masson P., et al. (2001) *Space Science Reviews* 96, 333-364. [10] Mustard J.F., et al. (2001) *Nature* 412, 411-414. [11] Mellon M.T. and Phillips R.J. (2001) *J. Geophys. Res. Planets* 106, 23165-23179. [12] Baker V.R. (2001) *Nature* 412, 228-236. [13] Mellon M.T. and Jakosky B.M. (1993) *J. Geophys. Res.* 98, 3345-3364. [14] Titus, T. N., et al. (2002), *Science*, 10.1126/SCIENCE.1080497. [15] Mellon M.T., et al. (1997) *J. Geophys. Res.* 102, 19357 – 19369. [16] Christensen, P. R. et al. (2000) *J. Geophys. Res.* 105, 9623-9642. [17] Zent A.P. and McKay C.P. (1994) *Icarus* 108, 146-157. [18] Lingenfelter, R. E. et al. (1961) *J. Geophys. Res.*, 66, #9, 2665 – 2671. [19] Drake, D. M. et al. (1988) *J. Geophys. Res.*, 93, #B6, 6353 – 6368. [20] Maurice, S. et al. (2000) *J. Geophys. Res.*, 105, 20365-20375. [21] Feldman W.C. et al. (2001) *J. Geophys. Res.*, 106, 23231-23251. [22] Lawrence, D. J., et al. (2002), *Lunar Planet. Sci. XXXIII*, abstract #1597 (CDROM). [23] Bruckner et al. (2001) *Lunar and Planet. Sci. XXXII.*, Abstract #1293 (CDROM). [24] Lawrence, D. J. et al., this conference. [25] Feldman, W.C. et al. (1993) *J. Geophys. Res.* 98, 20855-20870.

A NOVEL APPROACH TO MODELING EMISSIVITY AND ALBEDO OF THE MARTIAN SEASONAL CAPS. J. Eluszkiewicz¹ and T. N. Titus², ¹Atmospheric and Environmental Research, Inc., 131 Hartwell Ave., Lexington, MA 02421, jel@aer.com, ²U.S. Geological Survey, 2255 North Gemini Dr., Flagstaff, AZ 86001, ttitus@usgs.gov.

Summary: Initial results from a new model for the emissivity and reflectivity of the martian seasonal caps represented as porous slabs are described. The radiative transfer modeling is linked to a physically based model of CO₂ frost metamorphism. Besides Mars, this coupled radiative transfer/sintering model is applicable to other Solar System bodies where slab-like volatile deposits are likely to be present, including Triton, Pluto, and Io.

Introduction: There is abundant evidence that large portions of the seasonal CO₂ deposits in the polar regions of Mars form a solid slab rather than a fluffy frost. The presence of low-porosity slabs of solid CO₂ was indicated by the early spectroscopic measurements of the caps that suggested long (on the order of 10 cm) path lengths in the 1.5- μ m absorption band of solid CO₂ [1,2]. Unusually long spectroscopic path lengths for portions of the seasonal caps were subsequently inferred from later observations [3,4]. Viking images [5] revealed that the southern residual cap could be distinguished when the seasonal frost was present and that it was always brighter than the brightest areas in the seasonal cap, thus strongly arguing for some degree of transparency in the seasonal deposits. With partially transparent seasonal caps, the albedo contrast between the northern and southern residual caps, invoked to explain the compositional dichotomy between the residual caps (H₂O in the north, CO₂ in the south) [6] could reside in the residual caps. This would make the albedo contrast permanent, whereas in the alternative hypothesis of dust contamination of the overlying seasonal deposits the contrast would be sporadic (e.g., related to the occurrence of dust storms). Furthermore, the penetration of sunlight through a clear CO₂ layer would help to stabilize the compositional dichotomy [7].

The above observations and modeling results led to the conclusion that a semitransparent seasonal CO₂ slab forms on Mars by pressureless sintering [8]. According to this model, the slab is polycrystalline and the long path lengths result from the elimination of voids between crystals. This densification process is driven by the thermodynamic requirement of minimum surface energy and its kinetics is determined by the material properties of solid CO₂, crystal size, and temperature. In addition, circumstances specific to Mars, e.g., the near-absence of an inert gas, low abundance of impuri-

ties, and nearly isothermal conditions, are conducive to the formation of low-density CO₂ deposits. These factors distinguish the CO₂ frost metamorphism on Mars from the snow metamorphism of Earth. On the other hand, CO₂ metamorphism on Mars has many analogs to the N₂ frost metamorphism on Triton [9], where the preponderance of evidence also points out to the presence of semi-transparent seasonal deposits [10-14]. Interestingly, a spectacular phenomenon observed on Triton, the presence of active geysers and dark streaks apparently caused by geyser-like eruptions [15], may have a counterpart on Mars [16]. In both cases, a plausible explanation for these features is offered by a solid-state greenhouse effect occurring in a slab of clear ice [11].

Since 1993, the presence of transparent slabs of solid CO₂ and other results from the sintering model have been supported and/or invoked by numerous studies [17-22]. Most recently, the idea of slab-like CO₂ deposits has been supported by data obtained by instruments onboard the Mars Global Surveyor (MGS) spacecraft. In particular, a densified mean state of the seasonal CO₂ deposits has been inferred from the MOLA and MGS orbital data [23], while very large (up to 1 meter) spectroscopic grain sizes were inferred from analysis of spectra obtained by the Thermal Emission Spectrometer (TES) onboard the spacecraft [24,25]. Slab ice can be distinguished from a porous layer by the shape of the 25- μ m band in the TES spectra, with small band depth BD_{25} indicative of small porosity. BD_{25} is defined as the fractional drop in the measured band radiance relative to the expected blackbody radiance at the brightness temperature of adjacent continua [24]. Two sample TES spectra of the southern seasonal cap with small and large BD_{25} are shown in Figure 1. The interpretation of low values of BD_{25} as indicative of slab-like texture has strong physical basis, with zero BD_{25} corresponding to Fresnel reflection [24]. High BD_{25} 's (i.e., low spectral emissivity) have been identified with small grain sizes [24]. In this work, we will instead relate high BD_{25} to high porosity, an interpretation supported both by experimental data on the emissivity of other materials in various stages of densification [26,27] and by new theoretical calculations presented below.

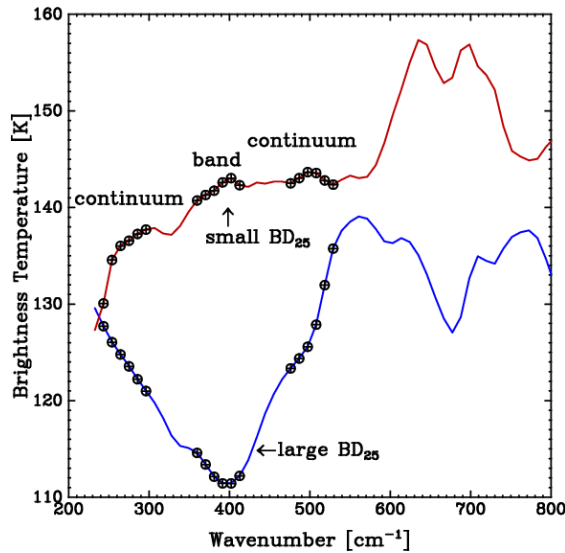


Figure 1: Examples of TES spectra of the southern polar cap. Circles mark spectral locations of channels used to define the 25- μm band (the band itself and two continua). The blue spectrum has low brightness temperatures in the 25- μm band and corresponds to a highly porous deposit. The red spectrum, with a small BD_{25} , corresponds to slab ice.

Texture of Martian Seasonal Caps: The original investigation of the martian CO_2 frost metamorphism [8] only considered densification and led to the conclusion that a slab-like deposit may form on a seasonal timescale provided the frost is sufficiently fine-grained. The TES observations of a CO_2 slab forming essentially simultaneously with deposition in some locations [24], prompted an evaluation of the role played by non-densifying mechanisms in the metamorphism of porous dry ice. The main conclusion from this recent work (and a basic premise of the present study) is that the seasonal CO_2 deposits on Mars rapidly metamorphose into an impermeable slab regardless of the initial grain size. This occurs by the sealing off of the pore space by vapor transport (Kelvin effect). In addition to the TES observations, rapid formation of an impermeable slab is consistent with observations of rapid annealing of microcracks in laboratory samples of dry ice [28,29]. In the laboratory, such rapid annealing leading to the formation of optically clear samples is undoubtedly aided by the favorable geometry of the cracks (crack length \gg crack width). In an assembly of spherical grains, the formation of clear samples is likely to be somewhat slower, but a rapid sealing off of the pore space can be rationalized by a consideration of the timescale for sintering due to the Kelvin effect [30]. This mechanism is driven by the difference in curvatures between the neck and the grain surface and stops

when this difference becomes zero. In an assemblage of spherical grains, this leads to the formation of isolated spherical pores, which happens when $x \approx 0.3a$, where x and a are the neck and grain diameter, respectively [30]. When the rate equation for neck growth [30] is integrated with the material parameters for solid CO_2 at 142 K (including a recent estimate of surface energy [31]), the timescale to reach this condition is on the order of seconds for $a = 1 \mu\text{m}$ and minutes for $a = 10 \mu\text{m}$. Even grains as large as $100 \mu\text{m}$ are likely to develop sealed-off quasi-spherical pores in a matter of hours. It should be emphasized that the Kelvin effect is a non-densifying sintering mechanism that operates in addition to the densifying mechanisms driven by volume and grain-boundary diffusion. Consequently, the slab forming by this mechanism is expected to contain quasi-spherical voids that then undergo slow elimination by the densifying mechanisms. This proposed texture for the martian CO_2 deposits is consistent with the TES and other observations discussed above (in particular, the porous texture of the slab is consistent with the mean density of the seasonal deposits inferred from the MOLA data being less than the theoretical density of solid CO_2) and it has two important consequences for the modeling of the physical properties of the martian seasonal frost. Firstly, the radiative properties of the frost (e.g., albedo and emissivity) are more properly modeled by treating radiative transfer in a slab of solid CO_2 containing spherical voids (and other impurities such as dust grains) rather than by the usual model of spherical CO_2 and dust grains *in vacuo*. In the present study, this problem is tackled by employing the Mie solution for a spherical particle embedded in an absorbing host medium in a multiple scattering code. A second consequence of the impermeability of the slab is the formation of a thermal gradient, which will affect radiative properties of the slab.

Optical Properties of Spherical Particles Embedded in an Absorbing Host Medium: As noted by several authors [32 and references therein], the optical properties of a spherical particle embedded in an absorbing host medium cannot be computed by modifying the refractive indices for the particle and the medium along with scaling the incident wavelength in the input list of the conventional Mie code. Consequently, Yang et al. [32] have considered the general problem when the refractive indices for the particle and the medium have arbitrary values and we rely on their code in the present study. The generalized Mie code can handle both voids and dust particles without difficulty, although a scientific debate continues about the appropriateness of using intrinsic or apparent single scattering properties in multiple scattering calculations [32].

Radiative Transfer in a CO₂ Slab Containing Spherical Voids and Dust Particles: The Mie solution for a spherical particle embedded in an absorbing medium can be applied in a multiple scattering code to compute the radiative properties of the martian CO₂ deposits. In this work, the publicly available DISORT model [33] is used for this purpose. As an example, in Figure 2 we show computed brightness temperatures for an isothermal slab of solid CO₂ at $T = 142$ K containing spherical voids with 1- μm radius (the refractive indices for solid CO₂ are as in [29]). The choice of this rather small value of r is motivated by the analysis of TES data (see below). As can be seen in Figure 2, the spectrum of a highly porous dust-free slab exhibits a deep minimum around 25 μm , qualitatively consistent with the TES spectra of the cold spots (see example in Figure 1). As the porosity ϕ decreases due to densification, the 25- μm band depth BD_{25} decreases, with the brightness temperatures for a nonporous slab approaching the kinetic temperature. Also shown in Figure 2 are spectra computed when, in addition to voids, the slab is assumed to contain 1- μm dust particles with a fractional abundance of 10^{-4} by volume. The dusty spectra have been computed using optical constants for palagonite [34]. In agreement with past investigations [22, 24], the presence of dust reduces the depth of the 25- μm band significantly. The presence of dust is also required to significantly lower the slab albedo. For example, the solar spectral reflectivity of the pure CO₂ slab considered in Figure 2 is close to unity regardless of porosity (except for $\phi \rightarrow 0$, when the slab albedo approaches the albedo of the underlying surface).

While the spectra shown in Figure 2 are similar to the spectra computed by means of the conventional Mie/delta-Eddington approach [35, 22, 24] (which considers spherical particles *in vacuo*), the chief advantage of the present approach is its connection to the microphysical model of the cap texture and, consequently, its predictive capability. In particular, the present model does not require the notion of meter-sized Mie boulders of solid CO₂ in order to explain the low values of BD_{25} seen in the TES spectra, but instead relates low BD_{25} to low porosity. The strong porosity dependence of the computed BD_{25} suggests that the density evolution obtained from the sintering model can be coupled with the radiative transfer calculations to predict the evolution of BD_{25} . To illustrate this point, in Figure 3 we plot the values of BD_{25} computed from the TES spectra of a narrow zonal sector at the southernmost point of the MGS orbit and compare them with the evolution of BD_{25} predicted by the sintering model. BD_{25} is defined as in [24], with band and continuum channels given in Figure 1. The blue lines represent the

evolution computed using the ad-hoc assumption that BD_{25} is inversely proportional to the mean distance \bar{a} between scattering centers and that \bar{a} is, on dimensional grounds, on the order of the ratio (volume)/(internal pore surface area). In the sintering model, this ratio is a weakly nonlinear function of ϕ , with the result that $BD_{25} \sim \phi$. Note that the strong $1/r^{3-4}$ dependence of the densification rate on the grain/void radius [8] provides a stringent constraint on the grain/void size consistent with a seasonal densification timescale. When the volume diffusion coefficient D_v , inferred from NMR measurements [36] is used in the densification equations, the allowable grain/void size is reduced from 10 to about 1 μm as a consequence of a larger activation energy for D_v than assumed previously [8]. This constraint is also of great value in computing the optical properties of the slab. The black and red lines in Figure 3 represent results from the proposed more rigorous approach to the modeling of BD_{25} , in which the evolution of ϕ computed for $r = 1 \mu\text{m}$ is used to predict the evolution of optical depths and single scattering properties used by the DISORT model. Both dust-free and dusty calculations (as in Figure 2) are presented in Figure 3. For the particular case shown in Figure 3, the computed evolution of BD_{25} is quite different from observations when dust is neglected, but even in this case the proposed model is capable of reproducing the end-member cases of high and low BD_{25} for high and low porosity, respectively. The inclusion of 10^{-4} by volume of dust lowers the computed BD_{25} and improves the agreement with observations (except for the drop in the computed BD_{25} near $t = 100$ sols).

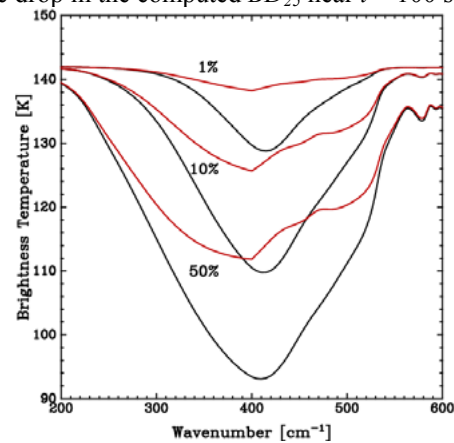


Figure 2: Black curves: spectra of a meter-thick slab of solid CO₂ containing spherical voids with radius 1 μm . The curves are labeled by the value of porosity. These spectra have been computed assuming isothermal conditions at $T = 142$ K. The red lines show corresponding spectra when in addition to voids the slab contains 1- μm dust particles with an abundance of 10^{-4} by volume.

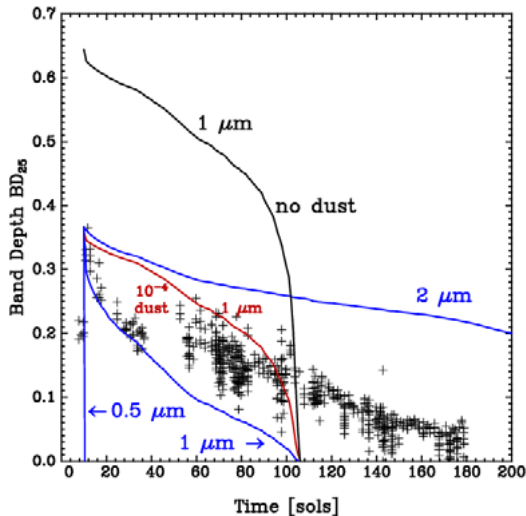


Figure 3: Evolution of BD_{25} in the zonal band $30-40^\circ W$ in the southern polar ring during the first southern winter of the MGS mapping phase (time is counted from $L_s = 107^\circ$). Black dots represent individual spectra. The blue curves represent evolutions of BD_{25} computed using the assumption $BD_{25} \sim \phi$. The black and red curves represent the evolution of BD_{25} computed by coupling the evolution of ϕ to radiative transfer calculations (the black and red curves correspond to dust-free and dusty slabs, respectively). The curves are labeled by the assumed void size r in the sintering model.

In the future, several important factors not considered in the preliminary analysis presented above should be included, some of which could improve the agreement between the proposed model and observations:

- In the above calculations, the slab thickness has been assumed constant at $L = 1$ m. In reality, the slab thickness will change in the course of a season as a result of condensation, densification, and sublimation. In future work, a more realistic approach could be adopted, in which L is constrained by the MOLA data (such as Fig. 2 in [23]). The use of a realistic evolution of L might necessitate a consideration of a non-homogeneous density distribution with depth (with younger frosts being fluffier than older deposits). Deposition of fresh frost is likely to reduce the sharp drop in the computed BD_{25} seen in Figure 3.

- As mentioned above, the void size r strongly affects densification rate. The value of r consistent with observed evolution of BD_{25} is dependent on the adopted value for the volume diffusion coefficient D_v and the sensitivity of the estimated r to the measurement uncertainties in D_v [36], as well as possible changes in r in the course of the densification process need to be evaluated.

- The sealing-off of the pore space will lead to the formation of a thermal gradient. This will affect

radiative transfer in the slab, both directly and by increasing the void size consistent with seasonal densification (with the concomitant effect on the optical properties of the slab).

Implications: The new model presented herein will aid in the analysis of data from instruments employing both remote (visible, infrared, radar) and *in situ* (e.g., drilling) technology. For example, the model of CO_2 surface emissivity could constrain retrievals from nadir-looking IR-sounders over the martian polar regions, in a somewhat analogous manner as models of ocean IR emissivity provide the *a priori* information for retrievals from terrestrial infrared sounders. Moreover, since the radiative properties of the CO_2 deposits exert a strong control on the martian atmosphere, the new model is relevant to meteorological and climate studies of Mars.

Acknowledgements: Dr. Ping Yang of Texas A&M University is thanked for making available the Mie code. This work has been funded in part by the Mars Data Analysis Program.

References: [1] Moroz V. I. (1964) *Sov. Astron.* 8, 273. [2] Kieffer H. (1970) *JGR*, 75, 510. [3] Larson H. P. and U. Fink (1972) *ApJ. Lett.*, 171, 91. [4] Calvin W. M. (1990) *JGR*, 95, 14,743. [5] James P. B. et al. (1979) *JGR*, 84, 2889. [6] Paige D. A. and A. P. Ingersoll (1985) *Science*, 228, 1160. [7] Lindner B. L. (1992) *GRL*, 19, 1675. [8] Eluszkiewicz J. (1993) *Icarus*, 103, 43. [9] Eluszkiewicz J. (1991) *JGR*, 96, 19,217. [10] Cruikshank D. et al. (1984) *Icarus*, 58, 293. [11] Kirk R. L. et al. (1990) *Science*, 250, 424. [12] Moore J. M. and J. R. Spencer (1990) *GRL*, 17, 1757. [13] Helfenstein P. J. et al. (1992) *Science*, 255, 824. [14] Lee P. et al. (1992) *Icarus*, 99, 82. [15] Soderblom L. A. et al. (1990) *Science*, 250, 410. [16] Kieffer, H. H. (2000) *Science*, 289, 1853. [17] Calvin W. M. and T. Z. Martin (1994) *JGR*, 99, 21,143. [18] Butler B. J. (1994) Ph.D. thesis, Caltech. [19] Paige D. A. et al. (1995) *BAAS*, 27, 1098. [20] Forget F. and J. B. Pollack (1995) *JGR*, 101, 16,865. [21] Forget F. et al. (1998) *Icarus*, 131, 302. [22] Hansen G. B. (1999) *JGR*, 104, 16,471. [23] Smith D. E. et al. (2001) *Science*, 294, 2141. [24] Kieffer H. et al. (2000) *JGR*, 105, 9653. [25] Titus T. N. et al. (2001) *JGR*, 106, 23,181. [26] Adissin A. et al. (1977) *Trans. J. Br. Ceram. Soc.*, 76, 17. [27] Markham J. R. et al. (1992) *J. Heat Transfer*, 114, 458. [28] Kieffer H. (1968) Ph.D. thesis, Caltech. [29] Hansen G. B. (1997) *JGR*, 102, 21,569. [30] Swinkels F. B. and M. F. Ashby (1981) *Acta Metall.*, 29, 259. [31] Wood S. E. (1998) Ph. D. thesis, UCLA. [32] Yang P. et al. (2002) *Appl. Opt.*, 41, 2740. [33] Stamnes K. et al. (1988) *Appl. Optics*, 27, 2502. [34] Roush T. et al. (1991) *Icarus*, 94, 191. [35] Warren S. et al. (1990) *JGR*, 95, 14,717. [36] Liu S.-B. et al. (1985) *J. Chem. Phys.*, 81, 6064.

TES spectra. This suggests the presence of oriented grains in the martian hematite outcrops. Recently, *Glotch et al., 2003* [9] studied the effects of precursory mineralogy on hematite spectra and concluded that goethite (FeOOH) that has been dehydroxylated to form hematite (Fe_2O_3) provides the best match to the Sinus Meridiani (SM) hematite spectra. This is one possible formation mechanism among synthetic samples.

Our samples were measured in VNIR/SWIR region by an ASD field spectrometer at the Arthur Brant Laboratory for Exploration Geophysics at the University of Nevada, Reno. The emission spectra were acquired with a Nicolet Nexus 670 FTIR interferometric spectrometer at 4cm^{-1} resolution at Arizona State University [10].

Oxide samples. As noted above, the oxide facies consists mainly of hematite with minor magnetite. The thinly banded hematite that occurs in typical banded iron structure has distinct minima in the VNIR region at 0.65 and $0.85\mu\text{m}$. In the TIR, this hematite shows emission minima at approximately, 300 , 465 , and 550cm^{-1} , matching the SM hematite.

The more metamorphosed hematite with the schistose texture does not show distinct hematite features in the VNIR region. It does however exhibit the same hematite oxide features in the TIR as the banded hematite. These features are two to three times stronger in the schistose samples than in the banded samples. The lack of features in the VNIR region could be due to a substantial amount of magnetite in the sample.



Figure 3. Field photo illustrating gray, crystalline hematite in typical banded iron formation structure. The red bands are chert.



Figure 4. Field photo illustrating more metamorphosed crystalline hematite with a schistose texture.

The magnetite samples have a typical featureless spectrum in the VNIR/SWIR. The TIR spectra are dominated by quartz features most likely from the fine grained chert throughout the sample. Petrographic analysis should reveal how much quartz/chert is present in the sample.

Carbonate samples. The carbonate facies of banded iron formation consists of alternating bands of siderite and chert. The VNIR/SWIR spectra of these samples typically do not show any distinct carbonate features in the 2.3 to $2.5\mu\text{m}$ range, or at most have a weak feature at $2.3\mu\text{m}$. They do have broad $1\mu\text{m}$ bands indicating the ferrous iron component of siderite (FeCO_3). One sample shows weak carbonate features in the TIR at 7 and $11.3\mu\text{m}$. The geochemical analysis to determine how much carbonate is present will be presented at the meeting.

Silicate Sample. The VNIR/SWIR spectra of the silicate sample resembles many of the magnesium (Mg) endmember serpentines [11]. However, the low albedo (10%), and the narrow $0.7\mu\text{m}$ feature indicate a high iron content.

The TIR spectra of the silicate facies exhibit a 500cm^{-1} feature common to many of the Mg endmember serpentines such as clinochore and lizardite, but lack a 600cm^{-1} feature characteristic of these minerals. The features between 1000 and 900cm^{-1} are consistent with the Mg endmember amesite. An odd feature at 1220cm^{-1} has not yet been identified. XRD and petrographic analysis will help identify the mineral composition and will be presented at the meeting.

Resampling. All sample spectra will be resampled to TES and mini-TES resolution using a gaussian convolution approach. At TES resolution, a direct comparison can be made between the SM hematite spectra, and the hematite spectra from the oxide facies of LST BIF. Mini-TES resolution will provide insight for

observations made by the Mars Exploration Rover (MER) at the SM landing site. Samples from the carbonate and silicate facies are examples of possible auxiliary minerals for the martian hematite sites. This spectral data will help constrain the combination of features, identifiable by MER that will be indicative of a BIF like process on Mars.

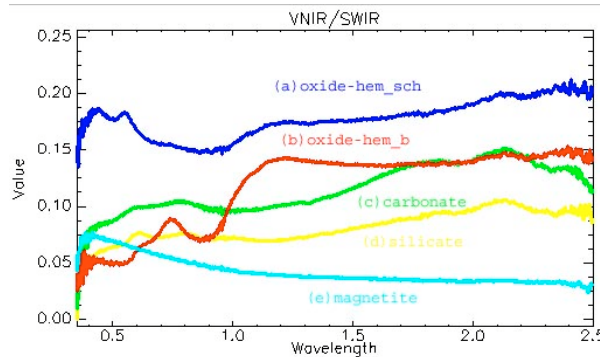


Figure 5. VNIR/SWIR spectra of (a) schistose hematite, (b) typical banded hematite, (c) carbonate, (d) silicate, (e) magnetite.

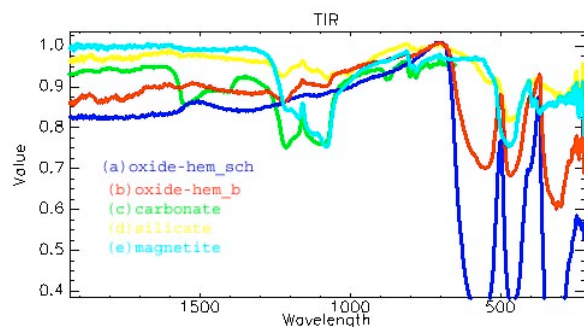


Figure 6. TIR spectra of (a) schistose hematite, (b) typical banded hematite, (c) carbonate, (d) silicate, (e) magnetite.

Geochemistry: Thin sections have been acquired of the samples in order to further constrain the mineralogy. Sample textures should provide further clues to the nature of origin. Electron microprobe and XRD analyses will also be done to obtain elemental percentages that can be related to specific mineral species. These results will be presented at the meeting.

Mars Exploration Rovers: Instruments onboard the MER will examine the SM hematite deposit for composition and texture at a much finer spatial scale. Data from the Mossbauer spectrometer, mini-TES, APXS, and the microscopic imager can be directly compared to our hand samples in order to constrain an origin of the SM hematite.

References: [1] Christensen et al. (2000) *JGR*, 105, E4, 9623-9642. [2] Christensen et al. (2000) *JGR*, 106, E10, 23,873-23,885. [3] Baldridge and Calvin (2003) *in press*. [4] Gross (1983) *Precambrian Research*, 20, 171-187. [5] Trendall (1968) *Geol. Soc. Am. Bull.*, 79, 1527-1544. [6] Trendall (2002) *Spec. Pub. #33 Int. Assoc. Sedimentol.*, 33-66. [7] James (1954) *Econ. Geology*, 49, 235-293. [8] Lane et al. (2002) *JGR*, 107, E12, 9-1 – 9-15. [9] Glotch et al. (2003) *LPS XXXIV*, Abstract #2008. [10] Thanks to Alice Baldridge for her assistance in acquiring spectra. [11] Calvin and King (1997) *Meteoritics & Plan. Sci.*, 32, 693-701.

THEMIS OBSERVATIONS OF PITTED CONES IN ACIDALIA PLANITIA AND CYDONIA MENSÆ.

W. H. Farrand¹ and L. R. Gaddis², ¹Space Science Institute, 3100 Marine St., Suite A353, Boulder, CO 80303, farrand@colorado.edu, ²U.S. Geological Survey, Flagstaff, AZ.

Introduction: Analysis of Viking imagery revealed the presence of large numbers of pitted or cratered cones in the northern plains of Mars with the highest concentrations occurring in eastern Acidalia Planitia and Cydonia Mensæ [1-3]. Based largely on crater/cone diameter ratio comparisons, these features were hypothesized as being analogous to terrestrial pseudocraters (rootless cones) [1-2] such as occur in the Lake Myvatn region of Iceland [4]. Doubts remained about this connection given the disparity in mean diameters between these Martian features (mean diameter of ~600 m [2]) and the Icelandic rootless cones (mean diameter of ~ 50 m [5]). Recent analysis of MOC Narrow Angle camera images of Elysium Planitia, Amazonis Planitia and elsewhere have revealed another class of features with diameters commensurate with the Icelandic rootless cones [5, 6]. If the features in Acidalia and Cydonia are not rootless cones, what are they? Recent information on the thermophysical properties of these features as provided by the Mars Odyssey THEMIS instrument may help to answer this question.

Geologic Setting: Much of Acidalia has been mapped as being covered by the Vastitas Borealis Formation (VBF); the mottled member and knobby member of which were tentatively interpreted as being volcanic in origin [7]. Features in Acidalia have been interpreted as being analogous to features formed by the interaction of volcanoes and ice sheets: tuyas and moberg hills [8,9]. Recently, the VBF has been reinterpreted as the sedimentary residue left from the deposition of sediments and sublimation of water deposited from outflow channels to the south [10]. While there are numerous pitted cones within the VBF, they also occur beyond its boundaries. For example, the present investigation examines numerous pitted cones within Cydonia Mensæ which lies outside the mapped boundaries of the VBF. The VBF is Hesperian in age and is overlain in central Acidalia by a member of the Amazonian-aged Arcadia formation. Acidalia also hosts numerous mesas which have been alternatively interpreted as tuyas [8,9] or as erosional remnants of younger overburden sediments. There are instances where these mesas partially overlie pitted cones. An example of such an occurrence is provided in **Figure 1**.

Observations: The spectral emittance characteristics of the regional deposits that serve as substrates for these pitted cones in Acidalia have been examined

with TES data [11]. Earlier analyses with TES have identified Acidalia as the type locale for the "Surface Type 2" (ST2) dark region cover type [12]. The ST2 spectral signature was originally interpreted as being produced by volcanic products of basaltic andesite to andesite in composition [12]. It has since been suggested to also be explainable as being caused by weathered basalt [13], a higher glass component [14], and palagonite coatings [15]. Analyses by [11] and [16] have indicated that Acidalia has higher fractions of basaltic glass than does the Surface Type 1 type region of Syrtis Major. Higher basaltic glass fractions would be consistent with extensive ice-magma interactions in Acidalia.

THEMIS multispectral infrared and single band visible information was analyzed in this investigation. THEMIS provides 10 Mid-Wave Infrared (MWIR) bands, one of which is in an atmospheric absorption. THEMIS also has a 5 band visible to very near infrared imaging system. Some residual problems remain with some of the THEMIS bands; however, gross spectral differences can be determined. The system is very effective at determining thermophysical properties of the surface. Nighttime brightness temperature images can be used as a proxy for thermal inertia [17]. The locations of the THEMIS scenes discussed here are indicated in **Figure 2**.

Using THEMIS to help determine thermophysical properties of the pitted cones in Acidalia is demonstrated in **Figure 3**, a daytime THEMIS image, and **Figure 4**, a nighttime brightness temperature THEMIS image over approximately the same region in eastern Acidalia very near the border with Cydonia. In the image acquired in the day, the pitted cones appear bright. Because they have positive relief the slopes facing the solar illumination are especially bright (indicating warmest temperatures). In the night image, the pitted cones are very dark. Dark signatures in the brightness temperature image suggests that the cones have a low thermal inertia, and that they are composed of, or mantled by, fine-grained materials.

The east-central Acidalia nighttime brightness temperature image I03390003 (which, at the time of the writing of this abstract, does not have an overlapping daytime THEMIS image) shows remarkable temperature differences both between dark spots (likely pitted cones) and the background and among very bright, irregularly shaped, flow-like features on the surface (**Figure 5**). Irregularly shaped flow-like fea-

tures are also apparent in daytime THEMIS images (**Figure 6**) in which they appear dark. The nature of these flow-like surface units remains to be determined. However, the fact that they are bright in nighttime brightness temperature images and dark in daytime images indicates that they consist of materials which have higher thermal inertia than the surroundings. Also, their apparent proximity to units with pitted cones suggests that their presence may have bearing on the origin of the pitted cones.

Interpretation: The inferred low thermal inertia of the pitted cones is an important clue to their nature. Their apparent low thermal inertia values provide evidence against their possible origin as rootless cones. Rootless cones consist mainly of coarse scoria, are often capped by spatter, and have finer material admixed with scoria blocks on the outer apron [5]. Such spatter and scoria blocks are materials with high thermal inertias. Cinder cones are also formed from coarse scoria which would be higher in thermal inertia than the observed pitted cones. Tuff cones consist of cemented palagonite tuffs which also should produce a relatively high thermal inertia signature. Neither origin as rootless cones nor as cinder cones explains the inferred low thermal values of the pitted cones in Acidalia. These pitted cones have also been hypothesized as being pingoes or mud volcanoes [18]. Both of these landforms are commonly composed of fine grained, poorly to semi-indurated materials which would be consistent with the thermal inertia observations. The presence of the flow-like surface units may be supportive of the mud volcano origin; however, the flow-like units have not been observed to emanate from any pitted cones. Alternatively, the conundrum of mesas partially overlying some cones (**Figure 1**) might be evidence that the features are pingos. Pingos are ice cored domes. Domes of ice have the internal integrity to withstand burial and exhumation. Sublimation of the ice after exhumation would leave a crater and a mantle of the low thermal inertia sediments (which had been admixed with the ice).

References: [1] Frey H. and Jarosewich M. (1982) *JGR*, 87, 9867-9879. [2] Frey H. et al. (1979) *JGR*, 84, 8075-8086. [3] McGill G.E. (2002) *LPS XXXIII*, Abstract #1126. [4] Thorarinsson S. (1953) *Bull. Volc. Ser. 2, 14*, 3-44. [5] Greeley R. and Fagents S.A. (2001) *JGR*, 106, 20527-20546. [6] Lanagan P.D. et al. (2001) *GRL*, 28, 2365-2367. [7] Scott D.H. and Tanaka K.L. (1986) USGS Map I-1802-A. [8] Allen C.C. (1979) *JGR*, 84, 8048-. [9] Hodges and Moore [10] Kreslavsky M.A. and Head J.W. (2002) *JGR*, 107, E12, 4. [11] Farrand W.H. and Gaddis L.R. (2003) *LPS XXXIV*, Abstract #1601. [12] Bandfield J. et al.

(2000) *Science*, 287, 1626-1630. [13] Wyatt M. and McSween H (2002), *Nature* 417, 263-266. [14] Noble S.K. and Pieters C.M. (2001), *LPS XXXIII*, Abstract #1230. [15] Morris R.V. et al. (2003) *LPS XXXIV*, Abstract #1874. [16] Bandfield, J. (2002) *JGR*, 107, 9-1. [17] Fergason and Christensen (2003), *LPS XXXIV*, #1785. [18] Tanaka K.L. (1997) *JGR*, 102, 4131-4149.

Acknowledgements: This work is funded by NASA Office of Space Science Mars Data Analysis Program grant NAG5-10577.



Figure 1. Subsection of MOC narrow angle camera image m1500479. The rightmost of three pitted cones at the bottom of this image is partially overlain by a mesa. Resolution is 4.63 m/pixel.

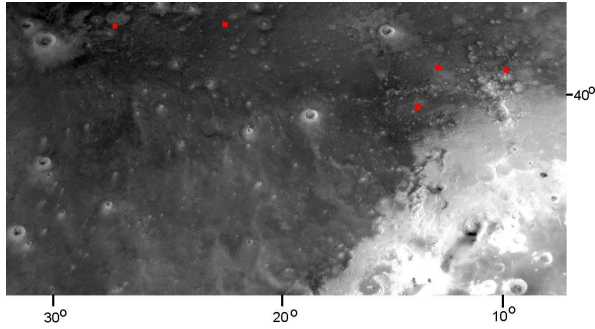


Figure 2. MOC wide angle camera mosaic of central to east Acidalia and Cydonia. Red dots indicate nominal centers of THEMIS scenes shown in **Figures 3–6**.

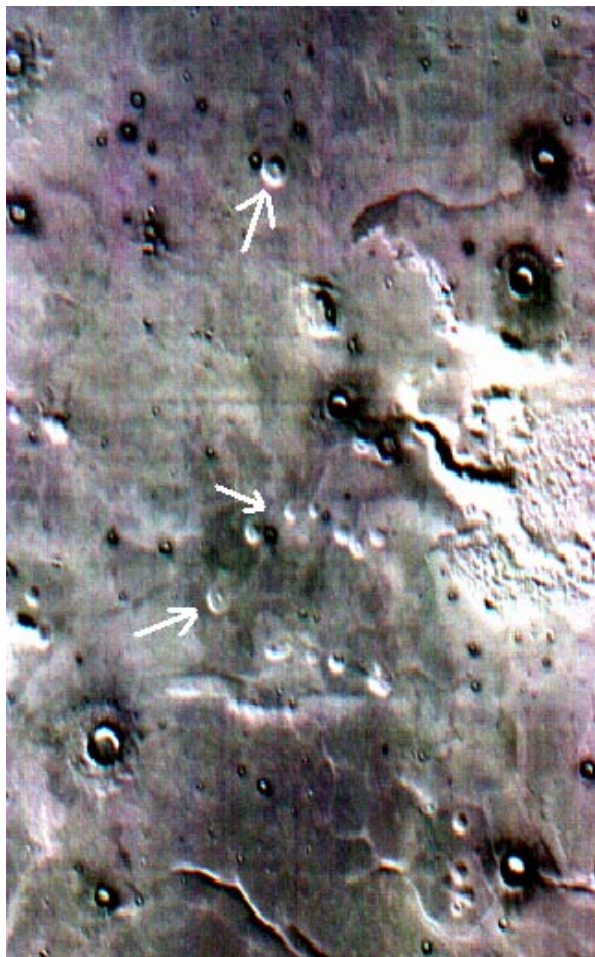


Figure 3. Subsection of THEMIS daytime scene I01461009 band 8, 5, 3 composite. Arrows point to pitted cones. Fresh impact craters with blocky ejecta have dark halos in this image. Solar illumination is from the lower left. North is towards the top. Resolution of the MWIR THEMIS images shown here is 100 m/pixel. THEMIS images shown here are 304 to 320 pixels (30.4 to 32 km) in width.



Figure 4. Subsection of nighttime THEMIS brightness temperature image for scene I01692010 covering approximately the same area as in Figure 1. Arrows point to pitted cones which are very dark indicating low thermal inertia. In contrast blocky ejecta near fresh impact craters are bright in this image.

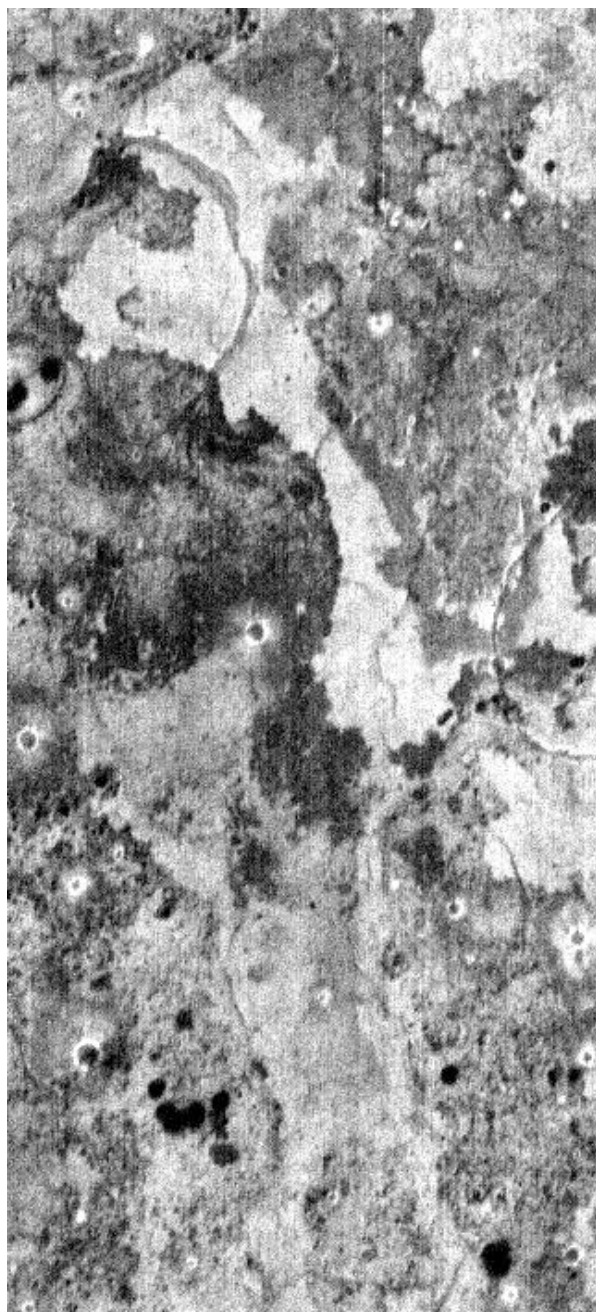


Figure 5. Subsection of nighttime THEMIS image I03390003 showing marked contrast in temperature between dark spots in lower portion of image (assumed pitted cones) and background and among irregularly shaped surface units in upper portion of image.



Figure 6. Dark flow-like surface unit in central Acidalia. The unit is bounded in its upper center portion by grooves and is overlain on the lower left by a field of pitted cones. Image is a subsection of a band 8, 5, 3 composite of THEMIS scene I03284002.

THE GLOBAL DISTRIBUTION OF NEAR-SURFACE HYDROGEN ON MARS. W.C. Feldman¹, T.H. Prettyman¹, W.V. Boynton², S.W. Squyres³, D.L. Bish¹, R.C. Elphic¹, H.O. Funsten¹, D.J. Lawrence¹, S. Maurice⁴, K.R. Moore¹, R.L. Tokar¹, D.T. Vaniman¹, ¹Los Alamos National Laboratory (Los Alamos NM 87545 USA; wfeldman@lanl.gov), ²Lunar and Planetary Laboratory (University of Arizona, Tucson, AZ), ³Cornell University (Ithaca, NY), ⁴Observatoire, Midi-Pyrenees (Toulouse, France)

1. Introduction: Prime objectives of the neutron spectrometer (NS) component of the Gamma-Ray Spectrometer suite of instruments aboard Mars Odyssey are to identify the major reservoirs of hydrogen on Mars, determine their relative contributions to its total water inventory, and estimate the portion of the current inventory that is near the surface. Although more information is required than is currently available, epithermal neutron currents alone can provide a significant lower bound of hydrogen abundances on Mars.

Observations from Viking 1, Viking 2, and Mars Pathfinder positively identified two of these reservoirs. By far the largest near-surface reservoir is comprised of the two residual polar caps, which together are sufficient to cover Mars with a global ocean about 30 m deep [1, 2]. The second is contained in the atmosphere, which if deposited on the surface, would cover Mars with a thin film of water about 10^{-5} m deep [3]. Although negligible in comparison, the fact that an atmospheric reservoir exists shows that it can provide a conduit that couples transient reservoirs of near-surface water ice [4,5].

It has long been speculated that Mars has had, and may still retain, a far larger reservoir of water. Topographic features such as rampart craters, collapsed chaotic terrain, massive outflow channels, and valley networks provide strong support for the past existence of large bodies of surface water [6,1,7,8]. Measurements of the areal size and depth of all paleo-water and volcanic features led to an estimate of a total water inventory equivalent to a global ocean that was between 100 and 500 m thick [1]. Measurements of the D/H ratio have allowed predictions that between 5 and 50 m of this inventory was lost to space [9,10,11,12,13]. Altogether, these estimates lead to between 20 and 465 m of water from the juvenile Martian inventory that is not accounted for.

First analyses of Mars Odyssey neutron and gamma-ray data showed that reservoirs of hydrogen do indeed exist poleward of about $\pm 50^\circ$ latitude [14,15,16,17]. Mars Odyssey neutron observations also revealed a near equatorial hydrogen reservoir [15] that maximizes in Arabia Terra and its antipode. Initial quantitative estimates of hydrogen abundances in these investigations were normalized to an assumed 1% H₂O content by mass for the Viking 1 landing site [18,19]. However, a recent analysis of the seasonal variation of the CO₂ frost cover at the north pole has allowed an independent absolute calibration of the three neutron energy bands measured using the NS aboard Mars Od-

yssey [20,21]. This calibration allows a reinterpretation of neutron fluxes measured globally to provide a lower bound of the hydrogen abundance within about 1 m of the Martian surface. A determination of true hydrogen abundances requires knowledge of the stratigraphy of hydrogen-bearing layers because the presence of an overlying relatively desiccated layer would mask enhanced abundances of a lower layer [20,22].

2. CO₂ Frost-Free Epithermal Neutron Counting Rates: The sensor element of the NS is a segmented cubical block of borated plastic scintillator [23,24]. This design allows measurements of upward currents of thermal (energies, E, less than 0.4 eV), epithermal (0.4 eV < E < 0.7 MeV) and fast (0.7 < E < 2 MeV) neutrons. Absolute calibration of all three energy ranges was made using counting rates measured when the spacecraft was poleward of $+85^\circ$ N Latitude near L_S $\sim 10^\circ$, when the thickness of the CO₂ seasonal frost cover at the north pole was greatest [20,21].

The connection between measured counting rates and neutron energy distributions is made by combining our absolute calibration with simulations of neutron counting rates using the Monte Carlo Neutral Particle computer code, MCNPX, fitted with a special planetary boundary patch developed for Mars [21]. The relationship between the water-equivalent hydrogen content (W_{H_2O}) of soil having the composition measured at Mars Pathfinder [25] and the calibrated counting rates (Epi) can be fit quite well (correlation coefficient, R = 0.9996) by the power law function,

$$W_{H_2O} = 1.31 [Epi]^{-1.72}. \quad (1)$$

A CO₂ frost-free map of epithermal counting rates constructed from the first year of mapping data is shown in Figure 1. Correction of all counting rates for variations in cosmic rays, global variations in atmospheric thickness, and effects of variations in the NS high voltage were made by normalizing peak areas for each measured spectrum to the average counts summed over ± 0.5 day when the spacecraft was equatorward of $\pm 40^\circ$ latitude [21]. Corrections were also made for variations in atmospheric thickness due to topography [21].

An overview of Figure 1 shows that Mars can be separated into three domains that have very different character. A large spatial domain north of $+50^\circ$ latitude is marked by very low epithermal neutron counting rates. The minimum rate surrounds the north pole and a secondary minimum is centered at about -130° east longitude between 65° and 70° north latitude. The

spatial domain of low counting rates is pinched off, being narrowest at about -45° East Longitude in north Acidalia. South of -50° the map is dominated by low counting rates in a broad ellipse with its long axis pointing toward 110° east longitude. At mid-latitudes between $\pm 50^\circ$, a mixed pattern of both low and high counting rates exists, having minima within Arabia Terra and its antipode.

3. Maps of Lower-Bound Estimates of Hydrogen on Mars: The epithermal-neutron counting-rate map of Figure 1 was converted to lower-bound abundances of water-equivalent hydrogen using Equation 1. The result is shown in Figure 2. Two different reservoirs are evident. The component having large hydrogen abundances poleward of $\pm 50^\circ$ latitude corresponds to terrain poleward of the red-yellow wavy contour in the top panel of Figure 2. Although abundances in the south range between 20% and 50% by mass, those in

the north extend to 100%. Abundances of hydrogen equatorward of these contours (the second reservoir) range between 2% and 9% by mass with a most probable value of 4%.

Inspection of Figure 2 reveals several striking observations. First, the two largest discrete reservoirs at equatorial latitudes occur at antipodal longitudes. That in Arabia Terra is centered near the equator at 25° east longitude, and its antipode is just below the equator at about 185° east longitude. Both maximize between 8% and $8.5\% \pm 1.3\%$ water equivalent hydrogen, and are bisected by the zero km elevation contour. Relative maxima extending beyond these absolute maxima also follow the zero-km elevation contour. H_2O weight fractions for selected mid-latitude sites are collected in Table I. Other observations worth noting are that Alba Patera at $+40^\circ$ latitude and 115° west longitude is a relative maximum, the terrain just beyond

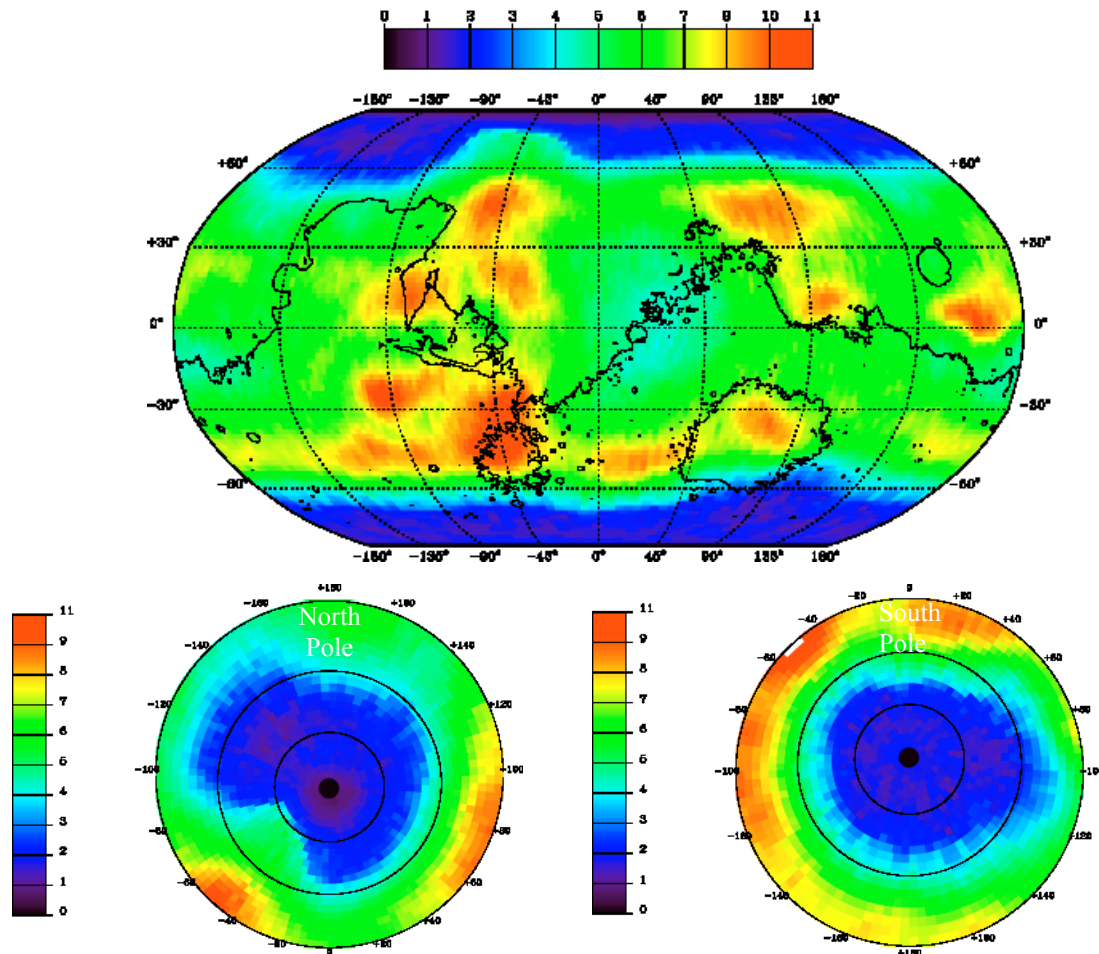


Figure 1. A CO_2 frost-free map of Mars. Data south of -50° latitude were measured during the late summer in the south, [$329^\circ < L_s < 1.7^\circ$], and data north of $+50^\circ$ latitude were measured after the northern summer solstice, [$100^\circ < L_s < 131^\circ$]. A contour of topography at 0 km is superimposed on the Robinson map.

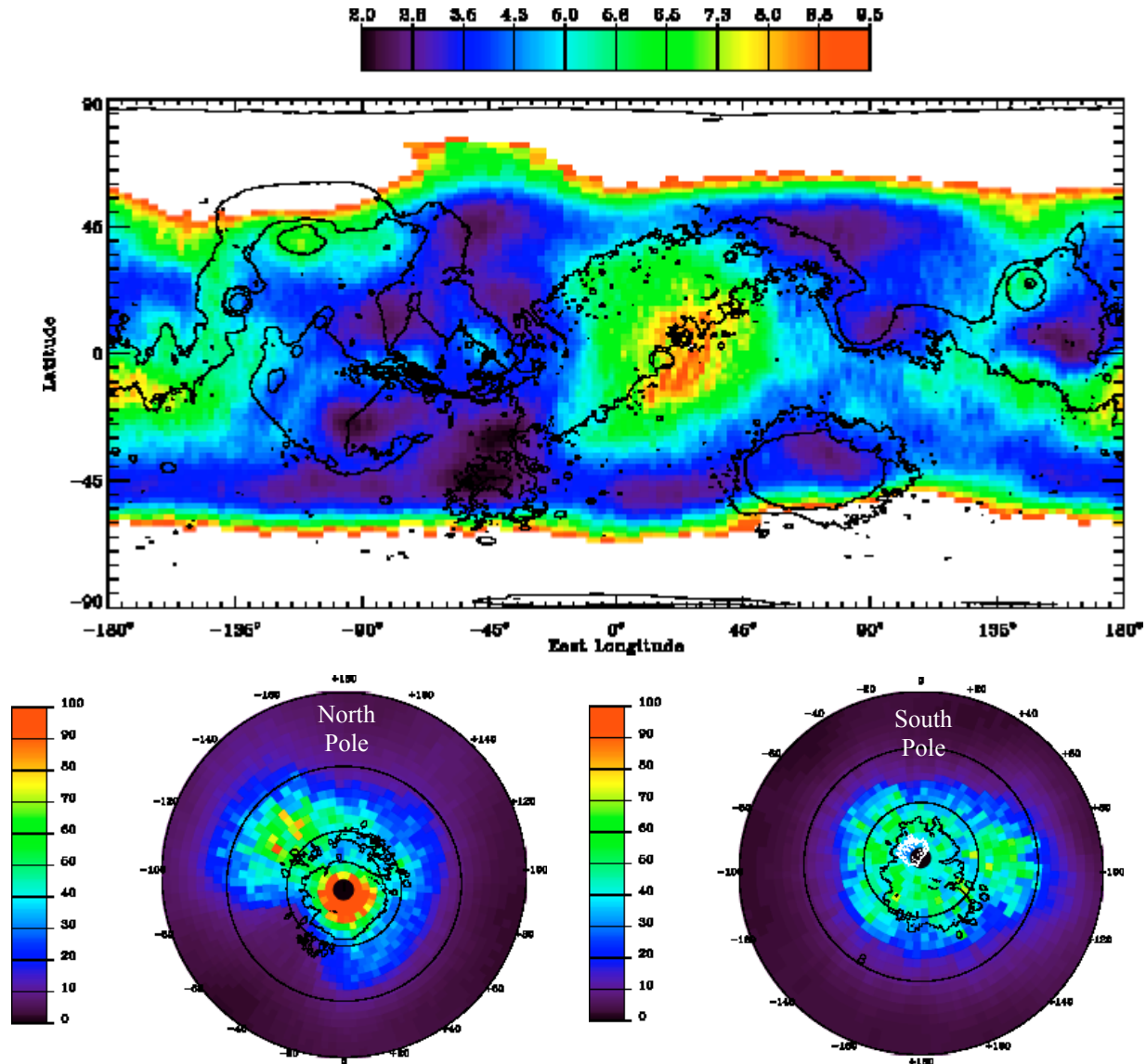


Figure 2. Maps of lower-bound estimates of the water abundance on Mars. The map at mid latitudes is given in cylindrical projection in the upper panel, that at latitudes poleward of $\pm 45^\circ$ are given in stereographic projection in the lower left and right hand panels, respectively. Contours of topography at the -2.5 km, 0 km, $+6$ km and $+10$ km are superimposed on the cylindrical map. Contours outlining the extent of the water-ice polar cap in the north are superimposed on the stereographic map at the lower left, and those outlining the residual cap (white line) and layered terrain (black line) in the south are shown in the lower right-hand panel.

the Kasei Valles and Valles Marineris outflow channels that debouch into Chryse Planatia have relatively low hydrogen abundance, and the relative minimum within Hellas Planatia is in its northeast sector where most global dust storms originate.

4. Summary and Conclusions: One year of Mars Odyssey NS epithermal-neutron data were used to construct a CO_2 frost-free map of Mars. These data provided input for a map of lower-bound water-equivalent

hydrogen concentrations within about one meter of the Martian surface. Two major near-surface reservoirs are readily delineated. One surrounds both poles extending down to about $\pm 50^\circ$ latitude and has relatively high-grade deposits. The near-polar mass concentrations of water-equivalent hydrogen range between 20% and 100%. A second mid-latitude reservoir maximizes at antipodal locations near the equator. Water-

equivalent mass concentrations in this reservoir range between 2% and 9%.

A minimum thickness of a global covering of water can be estimated from the lower-bound water-equivalent hydrogen maps in Figure 2. The results are tabulated in Table 2. If the thickness of these deposits is no more than the 1m nominal detection depth, then the total inventory of near-surface hydrogen amounts to about a 13-cm global layer of water. If, for example, the deposits extend to a depth of 1 km, then the inventory could amount to about a 130 m global layer. Although orbital neutron data only reflect hydrogen concentrations within about 1 m of the Martian surface, they provide no constraints on how deep the deposits may extend. If the foregoing 1 km depth estimate applies, these deposits contain an important part of the Martian inventory of juvenile water inferred from geomorphic studies [1,6,8,26].

References: [1] Carr, M.H. (1986) *Icarus* 68, 187-216. [2] Smith, D.E., et al. (1999) *Science*, 284, 1495-1503. [3] Jakosky, B.M., C.B. Farmer (1982) *J. Geophys. Res.*, 87, 2999-3019. [4] Jakosky, B.M., R.M. Haberle (1992), in *Mars*, Kieffer, H.H., B.M. Jakosky, C.W. Snyder, M.S. Matthews, eds., pp969-1016, U. of A. Press, Tucson. [5] Mellon, M.T., B.M. Jakosky

(1993) *J. Geophys. Res.*, 98, 3345-3364. [6] Baker, V.R. (2001) *Nature*, 412, 228-236. [7] Carr, M.H. (1996) *Water on Mars*, 229 pp, Oxford U. Press. [8] Jakosky, B.M., R.J. Phillips (2001) *Nature*, 412, 237-244. [9] Yung, Y.L. (1988) *Icarus*, 76, 146-159. [10] Luhman, J.G., et al. (1992) *Geophys. Res. Lett.*, 21, 2151-2154. [11] Carr, M.H. (1990) *Icarus*, 87, 210-227. [12] Jakosky, B.M. (1991) *Icarus* 94, 14-31. [13] Leshin, L.A. (2000) *Geophys. Res. Lett.*, 27, 2017-2020. [14] Boynton, W.V., et al. (2002) *Science*, 297, 81-85. [15] Feldman, W.C., et al. (2002) *Science*, 297, 75-78. [16] Mitrofanov, I., et al. (2002) *Science*, 297, 78-81. [17] Tokar, R.L., et al. (2002) *Geophys. Res. Lett.* 29, doi:10.1029/2002GL015691. [18] Biemann, K, et al. (1977) *J. Geophys. Res.*, 82, 4641-4658. [19] Anderson, D.M., A.R. Tice (1979) *J. Mol. Evol.*, 14, 33-38. [20] Feldman, W.C., et al. (2003) *J. Geophys. Res.*, Submitted. [21] Prettyman, T.H., et al., *J. Geophys. Res.*, Submitted. [22] Feldman, W.C., et al. (1993) *J. Geophys. Res.*, 98, 20855-20870. [23] Feldman, W.C., et al. (2002) *J. Geophys. Res.*, 107, DOI 10.1029/2001JA000295. [24] Boynton, W.V., et al. (2003) *Space Sci. Rev.*, Submitted. [25] Wänke, H., et al., (2001) *Space Sci. Rev.* 96 317-330. [26] Squyres, S.W. (1989) *Icarus*, 79, 229-288.

Table 1 Water-Equivalent Hydrogen for Selected Mid-Latitude Sites

Site	(Latitude, Longitude)	Weight Fraction
Alba Patera	(+37.5°, -112.5°)	6.7 ± 1.0 %
Arabia	(- 2.5°, +27.5°)	8.5 ± 1.3 %
Arabia Antipode	(-12.5°, -177.5°)	8.0 ± 1.2 %
Argyre	(-47.5°, -42.5°)	2.3 ± 0.4 %
Pathfinder	(+17.5°, -32.5°)	2.7 ± 0.4 %
Sinus Meridiani	(+ 2.5°, -2.5°)	6.5 ± 1.0 %
Solis Planum	(- 22.5°, -92.5°)	2.3 ± 0.4 %
Viking 1	(+ 22.5°, - 47.5°)	2.9 ± 0.4 %
Viking 2	(+47.5°, +132.5°)	5.7 ± 0.9 %

Table 2 Equivalent Global Thickness of Water Layer

Latitude Band	$\rho D \iint \mathbf{W}_{\text{H}_2\text{O}} d\Omega / 4\pi$	
	D = 1 m	D = 10 ³ m
$\Lambda > +45^\circ$	3.8 cm	38 m
$\Lambda < -45^\circ$	4.4 cm	44 m
$-45^\circ < \Lambda < +45^\circ$	5.3 cm	53 m
Total	13.4 cm	134 m

TEMPORAL INVARIANCE OF WIND ORIENTATIONS AS RECORDED BY AEOLIAN FEATURES IN PROCTOR CRATER. L. K. Fenton¹, M. I. Richardson², and A. D. Toigo³, ¹Arizona State University, Department of Geological Sciences, Mail Code 1404, Tempe, AZ 85287, lkfenton@asu.edu, ²California Institute of Technology, Department of Geological and Planetary Sciences, MS 150-21, Pasadena, CA 91125, mir@gps.caltech.edu, ³Cornell University, Center for Radiophysics and Space Research, 326 Space Sciences Bldg., Ithaca, NY 14853, toigo@astro.cornell.edu.

Introduction: The importance of wind action among contemporary surface processes on Mars has become well known since the first dunes were observed in spacecraft images. Wind circulation patterns determine the location and magnitude of sources, sinks, and transport pathways of particulate materials. The winds also dictate the morphology of aeolian features, such as yardangs and dunes. Because of this coupling between surface materials and the atmosphere, the study of one is not complete without the study of the other.

With the advent of mesoscale atmospheric models, the circulation of a small region can be examined in detail for the first time. These models can be used in concert with spacecraft data, and in particular MOC NA (Mars Orbiter Camera Narrow Angle) images, which provide detailed wind orientations at the scale of tens of meters. Comparing the two provides not only a verification of the mesoscale model and the GCM to which it is coupled, but also an understanding of the source of the winds that influence the surface. This in turn can lead to a better understanding of landscape morphology and the sources and sinks of mobile material.

In this work, we apply the Mars Mesoscale Model 5 (Mars MM5) to Proctor Crater to determine how the observed aeolian features correlate with predicted wind orientations. The various aeolian features on the crater floor have different relative ages, such that the comparison of each type of feature with the current wind regime provides an understanding of how wind circulation patterns have changed since the oldest remaining aeolian features formed.

Study Area: Proctor Crater is a 150 km diameter crater located in Noachis Terra, in the southern highlands of Mars and roughly 900 km west of Hellas Planitia (see Fig. 1). It contains numerous aeolian features, including a 35 X 65 km wide dark dunefield that is prominent in Figure 1. Generally visible only in MOC NA images, small bright dune-like features that are interpreted as transverse bedforms cover most of the Proctor Crater floor. In addition, dark filamentary streaks that are interpreted to be dust devil tracks form each summer. Each type of feature is aligned with its formative winds, giving an indication of the prevailing wind orientation at the time it was last active.

The Mars Mesoscale Model 5: To model the winds over Proctor Crater, we applied the Mars MM5 (Mesoscale Model Version 5), developed from

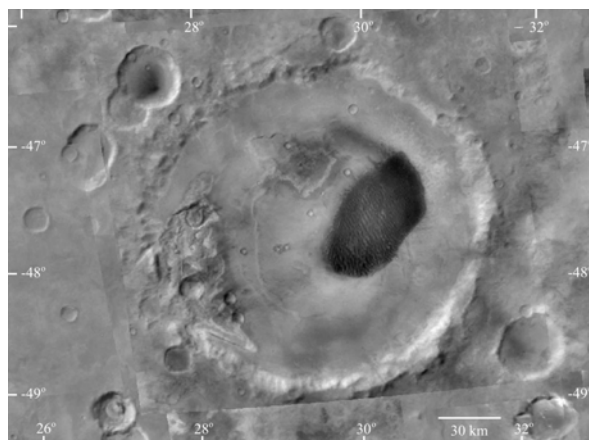


Figure 1. MOC Wide Angle mosaic of Proctor Crater

the PSU/NCAR MM5 [1]. The Mars MM5 uses boundary and initial conditions provided by the GFDL Mars GCM [2]. It is nonhydrostatic, uses terrain-following sigma-coordinates, and applies the same radiation scheme as the GFDL Mars GCM. Recent topography, albedo, and thermal inertia maps are used to model the surface. The model uses a boundary layer scheme from the Medium Range Forecast (MRF) to represent the transfer of momentum from the atmosphere to the surface.

We ran the model for seven ten-day time periods distributed through the Martian year. We used 24 vertical levels from the surface to ~50 km and a horizontal spatial resolution of 10 km. The model timestep was 5 seconds, although data output was recorded 12 times each day (every 2 hours).

Aeolian Features in Proctor Crater:

Dark Dunes. Inspection of MOC NA images shows that the interior of the dark dune field in Proctor Crater is dominated by large (1-2 km wide) reversing transverse and star dunes [3]. Near the edge of the dune-field, the sand layer thins and the large dune ridges become barchanoid dunes with slipfaces that are easy to interpret, as they are always oriented downwind (see Figure 2).

Measurements were made of the orientations of these slipfaces. A rose diagram of the results is shown in Figure 3a. The dune slipfaces show three dominating wind orientations. The primary orientation, which is present throughout the dune field, indicates winds

from $239^\circ \pm 18^\circ$ (mean \pm standard deviation), or WSW. The secondary orientation indicates winds from $110^\circ \pm 18^\circ$, or ESE, and these slipfaces are present in all but the easternmost portion of the dune field. The final, tertiary orientation indicates winds from $75^\circ \pm 9^\circ$, or ENE, and these slipfaces are only present on the eastern edge of the dunefield. These three slipfaces orientations implies that the dark dune field is located in a convergent wind regime [3], which is typical of terrestrial dune fields containing reversing transverse and star dunes [4].

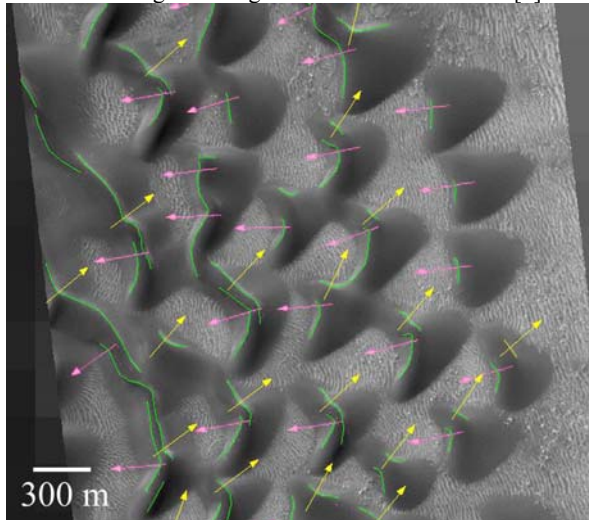


Figure 2. Dunes at the eastern edge of the dune field. Arrows indicate differing slipface orientations. Green lines indicate dune brinks.

Bright Duneforms. Small bright bedforms are distributed nearly uniformly across the floor of Proctor Crater. Where they come into contact with the large, dark dunes, they lie stratigraphically beneath them. Figure 4 shows the passage of large, dark barchans across a field of small bright bedforms. In the wake (upwind) of the dark dunes, the bright bedforms have been destroyed, implying that the migration of dark dunes also erodes away the previously existing bright bedforms.

Figure 3b shows the measured along-crest orientations of several hundred bright bedforms. The bedforms appear symmetrical at the scale of MOC NA images, with no obvious upwind or downwind slopes, and thus there is a directional ambiguity of 180° . All directions are therefore constrained to greater than 270° or less than 90° . There are two modal directions that appear in the wind rose: a primary one at $330\text{--}350^\circ$ and a secondary one at 5° . If these bright duneforms are oriented transverse to the winds that most recently shaped them, as would be the case if they are granule ripples or small transverse dunes, then they reflect winds oriented ENE-WSW and ESE-WNW, respectively.

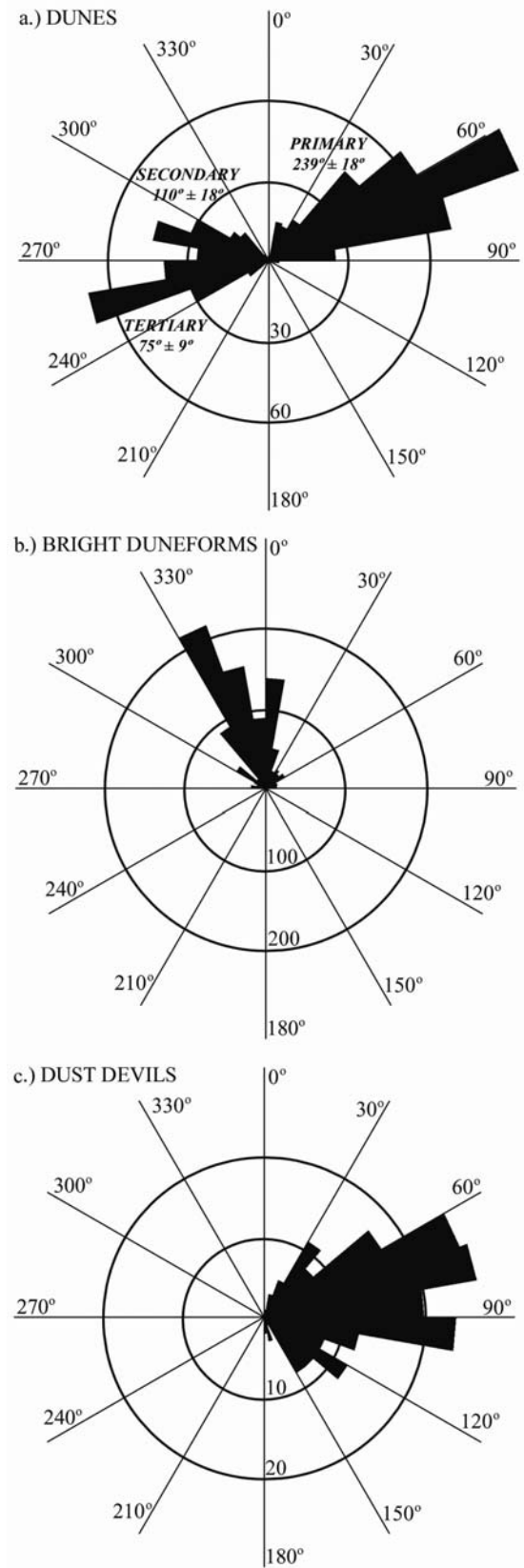


Figure 3. Wind roses showing the orientations of aeolian features.

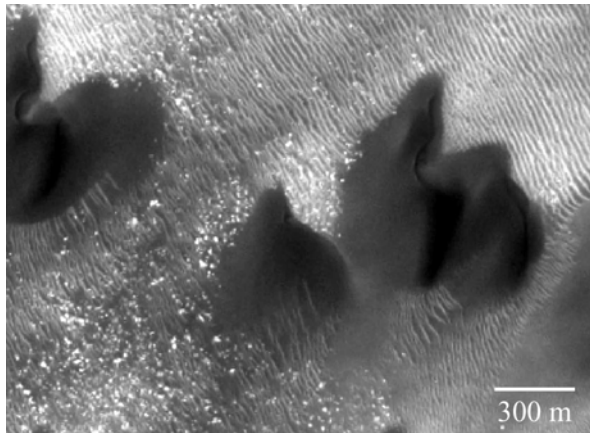


Figure 4. Migrating dunes erode smaller, bright bedforms

Dark Filamentary Streaks. Dark filamentary streaks form each summer and are erased each winter in MOC NA images of Proctor Crater. Figure 5 shows such streaks emanating from a dark patch, probably of sand. These tracks were probably created by dust devils that formed on the dark patch and moved downwind to the ENE.

Figure 3c shows the orientations of nearly two hundred such dark streaks. Because determining the upwind versus downwind direction is impossible from observing most dust devil tracks, all directions shown have been restricted to 0° to 180° . Tracks oriented at 0° or 180° are oriented north-south, and tracks measured at 90° are oriented east-west. One modal direction is evident in Fig. 5, with a spread from 60° - 100° , or generally ENE-WSW. Because of the tracks shown in Figure 5, we consider the predominant upwind direction to be from the WSW.

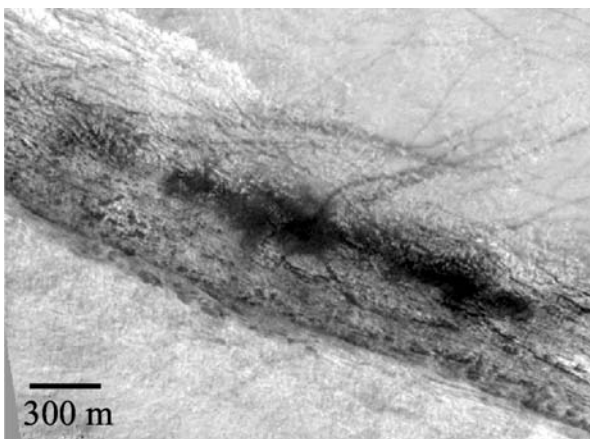


Figure 5. Dust devil tracks emerge from a small patch of dark material

Model Results: The strongest daily winds shift in direction with the seasons (see Figure 6). Fall and winter winds come from the west and west-southwest. Spring and summer winds blow from the east-northeast, but they are weaker than their fall and winter counterparts. The fall and winter winds correspond well with the primary dune slipfaces, and they are most likely responsible for both the dune slipfaces and the orientations of most of the bright duneforms that are common on the Proctor Crater floor.

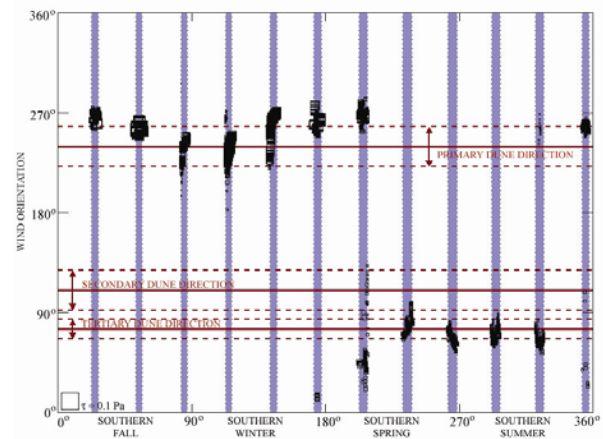


Figure 6. The highest-stress winds predicted by the mesoscale model over the Proctor Crater dunefield throughout the year.

Dust devil tracks are also aligned with the primary wind, but they are generally only visible in spring and summertime images, indicating that this fall and winter wind is not responsible for creating the majority of dust devil tracks. Rather, they are produced by weaker winds from the WSW that blow only during the spring and summer (not shown in Fig. 6)

The secondary winds, from the ESE, are absent from Fig. 6. It is not clear why the ESE winds do not appear as the strongest winds at some point of the year, but it may be that the model is not capturing small-scale processes that create these winds.

Conclusions: Two of the three dune slipfaces are produced by the mesoscale model, indicating that the winds that last influenced the dunes are still active today. The bright duneforms, if transverse bedforms, are consistent with either the primary or the tertiary winds that influence the dark dunes, suggesting that the winds that produced the bright bedforms are also still active today. Finally, the dust devil tracks are oriented to summertime afternoon winds predicted by the model (although not shown in this abstract), and clearly indicate present-day winds.

All three types of aeolian features, regardless of their age, are consistent with present-day winds predicted by the mesoscale model. No shift in prevailing

wind orientation is apparent in the aeolian features in the floor of Proctor Crater.

[1] Toigo, A. D. (2001) Ph.D. Thesis, Calif. Inst. Of Tech, 139 pp. [2] Wilson R. J. and Hamilton, K. (1996) *JAS*, 53, 1290-1326. [3] Fenton, L. K., Bandfield, J., and Ward, A. W. (2003) *JGR* (in press). [4] Wasson, R. J. and Hyde, R. (1983) *Nature*, 304.

CHARACTERISTICS AND DISTRIBUTION OF THE MARS NORTH POLAR BASAL UNIT Kathryn E. Fishbaugh¹ and James W. Head III¹, ¹Brown University, Dept. Geol. Sci., Box 1846, Providence, RI 02912, kathryn_fishbaugh@brown.edu, james_head_III@brown.edu

Introduction: Beneath much of the northern polar layered deposits lies a dark, platy unit (Fig. 1) noted by a few authors [1,2] and described in detail by *Byrne and Murray* [3] and *Edgett et al.* [4]. We have continued the investigation of this unit [5-7] by examining MOC images and MOLA data (looking forward to the release of spring/summer THEMIS data) of the polar cap and of the features interpreted by *Fishbaugh and Head* [8-10] as polar material remnants and glacial retreat features. Here we discuss the broad characteristics, two example outcrops, and the distribution of the BU. In another abstract in this volume, we examine possible origins and modifications of the BU.

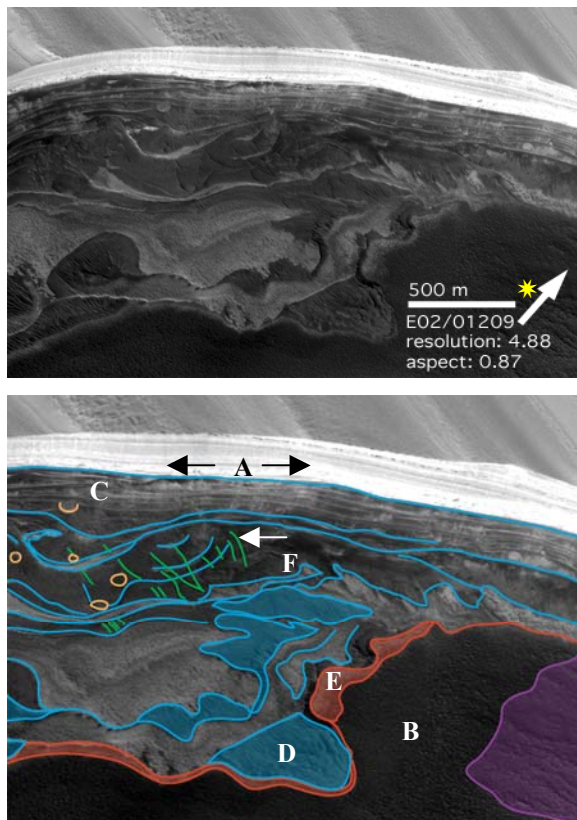


Figure 1. (a) MOC image E02/01209 showing outcrop of PLD and eroding layers of BU. (b) Sketch map of MOC image. Purple region shows ridges within dark mantle. Red outlines bright halo at base of BU, blue outlines major layers, with the shaded areas showing evidence of eolian erosion. Green outlines small, erosional ridges, and orange outlines pits whose impact origin is uncertain. Letters are explained in the text. Location of image is marked in Fig. 4.

Broad Characteristics: The main features of this unit have been described by *Byrne and Murray* [3] and *Edgett et al.* [4]. There is a stark contrast in albedo between the PLD and the BU (Fig. 1). Sometimes, the BU/PLD contact is associated with a break in slope and

in some places is manifested as a protruding step. The BU also has a platy appearance. Further investigation of the unit for this study using MOC images and MOLA profiles reveals that the unit is internally layered in many places. Layering in the BU is more irregular than but can be as fine scale as the PLD. Nearly all basal layers pinch-out within the width of one MOC image.

The contrast in properties between the PLD and the BU has resulted in differential erosion. Erosion of the BU is typically characterized by pitting, residual mesas, ridges, and anomalous grooves. Yardangs are visible in a few images of eroding layers. Individual layers within the BU also erode at different rates. Evidence of mass wasting is apparent but not common. Small pits (diameter = <300 m) can be found in a few MOC images of the BU where erosion has exposed the surface of some layers; an impact origin for these features is uncertain. Since so little of the unit has been exposed, it is unknown how many impact craters may yet be buried.

The BU/PLD contact warrants further detailed discussion. In places (e.g., *A* in Fig. 1), the contact appears distinct and sharp. However, closer examination reveals more complexity. While *Edgett et al.* [4] note that the “waviness” of the contact in some locations (e.g., *A* in Fig. 2) is a post-formation erosional effect, there are few if no locations where a single BU layer can be traced along the entire contact, thus erosion must have occurred between formation of the basal unit and formation of the PLD. Direct evidence of some erosion during this time is apparent in MOC image E02/01056 wherein pitting within the upper layers of the basal unit is exposed and has resulted in undulations in the lower layers of the overlying PLD.

Erosion of the BU and abrupt subsequent deposition of the PLD may not necessarily characterize the entire BU/PLD contact. Instead, the transition may have been more gradual. In several images there exist dark layers within the lower PLD (*Edgett et al.* [4] noted dark lenses in one MOC image). These layers (*A* in Fig. 3) are as dark as the dunes in the north polar erg (*B* in Fig. 3). Either the dark material of the BU was gradually being deposited in smaller quantities along with the newly forming PLD until it finally ceased to be deposited, or, as discussed below, erosion of the BU freed material which was transported by wind and included into the lower PLD.

Dunes are closely associated with the BU, leading some [3,4] to conclude that it is an icy, sand-rich deposit and is the source for the large circumpolar ergs [11]. According to our observations, dunes are visible in many but not all MOC images of the unit. *Thomas and Weitz* [12] have proposed that the north polar erg source

was the PLD. With these new observations of the BU, it seems likely that the BU is actually providing a large portion of the sand-sized particles. Where no dunes are present, there sometimes exists a dark mantle of material which has presumably eroded from the BU (e.g., *B* in Fig. 1 & *E* in Fig. 2). However, dunes may also be eroding from PLD layers just above the BU/PLD contact. Figure 3 shows dark lenses of material (*A*) within the PLD which have albedos similar to that of the dunes (*B*). Dark lenses are not visible in every image which contains both the BU and dunes, and not all images with dark lenses have dunes (although the dunes may have migrated away); thus, the dark lenses cannot be the sole source of dune material. Instead, we suggest that material may have eroded from the BU and migrated as dunes onto the young, still-forming PLD, leaving dark material within the lower layers of the PLD; this may currently be happening in Chasma Boreale (e.g., MOC image E03/01735) and is also hypothesized to have occurred in Antarctica [13].

Example Outcrops: Olympia Planitia. We have created detailed sketch maps of BU outcrops in MOC images. As illustrated by Fig. 1, the layering within the unit is complex, with no single layer extending across the entire image (a distance of about 3.3 km). The outcrop exhibits 3 main sequences. At the bottom of the image, lying stratigraphically at the base, is a rough textured, dark mantle (*B*). This texture could be a result of the presence of hummocks, boulders, or small dunes. Above this lie alternating bands of bright and dark material, and above this are the brighter PLD.

Within the alternating light and dark bands of the BU is a section (*C*) just below the PLD with steeper slopes (about 40°) than the more exposed basal layers below it. There are about eight dark layers in this 300 m thick section; therefore, each dark layer is about 35 - 40 m thick. As explained below, the lighter layers are much thinner than the darker. Within this section, no particular layers extend across the entire image. The PLD unconformably overlies the BU as illustrated by the fact that the top BU layers do not extend uniformly across the image but are instead eroded in some places.

The lowest BU layer is characterized by a relatively low albedo and by lineations likely of eolian origin which may either be yardangs or longitudinal dunes (*D*). Darker layers stratigraphically above and the dark mantle below this show no such evidence of eolian reworking. It is thus assumed that the eolian features are not currently forming but have been exhumed by erosion of overlying layers. While ridges of unknown origin (*F*) appear in a few of the upper dark layers, they are for the most part featureless.

Between the dark mantle (*B*) and the lowest BU layer, there exists a narrow, bright halo of material (*E*). Either this represents 1) a very thin layer or 2) material

which has mass wasted from above and collected here. Since the texture of the darker layers shows through in the lighter layers, it can be assumed that the darker layers are thicker. This same relationship is apparent throughout the BU in this outcrop. The bright halo may consist of material eroded from the brighter layers. Note its diffuse, irregular nature. Bright streaks cross-cut many of the layers just below the PLD, and there is little to no evidence of mass wasting of the darker material. Therefore, the brighter material is interpreted to be thinner and more mobile than the darker.

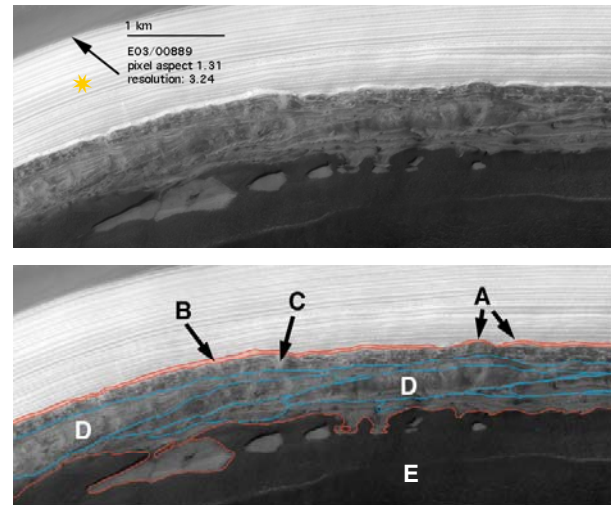


Figure 2. MOC image E03/00889 showing outcrop of PLD and the darker BU below them with dark mantle at the base. Sketch map outlines boundaries of exposed BU in red and major layers in blue. The red shaded area shows the transition zone between the BU and PLD at the contact. What look to be large lenses of material or massive beds in the BU (*D*) are actually just thinner layers exposed on a shallow slope. Letters are explained in the text. Location of image is marked in Fig. 4.

Chasma Boreale. The best exposures of the basal unit in Chasma Boreale (e.g. Fig. 2) lie within the two arcuate scarps at the chasma head region (Fig. 4). Alternating light and dark layers are evident in this region, as in Olympia Planitia. There exists a transitional zone in the PLD just above the contact (*B* in Fig. 2) which may consist of talus [4]; indeed light streaks of material emanate from this transitional zone (*C*). To allow talus to accumulate, there must be a small break in slope at the contact, too small to be discernable in MOLA profile data. Assuming that the talus was eroded from the PLD, the question then becomes, “Of what is this talus composed?” If it is dust, then why is it much lighter even than the darker PLD layers (which presumably contain dust [14]) in full sunlight on the left of the image? Instead, this transitional zone may be the uppermost layer of the BU with light streaks emanating from it as observed in the lighter layers of the BU in Olympia Planitia (Fig. 1).

Near the center of the BU in this outcrop are what appear to be massive beds or large lenses of material

(D), leading *Edgett et al.* [15] to conclude that the BU may consist of several different units. However, MOLA data reveal this to be a slope effect. The lenses are just layers exposed at shallower slopes than the other layers, again indicating differential erosion within the BU.

While no dunes appear in this image, the dark mantle at the base of the BU slope (E) may have eroded from the BU and not yet been worked into dunes.

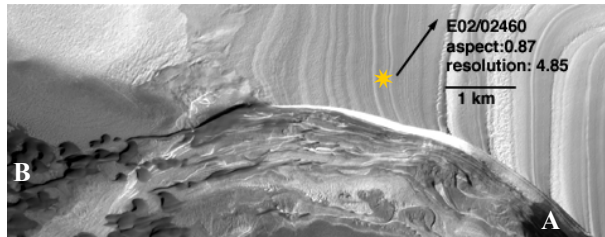


Figure 3. MOC image E02/02460 showing thin outcrop of lower PLD layers with the darker BU below. This image partially overlaps that of Fig. 1. Notice dark layers in PLD in lower right corner (A) and the dark dunes in the lower left corner (B) which may eroded from these dark layers. Location of image is marked in Fig. 4.

Distribution: The BU crops out in troughs near and extending into Olympia Planitia (elevation of BU/PLD contact at about -4330 ± 110 m) and within the walls of Chasma Boreale (elevation at about -4520 ± 80 m) [3,4] (Fig. 4). *Byrne and Murray* [3] suggest that Olympia Planitia is an exposure of the BU on the 180°W side. While few MOC images of the cap in the longitude range $270\text{--}70^\circ\text{W}$ were available at the time of their study, further analysis of newer MOC images shows that the BU does not appear in the troughs within this region. Thus, the layer pinches-out beneath the cap somewhere between Chasma Boreale and the cap margin or has been eroded back to this location (Fig. 4b). Another possibility is that the BU exists only at the edges of the polar deposits in the locations observed and not beneath the center.

We have continued the investigation into the occurrence of this unit by examining the currently available MOC images of the features interpreted as polar material remnants and glacial retreat features [8–10]. While there are associated patches of dunes, there is no obvious exposure of the BU within these features. The possible polar remnant near 230°W is another story. Some images (e.g., MOC image M18/00121) show evidence of dark, eroding material which is possibly the BU. Without images of the contact with PLD, this cannot be uniquely determined.

Examination of images of the polar remnant near the small chasmata to the west of Chasma Boreale and of the mesa near the mouth of Chasma Boreale leads again to inconclusive determination of the existence of the BU. Dune fields lie near these features, but there is no immediately apparent PLD/BU contact, and the mesa and remnant scarps are frost-covered in most images.

Kolb and Tanaka [1] have suggested that the lobe extending from the mouth of Chasma Boreale is a remnant of this BU, and *Edgett et al.* [4] claim that the chasma floor consist of the BU. Unfortunately, there are no images of the lobe scarp which would allow a cross-sectional view. Our preliminary interpretation of these lobate deposits is that they represent a combination of lower BU layers exhumed by outflow [16] and by katabatic winds [17] and deposition of material from the outflow.

If one cannot assume that the presence of dunes necessarily indicates the presence of the BU, it must be concluded that the BU does not exist anywhere except beneath the main polar cap (and in the form of Olympia Planitia). Otherwise, if it did exist elsewhere, it has since been significantly eroded and is the source for isolated patches of dunes.

Summary: The basal unit has had a complex depositional history. Our analyses have outlined the following characteristics of the basal unit internal layers which must be explained by any theory of origin: 1) various manifestations of differential erosion, 2) differing amounts of eolian reworking, 3) pinching-out, 4) alternating relatively high/low albedos, and 5) almost no evidence of deformation. The BU/PLD contact is also complex, exhibiting unconformities and possibly being a source of the north polar dunes. Although its lower contact is not readily identifiable, this unit may represent the transition between deposition of the Vastitas Borealis Formation and the polar cap deposits and therefore provides important clues to the history of the north polar region (see *Fishbaugh and Head*, abstract in this volume).

Acknowledgements: Much thanks is extended to Lynn Carlson (Brown U.), Trent Hare (USGS), and Shane Byrne (Cal. Tech.) for their invaluable help in the GIS mapping portion of this project.

References: [1] Kolb, E. and K. Tanaka, *Icarus*, 154, 22-39, 2001. [2] Malin, M. and K. Edgett, *J. Geophys. Res.*, 106 (E10), 23,429-23,570, 2001. [3] Byrne, S. and B. Murray, *J. Geophys. Res.*, 107 (E6), 10.1029/2001JE001615, 2002. [4] Edgett, K. et al., *Geomorphology*, in press, 2003. [5] Fishbaugh, K. and J. Head, *Brown U.-Vernadsky Microsymposium* [CD-ROM], 36, abstract MS019, 2002. [6] Fishbaugh, K. and J. Head, *Brown U.-Vernadsky Microsymposium* [CD-ROM], 36, abstract MS020, 2002. [7] Fishbaugh, K. and J. Head, *Lunar Planet. Sci.* [CD-ROM], XXXIV, abstract 1250, 2003 [8] Fishbaugh, K. and J. Head, *J. Geophys. Res.*, 105, 22,455-22,486, 2000. [9] Fishbaugh and Head, *Icarus*, 154, 145-161, 2001. [10] Fishbaugh, K. et al., *Lunar Planet. Sci.* [CD-ROM], XXXII, abstract 1426, 2001. [11] Greeley, R., et al., in *Mars*, edited by H. Kieffer et al., pp. 730-766, Univ. of Ariz. Press, Tucson, 1992. [12] Thomas, P. and C. Weitz, *Icarus*, 81, 185-215, 1989. [13] Koerner, R., *Science*, 244, 964-968, 1989. [14] Thomas, P. et al., in *Mars*,

MARS NORTH POLAR BASAL UNIT: K. E. Fishbaugh and J. W. Head

edited by H. Kieffer et al., pp. 767-795, Univ. of Ariz. Press, Tucson, 1992. [15] Edgett, K. and M. Malin, *Lunar Planet. Sci.* [CD-ROM], XXXII, abstract 1124, 2003. [16] Fishbaugh,

K. and J. Head, *J. Geophys. Res.*, 107 (E3), 2-1-2-29, 2002b. [17] Howard, A., *Icarus*, 144, 267-288, 2000.

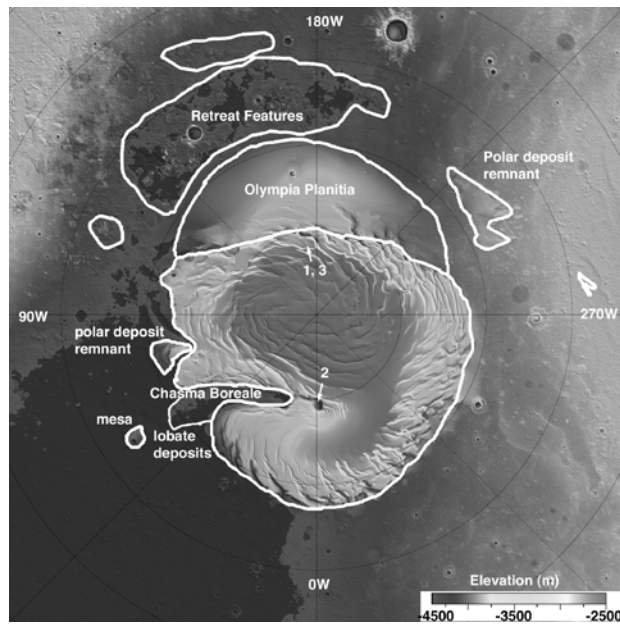


Figure 4a. MOLA shaded relief map of north polar region outlining major features discussed in text. Numbers indicate position of MOC images shown in Figs. 1, 2, & 3.

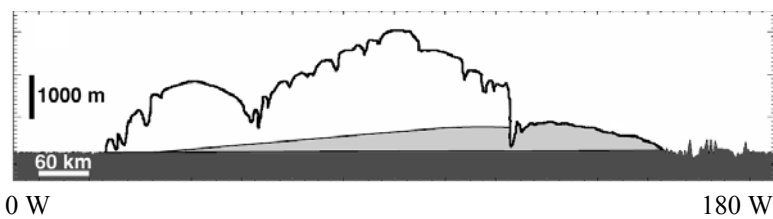


Figure 4b. Approximate profile of the basal unit (shaded grey) beneath the current polar layered deposits. From *Byrne and Murray* [3] (Fig. 11).

MARS NORTH POLAR STRATIGRAPHY AND IMPLICATIONS FOR GEOLOGIC HISTORY Kathryn E. Fishbaugh¹ and James W. Head III¹, ¹Brown University, Dept. Geol. Sci., Box 1846, Providence, RI 02912, kathryn_fishbaugh@brown.edu, james_head_III@brown.edu

Introduction: We have continued investigation of the dark, layered, and possibly sand-rich unit beneath the north polar deposits begun by previous authors [1-4] and have described the detailed characteristics of this basal unit (BU) [5-7; *Fishbaugh and Head*, abstract in this volume]. While *Kolb and Tanaka* [2] describe the BU as consisting of early north polar deposits, *Byrne and Murray* [3] suggest that such a significant change in deposition style has taken place that the unit must represent a period in time when there was no polar cap. They believe that the BU consists of ice-rich paleoerg deposits that migrated to the low elevation plains underlying the current polar deposits. In addition to these possibilities, we suggest that the unit may have initially been deposited by outflow channels and/or a paleo-ocean.

Fishbaugh and Head [8-10] have shown that the north polar deposits may once have been larger, extending to about 75°N. Still unknown are the timing and cause of this retreat as well as how many times advance and retreat have occurred. The basal unit has yet to be placed conclusively in this history. Since the BU lies stratigraphically between the 3 By old Vastitas Borealis Formation and the polar cap deposits with a surface age of at most 100 Ky [11], it may represent a preserved record of at least part of the pre-cap north polar history.

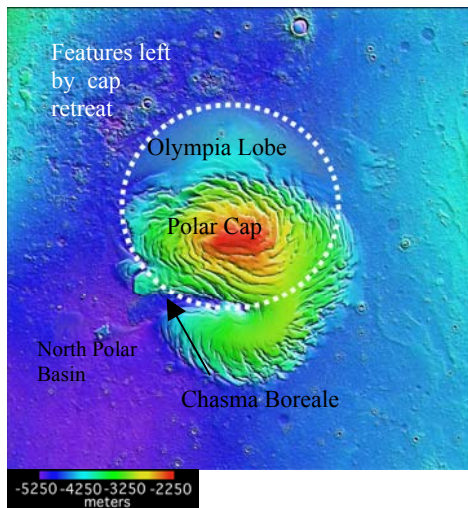


Figure 1. North polar region MOLA topography (72-90°N). Dotted line shows approximate extent of basal unit, though the floor of Chasma Boreale and the mesa beyond the mouth may also be part of the BU.

Here we examine three possible origins for this unit (paleopolar deposits, outflow channel/oceanic deposits, and eolian deposit) and three possible ways in which it may have been modified since its formation (paleoerg,

incorporation into basal ice, and basal melting with subsequent redistribution). Figure 1 shows the geographic context and topographic relationships of the BU, north polar cap, and the surrounding plains.

Possible Origins: We present three possible modes of formation of the BU and three possible ways in which it may have been modified since its formation.

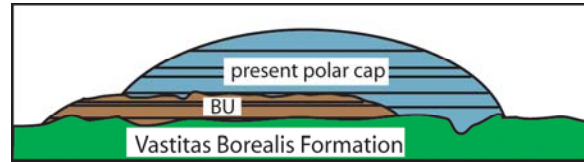


Figure 2. Sketch of present stratigraphy at north pole with the BU as a paleopolar deposit.

1) *Paleopolar Deposit* (Fig. 2): While not expounded upon in detail, according to *Kolb and Tanaka* [2], the BU represents a "an earlier phase of north polar deposits" (pg. 30). We interpret this to mean that the unit consists of paleopolar deposits, an earlier phase of polar cap deposition. We find that three major observations lend support to this idea: 1) the fine-scale layering of the BU, 2) the exclusive association of the BU with current polar deposits (and possibly with remnants of former extents of polar deposits), and 3) the "pile" shape of the unit.

In this case, the BU represents an unconformity in polar cap deposition and unknown amount of erosion during which time the environmental conditions changed such that one of two things happened. 1) The amount of atmospheric dust (or sand) decreased (possibly suddenly) and polar deposition continued with a lower sediment/ice ratio. 2) Large-scale erosion of earlier polar cap deposits resulted in a gradually increasing sediment/ice ratio as the ice sublimated leaving sediment behind.

If the BU does represent a shift in depositional style of polar deposits or large-scale erosion of former polar deposits, it may necessitate a relatively old age for the BU, possibly Early Amazonian. There are two reasons for this. 1) If the BU represents an early phase of polar cap deposition with more sediment than the current phase, then the necessary climate shift to allow more atmospheric suspension of sediment would be of a much larger magnitude than the smaller scale shifts which produce layering in the current PLD. 2) The BU has been more thoroughly eroded than the PLD, yet it is inherently more difficult to sublimate heavily sediment-laden ice than it is to sublimate purer ice. The resultant sublimation lag considerably slows the sublimation,

which could allow a possibly large volume of polar deposits to be "trapped" beneath the Olympia erg.

2) *Outflow channel/Oceanic deposits (Fig. 3):* Sediment brought by outflow channels [12] and a possible former standing body of water [13] may easily provide sand and ice-rich material for the BU.

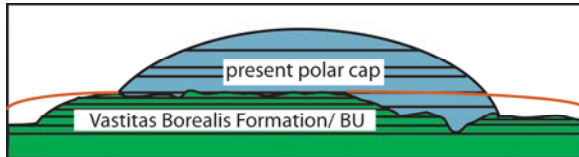


Figure 3. Sketch of present stratigraphy at north pole with the BU as a outflow channel/oceanic deposits, part of the Vastitas Borealis Formation. The red lines indicate possible previous extents of the deposits which have since been eroded away.

One major problem with this scenario is that the Vastitas Borealis Formation (VBF) is thought to consist in part of oceanic and outflow deposits [14,15]. Since the BU overlies the VBF, how could it be composed of these same deposits? In addition, there is apparently no evidence for the existence of this unit outside of the current polar cap bounds and Olympia Planitia. The answers may lie in the armoring of outflow channel/oceanic deposits near the pole.

Water from the outflow channels could have formed numerous standing bodies of water which froze. These ice and sand-rich deposits could then have sublimated, with the water being redeposited at the pole to form part of the north polar cap [16]. This cap would preserve the sediments beneath it. Still, the surrounding plains would have had to lose a lot of mass to sublimation since the upper BU contact is about 500 m higher than the plains. Alternatively, calculations of possible circulations patterns within an oceanic standing body of water in the northern plains yield deposition of material near the pole, rather than spread out within the lowest parts of the North Polar Basin [17]. Therefore, most of the sediments could have piled up near the pole, leaving the rest spread throughout the basin. As the polar cap formed, by several possible means, it would armor the sediment near the pole, preserving it beneath the polar deposits.

3) *Eolian Deposit (Fig. 4):* Another possible origin for the basal unit is eolian transport of material toward the north pole. *Anderson et al.* [18] have modeled the distribution of sand resulting from saltation, taking into account *Pollack et al.*'s [19] Mars general circulation model. They find that sand from northern mid latitudes would migrate to the north pole, creating the north polar erg within 50 Ky. Assuming a sufficient sand supply, this could indeed explain an accumulation of sand at the pole, but may not explain the detailed layered structure unless the process occurred with some cyclicity.

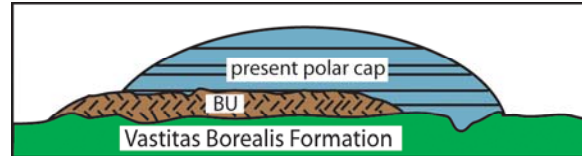


Figure 4. Sketch of present stratigraphy at north pole with the BU as an eolian deposit with possible cross-bedding.

Modification Processes: 1) *Paleoerg.* *Byrne and Murray* [3] suggest that the BU is an ice-rich paleoerg consisting of sand brought by means similar to those suggested by *Anderson et al.* [18]. We have found no evidence for the cross-bedding one may expect if the sand deposit was reworked into a major dune sea before deposition of the PLD. However, it may be that the resolution of the MOC images is not sufficient to detect the cross-bedding. If the deposit was reworked into a paleoerg, it would imply that some time passed between the end of sand deposition and the beginning of PLD deposition.

2) *Basal Ice (Fig. 5).* Regardless of the origin of the material within the basal unit, it may currently behave as basal ice as seen in terrestrial ice sheets [20-25]. On Earth, some glaciers and ice sheets have one or more layers of basal ice which can range in thickness from a few millimeters to tens of meters. Basal ice can have up to greater than 50% sediment by volume and has structural, chemical, and isotopic characteristics distinct from the overlying purer ice layers [20]. The contact between the basal ice and overlying ice is often quite distinct.

Basal ice can form by one or more of the following means [20,21]: 1) Regelation or congelation (glacial meltwater or other water with admixed sediment freezes on the lee side of obstacles or beneath the glacier) 2) net adfreeze (freezing front advances downward through saturated sediments, adding them to the glacier base), 3) entrainment of pre-existing ice (as ice sheet advances over buried glacier ice or debris aprons), or 4) mixing and crevassing (adds small amounts). The various means of creating basal ice require some amount of meltwater. Meltwater could have come from the formation of Chasma Boreale [26]. The creation of the basal unit as basal ice also would probably require longer time scales than the creation of terrestrial basal ice which at its thickest is an order of magnitude thinner than the martian basal unit. If the BU does comprise basal ice frozen to the bed of the PLD, it must be taken into account in any rheological models of the north polar cap.

3) *Basal melting and redistribution.* The BU may have affected the possible outflow which initiated the formation of Chasma Boreale (CB) [26] by influencing where CB formed (since the BU pinches out near CB) and/or by providing the water for the outflow as suggested by *Byrne and Murray* [3]. In addition, the

outflow may have taken place in some part along the PLD/BU contact and may have redistributed some of the BU. Indeed, since the BU outcrops on both sides of the CB head scarps, at least as much as is missing from those depressions must have been redistributed, possibly providing the sediment for the CB dunes.

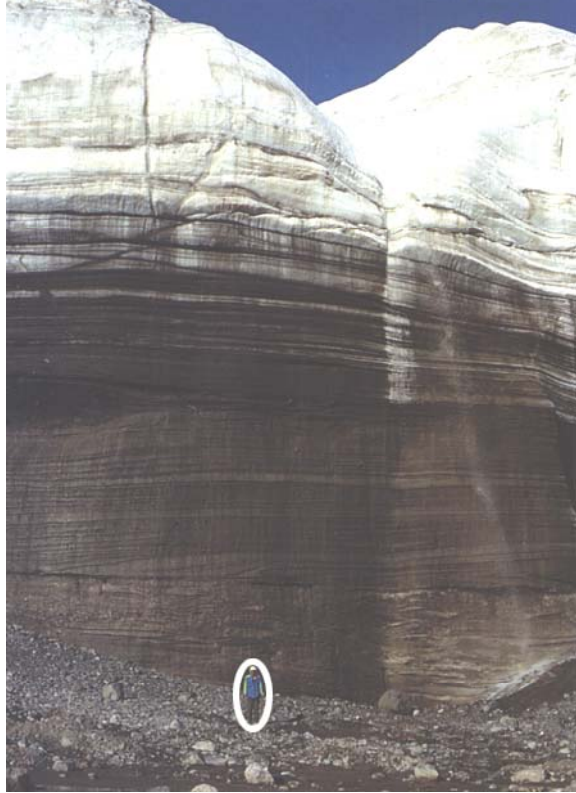


Figure 5. Basal ice in the subpolar Eugenie Glacier on Ellesmere Island with person in foreground for scale. From Benn and Evans [20] (Fig. 5.19).

Age of the Basal Unit: Underlying the BU is the Vastitas Borealis Formation which is about 3 By old [15,17]. The surface age of the polar cap deposits has been estimated to be at most 100 Ky old [11]. Overlying the basal unit and some dunes is the ice-rich latitudinally-dependent mantling layer [27,28]; no large craters have been found in this unit, so it assumed to be very young, Late Amazonian in age. Together, this evidence gives the BU an age of Early to Mid/Late Amazonian (0.1 – 3 By). It is difficult to absolutely date the BU itself since so little of its surface area is exposed. There are craters, better highlighted by MOLA data than by images, near the edge of the polar cap which may be BU craters covered by a thin layer of PLD. In addition, the floor of Chasma Boreale (CB) may consist of the lower BU layers [2, 4; Fishbaugh and Head, abstract in this volume]. This area has 3 large craters (~10 km diameter) and many smaller

craters. Crater counting of the CB floor could provide a better age estimate of the lower BU layers, but this is presumably only a small portion of the exposed surface area.

Conclusions: We have considered three possible origins and modifications of the north polar BU. Some characteristics of the BU are consistent with all of these. We look forward to the release of north polar THEMIS data to help us better characterize the unit. An obvious way to rule out an outflow channel/oceanic and/or eolian deposit origin for the BU would be to discover a similar unit in the south polar region. Preliminary examination of MOC images in the south polar region has yielded no evidence thus far for a basal unit, but we will continue to examine more south polar MOC and THEMIS images.

References: [1] Malin, M. and Edgett, K., *J. Geophys. Res.*, 106 (E10), 23,429-23,570, 2001. [2] Kolb, E. and K. Tanaka, *Icarus*, 154, 22-39 2001. [3] Byrne, S. and B. Murray, *J. Geophys. Res.*, 107 (E6), 10.1029/2001JE001615, 2002. [4] Edgett, K. et al., *Geomorphology*, in press, 2003. [5] Fishbaugh, K. and J. Head, *Brown U.-Vernadsky Microsymposium* [CD-ROM], 36, abstract MS019, 2002. [6] Fishbaugh, K. and J. Head, *Brown U.-Vernadsky Microsymposium* [CD-ROM], 36, abstract MS020, 2002. [7] Fishbaugh, K. and J. Head, *Lunar Planet. Sci.* [CD-ROM], XXXIV, abstract 1250, 2003. [8] Fishbaugh, K. and J. Head, *J. Geophys. Res.*, 105, 22,455-22,486, 2000. [9] Fishbaugh and Head, *Icarus*, 154, 145-161, 2001. [10] Fishbaugh, K. et al., *Lunar Planet. Sci.* [CD-ROM], XXXII, abstract 1426, 2001. [11] Herkenhoff, K. and J. Plaut, *Icarus*, 144, 243-255, 2000. [12] Baker et al., in *Mars*, ed. By H. Kieffer et al., 493-522, Univ. Ariz. Press, 1992. [13] Parker et al., *J. Geophys. Res.*, 98, 11,061-11,078, 1993. [14] Luchitta, B. et al., *Proc. Lunar and Planet. Sci. Conf. 17th*, Part I, *J. Geophys. Res.*, 91, suppl. E166-E174, 1986. [15] Tanaka, K. and D. Scott, *U.S.G.S. Misc. Inv. Ser. Map I-1802-C*, 1987. [16] Kargel, J. et al., *J. Geophys. Res.*, 100 (E3), 5351-5368, 1995. [17] Kreslavsky, M. and J. Head, *J. Geophys. Res.*, 105, 26,695-26,711, 2000. [18] Anderson, F. S. et al., *J. Geophys. Res.*, 104 (E8), 18,991-19,002, 1999. [19] Pollack, J. et al., *J. Geophys. Res.*, 95, 1447-1473, 1990. [20] Benn, D. and D. Evans, *Glaciers and Glaciation*, 193-197, Cambridge Univ. Press, 1998. [21] Knight, P., *Quat. Sci. Rev.*, 16, 975-993, 1997. [22] Alley, R. et al., *Quat. Sci. Rev.*, 16, 1017-1038, 1997. [23] Alley, R. et al., *J. Glaciol.*, 44, 563-569, 1998. [24] Roberts, M. et al., *Geology*, 30, 35439-442, 2002. [25] Cuffey, K. et al., *Geology*, 28, 351-354, 2000. [26] Fishbaugh and Head, *J. Geophys. Res.*, 107 (E3), 10.1029/2000JE001351, 2002. [27] Mustard, J. et al., *Nature*, 412, 411-414, 2001. [28] Kreslavsky, M. and J. Head, *Geophys. Res. Lett.*, 29 (15), 1719, 10.1029/2002GL015392, 2002.

TUNGSTEN ISOTOPIC COMPOSITIONS OF THE SNC METEORITES: FURTHER IMPLICATIONS FOR EARLY DIFFERENTIATION HISTORY OF MARS.

C. N. Foley¹, M. Wadhwa¹, and P. E. Janney¹,
¹Isotope Geochemistry Laboratory, Department of Geology, The Field Museum, 1400 S. Lake Shore Dr., Chicago, IL 60605, nfoley@fmnh.org.

Introduction: The hafnium-tungsten (¹⁸²Hf-¹⁸²W) short-lived chronometer ($t_{1/2} \sim 9$ Myr) has been used to date the timing of early metal-silicate differentiation events on the Earth, Moon, Mars (SNC parent body), and Vesta (eucrite parent body) [1-10]. Both hafnium and tungsten are highly refractory elements that are present in approximately chondritic relative abundances in bulk planets and planetesimals. However, during metal-silicate differentiation (or core formation), the lithophile Hf segregates into the silicate fraction while the siderophile W segregates into the metallic core. If this differentiation event occurs within ~ 5 half lives of ¹⁸²Hf, ~ 45 Myr, then its timing can be determined by measuring the excess of the daughter product, ¹⁸²W.

The Solar System initial ¹⁸²Hf/¹⁸⁰Hf ratio has recently been revised [7, 8, 9]. This has enabled new estimates for the timing of metal-silicate differentiation on the terrestrial planets and planetesimals. Core formation is now thought to have occurred within the first ~ 3 [7], ~ 13 [8], ~ 10 -29 [7], and ~ 29 [7] Myr from the beginning of Solar System formation for Vesta, Mars, Earth and the Moon, respectively. These time scales are significantly shorter than those determined previously for each of these planetary bodies [1, 6, 10]. A previous estimate of the Solar System initial ¹⁸²Hf/¹⁸⁰Hf ratio was derived from the W isotopic analyses of carbonaceous chondrites by [1, 2], which indicated an $\epsilon^{182}\text{W}$ value $\sim 2\epsilon$ units higher than the value recently reported by [7, 8, 9]. Since the only reported W isotopic measurements for SNCs are from [6], this raises the question as to whether these values are reproducible. Accurate determination of the W isotopic compositions of the SNC meteorites will help to constrain the timing of core formation on Mars and the extent of heterogeneity in the martian mantle.

Previous measurements indicate that whole rock $\epsilon^{182}\text{W}$ values in the SNCs vary from ~ 0 to $+3$ ϵ units above terrestrial [6]. Moreover, these values appear to correlate with initial $\epsilon^{142}\text{Nd}$ values for the SNCs that have been analyzed [11], suggesting that core formation and silicate differentiation on Mars occurred very early in the history of Mars, and that subsequently, the martian mantle has remained poorly mixed. Since these data were reported, numerous new SNC meteorites have been recovered, and Nd isotopic data are available for several of these [12, and references

therein]. Therefore, the goals of this study were to obtain new estimates of the range of $\epsilon^{182}\text{W}$ values in the SNC meteorites (by measuring the W isotopic compositions of not only those which were previously analyzed by [6] but also of new SNCs that have since been recovered) and to confirm the relationship between the $\epsilon^{182}\text{W}$ and initial $\epsilon^{142}\text{Nd}$ values. In this work, we report the W isotopic compositions of two basaltic shergottites, Zagami and Los Angeles, and one nakhlite, NWA 998. W isotopic analyses of additional SNCs are ongoing.

Methodology: The samples analyzed here were crushed with a clean agate mortar and pestle. Dissolution was performed by treatment with a 3:1 mixture of concentrated HF:HNO₃, followed by concentrated HNO₃, and samples were finally brought into solution in HCl. Isolation of W from samples was performed with column chromatography using AG-1X8 anion exchange resin (200-400 mesh). The chromatography procedure is similar to that used by [9, 13, 14]. Primary and secondary column chemistry was performed. The secondary column was necessary mostly to reduce the amount of Ti in the W-cut from the primary column. After the secondary clean-up column, the W-cut was evaporated and re-dissolved in 3% HNO₃-0.05 N HF for isotopic analysis.

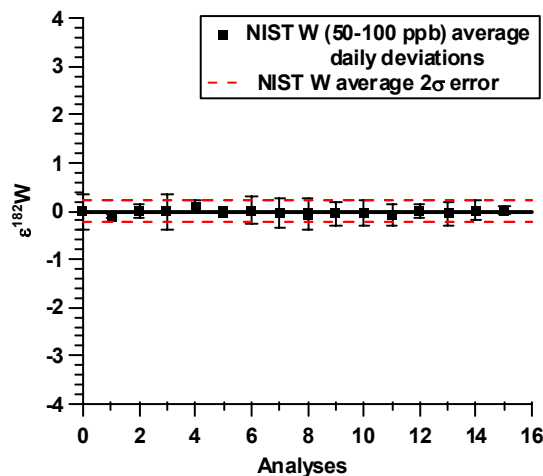
W isotopic analyses were made using the Micro-mass IsoProbe multicollector ICPMS in the Isotope Geochemistry Laboratory at the Field Museum. The normalizing ratio used to correct the raw ¹⁸²W/¹⁸³W ratio for instrumental mass fractionation was ¹⁸⁶W/¹⁸⁴W = 0.927633 [3]. As a check, we also determined the fractionation corrected ¹⁸²W/¹⁸³W ratio by normalizing to a ¹⁸⁴W/¹⁸³W ratio of 2.139758 [15]. For all samples analyzed here, within 2σ errors, the $\epsilon^{182}\text{W}$ values for respective samples were the same using both normalization schemes. Sample solutions (typically with W concentrations of ~ 50 -100 ppb) were introduced into the plasma using a CETAC Aridus MCN. The array of 9 Faraday collectors allowed simultaneous collection of all W isotopes. Each measurement was comprised of 40 cycles of 10 s integrations, and was preceded by a 10-minute washout and a 45 s integration of the background. Measurement of each sample was bracketed with multiple measurements of the NIST 3163 W standard. For each sample,

at least 2 repeat measurements were performed interspersed with measurements of the NIST 3163 W standard. The $\epsilon^{182}\text{W}$ value for each sample was the average of the calculated differences between each sample measurement and the average of repeated measurements of the NIST 3163 W standard bracketing that sample in epsilon (ϵ) units as shown below.

$$\epsilon_{182\text{W}} = 10^4 \cdot \left(\frac{\left(\frac{^{182}\text{W}}{^{183}\text{W}} \right)_{\text{Sample}} - \left(\frac{^{182}\text{W}}{^{183}\text{W}} \right)_{\text{NIST 3163 Standard}}}{\left(\frac{^{182}\text{W}}{^{183}\text{W}} \right)_{\text{NIST 3163 Standard}}} \right)$$

Results: Measurements of the W isotopic composition of the NIST 3163 standard were performed over the course of several months. Figure 1 shows the results of these analyses for the last ~2 months. Each data point consists of the average $\epsilon^{182}\text{W}$ value obtained from repeat measurements of the NIST 3163 standard performed on a single day. As shown in the figure, the long term reproducibility (2σ) of our W isotopic measurements is $\sim 0.2 \epsilon$.

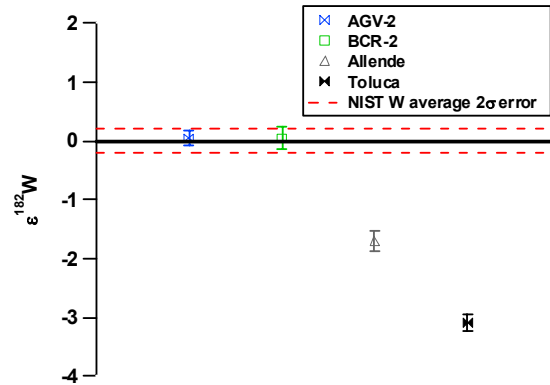
Figure 1: Long term reproducibility of W isotopic measurements of the NIST 3163 standard.



W isotopic compositions of geostandards as well as previously analyzed meteorites were also measured to verify the accuracy of our experimental techniques. Terrestrial USGS andesite and basalt geostandards, AGV-2 and BCR-2 respectively, were first analyzed. As shown in Figure 2, the W isotopic compositions of AGV-2 and BCR-2 are, within errors, the same as those of the NIST 3163 standard represented by the solid line $\pm 2 \sigma$ (dashed lines). The $\epsilon^{182}\text{W}$ values de-

termined by us of the carbonaceous chondrite Allende and the iron meteorite Toluca (Figure 2) are similar, within errors, to values reported for these meteorites by [7, 8] (Table 1). In contrast, our results for Allende are not consistent with those acquired by [1,2].

Figure 2: $\epsilon^{182}\text{W}$ values for AGV-2, BCR-2, Allende, and Toluca relative to the terrestrial W standard NIST 3163 $\pm 2\sigma$ external errors.

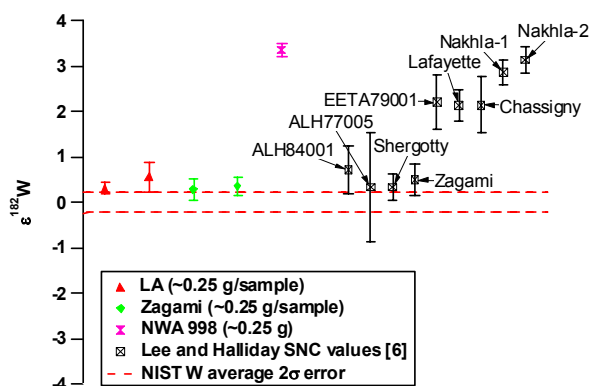


Our results for the SNC meteorites are similar to those acquired by [6], as illustrated in Figure 3. Specifically, the $\epsilon^{182}\text{W}$ value of 0.32 ± 0.18 (2σ) determined by us for Zagami is, within error, the same as that reported for this meteorite by [6]. The basaltic shergottite Los Angeles, which has not been analyzed prior to this work, has an $\epsilon^{182}\text{W}$ value of 0.43 ± 0.12 (2σ). This value is similar to that reported by [6] for other basaltic shergottites, Shergotty and Zagami, that have petrologic and geochemical similarities to Los Angeles. NWA 998, a nakhlite which also has not been analyzed prior to this work, has an $\epsilon^{182}\text{W}$ value of 3.35 ± 0.14 (2σ), similar to that of Nakhla [6].

Table 1: Average $\epsilon^{182}\text{W}$ values $\pm 2\sigma$.

Sample	$\epsilon^{182}\text{W}$ (this work)	2σ error	$\epsilon^{182}\text{W}$ (previous work)	2σ error
NIST W	0.01	0.17		
AGV-2	0.04	0.13		
BCR-2	0.05	0.20		
Allende	-1.7	0.17	-1.9 ^[7,8]	0.20 ^[7,8]
Toluca	-3.09	0.13	-3.16 ^[7]	0.15 ^[7]
LA	0.43	0.12		
Zagami	0.32	0.18	0.50 ^[6]	0.34 ^[6]
NWA 998	3.35	0.14		

Figure 3: $\epsilon^{182}\text{W}$ values for Los Angeles(LA), Zagami, and NWA 998 (this work) compared with the data of Lee and Halliday for various SNCs [6].



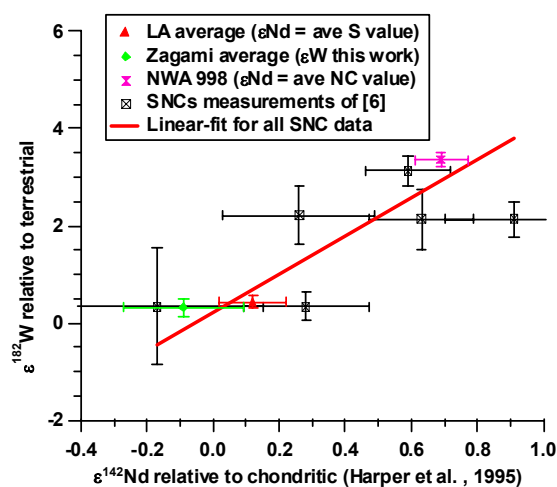
Discussion: Assuming an initial Solar System $^{182}\text{Hf}/^{180}\text{Hf}$ ratio of $(1.09 \pm 0.09) \times 10^{-4}$ [7, 8], a Hf/W ratio for the martian mantle of ~ 5 [16, 17], and a simple two-stage model for differentiation on Mars, it is possible to estimate the timing of core formation (provided that the measured ^{182}W excesses in the SNC meteorites are solely the result of this process). Given the above assumptions, one may estimate ΔT_{CHUR} values (or timing of core formation relative to Solar System formation) of ~ 12 -13 Ma from the W isotopic data for Zagami and Los Angeles and ~ 1.5 Ma from the data for NWA 998. However, it is significant to note that the W isotopic compositions of all the SNC meteorites are unlikely to be solely the result of core formation and may additionally be affected by silicate differentiation. This is suggested by the apparent correlation between the $\epsilon^{182}\text{W}$ and $\epsilon^{142}\text{Nd}$ values that was first noted by [6]. During core formation, Hf (lithophile) is fractionated from W (siderophile) whereas Sm and Nd (both lithophile) do not fractionate from each other. However, during crust-mantle differentiation, Hf/W ratios as well as Sm/Nd ratios are fractionated in the two silicate reservoirs. Therefore, if the correlation between $\epsilon^{142}\text{Nd}$ and $\epsilon^{182}\text{W}$ values in the SNCs can be further confirmed, it would indicate that on Mars, core formation and silicate differentiation both occurred when the short-lived radionuclides ^{182}Hf ($t_{1/2} \sim 9$ Myr) and ^{146}Sm ($t_{1/2} \sim 103$ Myr) were both extant.

Figure 4 shows a plot of $\epsilon^{182}\text{W}$ vs. $\epsilon^{142}\text{Nd}$ values in the SNC meteorites (including those analyzed by us). If we assume that the ^{142}Nd excesses in Los Angeles and in NWA 998 are similar to those in the basaltic shergottites (Shergotty and Zagami) and in the nakhlites, respectively, then the correlation between

$\epsilon^{182}\text{W}$ and $\epsilon^{142}\text{Nd}$ noted earlier by [6] appears to be robust. Therefore, this provides further confirmation that core formation and silicate differentiation occurred very early in the history of Mars.

It is notable here that the SNCs with the least radiogenic W and near chondritic Nd isotopic compositions (i.e., the basaltic shergottites Shergotty, Zagami, and Los Angeles) have ^{182}W excesses that are still ~ 2.2 ϵ units above the revised chondritic value determined by [7, 8, 9]. This provides an upper limit on the timing of core formation on Mars of ~ 13 Myr and furthermore suggests that core formation preceded silicate differentiation.

Figure 4: $\epsilon^{182}\text{W}$ vs. $\epsilon^{142}\text{Nd}$ in the SNC meteorites. $\epsilon^{182}\text{W}$ values are from this study and from [6], while $\epsilon^{142}\text{Nd}$ are from [15]. The $\epsilon^{142}\text{Nd}$ values shown here for LA and NWA 998 are average values, reported by [15], for shergottites (S) and nakhlites/chassignites (NC) respectively.



References: [1] Lee D. C. and Halliday A. N. (1995) *Nature*, 378, 771-774. [2] Lee D. C. and Halliday A. N. (1996) *Science*, 274, 1876-1879. [3] Lee D. C. and Halliday A. N. (1997) *Science*, 278, 1098-1103. [4] Halliday A. N. and Lee D. C. (1999) *GCA*, 63, 4157-4179. [5] Halliday A. N. (2000) *EPSL*, 176, 17-30. [6] Lee D. C. and Halliday A. N. (1997) *Nature*, 388, 854-857. [7] Yin Q. et al. (2002) *Nature*, 418, 949-952. [8] Kleine T. et al. (2002) *Nature*, 418, 952-955. [9] Schoenberg R. et al. (2002) *GCA*, 66, 3151-3160. [10] Quitté G. et al. (2000) *EPSL*, 184, 83-94. [11] Harper C. L. et al. (1995) *Science*, 267, 213-217. [12] Nyquist L. E. et al. (2001) in *Chronology and Evolution of Mars, Space Science Series of ISSI*, Ed. Kallenbach et al. 105-164. [13] Münker C. et al.

(2001) *Geochem. Geophys. Geosys.*, 2. [14] Kraus K. A. et al. (1955) *J. Am. Chem. Soc.*, 77, 3972-3977. [15] Harper C. L. Jr. and Jacobsen S. B. (1996) *GCA*, 60, 1131-1153. [16] Palme H. and Beer H. (1993) in *Landolt-Börnstein Group VI, Astronomy and Astrophysics* Vol. 3a, *Instruments; Methods; Solar System* (ed. Voigt, H. H.) 196-221. [17] Kong P. et al. (1999) *Geochim. Cosmochim. Acta*, 63, 1865-1875.

SCENARIOS TO EXPLAIN THE FORMATION OF GULLIES ON MARS : NUMERICAL SIMULATION WITH A CLIMATE MODEL. F. Forget¹ N. Mangold² and F. Costard², ¹LMD, CNRS, Université Paris 6 BP99, 4, place Jussieu, 75252 Paris cedex 05, France (forget@lmd.jussieu.fr) ²Orsay-Terre, FRE2566, CNRS et Université Paris-Sud, Bat. 509, 91405 ORSAY Cedex, France

Introduction: The observations of geologically young gullies [1] in the middle and high latitude on Mars are among the most debated topics in Martian science. Most scientists believe that their formation involved liquid water, but current temperature and pressure conditions on Mars are too low to allow liquid water or debris mixed with liquid water to freely flow on the surface.

Possible Scenarios

Gullies have been proposed to result of subsurface seepage of water [1] by geothermal activity [2] or brines [3], near-surface ice melting at recent periods of high obliquity [4], snowmelt in more recent periods [5]. One of the best constrain to test the various possible scenarios are the spatial distribution and the orientation of the slope on which gullies can be observed (Figure 1). The first two scenarios are somewhat difficult to reconcile with observed distribution. There is no clear association between the location of debris flows and the general distribution of recent geothermal activity [1]. Furthermore, gullies originating from the top of isolated peak and from the crest of large dark dunes [6] have been observed. In these cases, the involvement of a subsurface aquifer is unlikely.

Formation of Gullies at high obliquity

The formation of the observed gullies can be several hundred thousand or even several million years old. Therefore, when considering the possible origin of the Martian Gullies, one has to consider how Mars could have been at other obliquities.

In a previous work [4] we have explored the possibility that the gullies could be formed by the melting of the near-surface when the obliquity was different than today. Using the climate model developed at LMD, we calculated the temperature of the surface and subsurface on various locations on Mars and for various obliquities. We also included the ability to compute the climate on various slopes with various orientation, which is of key importance here.

Our calculations revealed that the only places on Mars where the daily mean temperature has been above the melting point of water during the past obliquity cycles are the mid and high latitudes above 30°, especially on poleward-facing slopes, except in the polar region where warm temperatures are found on both southward and northward facing slopes. The corresponding ther-

mal wave could have melted the ground ice over several tens of centimeters. The fact that poleward-facing slopes receive more sunlight and get warmer at high obliquity in the summer is due to the pole being tilted toward the sun (In the southern hemisphere around summer solstice, the sun appears most of the time in the southern sky).

This preferential orientation and the latitudinal distribution of the warmest near-surface temperature coincide with the location of the observed Martian gullies, suggesting a link between near-surface warming and debris flows. We have performed a detailed statistical analysis of the gullies orientations as observed in the most recent MOC pictures (M01 to E06, Fig. 1) We found a very good agreement between the variations of the orientation of the gullies with latitude observed on mars and those predicted by the model.

It must be noted that, even though the poleward facing slopes can get very warm around summer solstice at high obliquity, they remain colder on a yearly average than any other exposition. For instance, at 35° obliquity, a 30° poleward slope receives about 100 W m⁻² along the year, compared to almost 150 W m⁻² on a flat surface. When studying other aspect of the climate system like the CO₂ cycle and the water ice cycle, this means that both CO₂ ice and water ice tends to be more stable on such slopes. This strongly favours the formation of gullies.

For instance, around summer solstice, any near-surface ground (or ice layer) which is progressively warmed toward 0°C tends to sublime or lose its water trapped in its pores through the diffusion of H₂O molecules into the atmosphere. However, on poleward-facing slopes, the seasonal CO₂ ice layer accumulated during fall and winter maintains the surface at the low CO₂ frost point temperature until late spring (see Fig. 3 in [4]). These slopes are covered by seasonal CO₂ ice later in the season than other slopes, and get free of ice only in summer when the solar flux is already strong. The disappearance of CO₂ ice allows a sudden warming of the surface and of the near sub-surface which reach 0°C in a few days. If any water ice is present on the surface or in the soil, it have less time to completely sublime or diffuse out of the ground, especially since the atmosphere water content is then near its peak (diffusion primarily depends on the ground – atmosphere water density gradient). In addition, poleward

slopes act as cold trap for the water ice sublimed for nearby area, and this also favour the accumulation of ice before they get warm.

On this basis, and since Mars at high obliquity is thought to have had a water-rich atmosphere thicker than today (so that liquid water could sometime flow on the surface), we believe that the Mars gullies result from the melting of the ground ice at high obliquity. Figure 2 presents a summary of the environmental conditions on poleward facing slope at high obliquity that may have enable the formation of gullies.

Ultimately, the key question that remains to be solved is how much water can be available on the surface or in the subsurface at high obliquity, and whether the ice layer can actually accumulate in the relevant locations. On the one hand, the Mars Odyssey GRS records suggest that significant amount of water ice is currently accumulated in the high latitude subsurface. On the other hand, recent Global Climate Model simulations performed by several major GCM team (NASA Ames : Bob Haberle, GFDL-Caltech : M. Mischna, M. Richardson and R. J. Wilson, we at LMD) shows that at high obliquity the Martian climate was extremely "wet", and that, for instance; water ice or snow may have accumulated in the mid-latitudes. This should be especially true on poleward facing slopes.

Formation of Gullies under snowpack

Recently, Christensen [5] suggested that the gullies could form presently below snow-covered slopes through erosion by water melt beneath the dusty snow. The main motivation for this scenario was the observations of smooth mantle (thought to be a water ice snow pack covered by sediment) immediately next to gullies. According to P. Christensen, the water was transported from the poles to mid-latitudes during period of high obliquity. Patches of snow remain today on the cold poleward facing slope where they form gullies, thus explaining why gullies would be preferentially found on poleward-facing slopes.

However, this model does not fully address how liquid water can form beneath the snow, reach the surface and erode the substrate. Christensen based his scenario on calculations performed by Clow [7] using an optical-thermal model developed for dusty snow at 38° south latitude. However, in this paper, it is shown that it is relatively difficult to melt snow on current Mars (with a pressure of 7 mbar, this requires a very specific type of snow) and that liquid water would be available for run off at atmospheric pressures well above 7 mbars. Moreover, the calculations are performed on a flat surface. On a poleward facing slope on present Mars, melting the ice would be even less likely. For instance, the maximum clear sky solar flux reaching -38° latitude

on present Mars is about 700 W.m⁻² on a flat surface compared to only 525 W m⁻² on a 30° poleward slope (and only 420 W m⁻² at 50 deg latitude, where many gullies are observed).

If the smooth deposit discovered near some gullies are indeed the remnant of a snow pack that accumulated there during high obliquity period, it is more than likely that in some location the same snow could quite easily melt, but, as explained above, at obliquity higher than today. The melted snow would have then impregnate the debris observed on the surface, and form debris flows as described in [4]. Such a process would be very close to what is observed for Earth periglacial debris flows. It must be reminded here that the geomorphological characteristics of most Martian gullies, with levees and accumulations of debris at their base, do suggest that they are formed by debris flows rather than a slow erosion by little water flowing beneath a snow pack. At high obliquity, water do not need to be sheltered from rapid evaporation because the pressure is expected to have been higher than today and probably above the triple point of water thanks to the desorption of CO₂ from the regolith [5].

Conclusion

During our talk, we will review the different clues that are now available to constrain the possible scenarios that explain the formation of Gullies, and in particular present new calculations of the environmental conditions (temperature, water ice accumulation and sublimation) on various slopes and at various obliquity

References:

- [1] Malin, M. C. and K. S. Edgett, *Science*, 288, 2330-2335, 2000
- [2] Hartmann, W. K., *Space Sci Rev.*, 1-6, 2000
- [3] Knauth, L. P. and D. M. Burt, *Icarus*, 267-271, 2002
- [4] Costard, F. and F. Forget, N. Mangold and JP Peulvast, *Science*, 295, 110-113, 2002
- [5] Christensen P. R., *Nature*, doi10.1038-01436, 2003
- [6] Mangold, N. F. Costard and F. Forget, *J.G.R.*, in press
- [7] Clow, G. D. , *Icarus* 72, 95-127 (1987)
- [8] H. H. Kieffer, A. P. Zent, in Mars, H. H. Kieffer, B. M. Jakosky, C. W. Snyder, M. S. Matthews, Eds, University of Arizona press (1992).

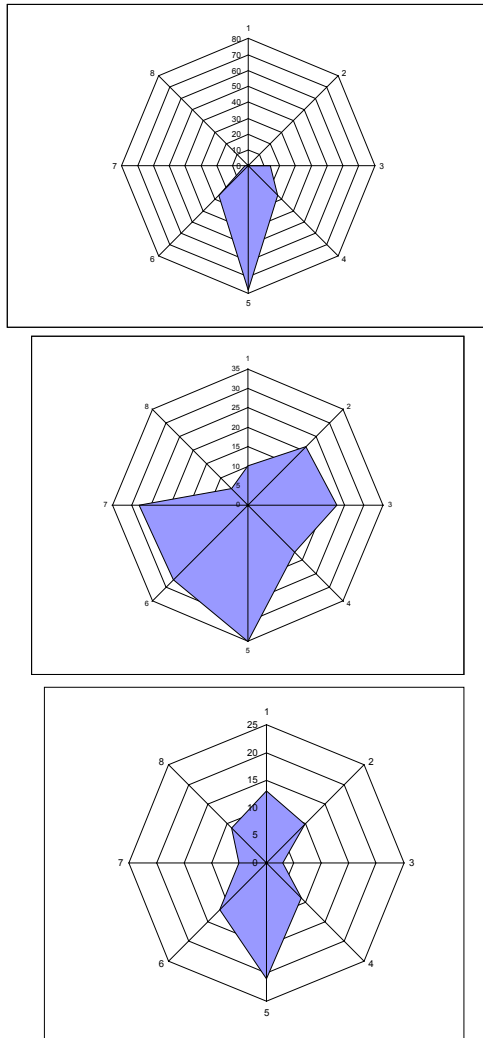


Figure 1 : Distribution of the orientation of martian gullies in three ranges of latitude in the southern hemisphere: None are observed equatorward of 28° of latitude. Statistics are made over all MOC images from data archives M01 to E06. The total number of gullies is 395, respectively 146, 167 and 82 in each latitude range. Orientations have been divided in 8 sectors of 45° large (S is centered at 180° , including directions from 157.5 to 202.5°). S means that gullies face the southern direction (the pole) on hillslopes oriented along the E-W direction. The number of octagons corresponds to the number of gullies in each of the eight sectors.

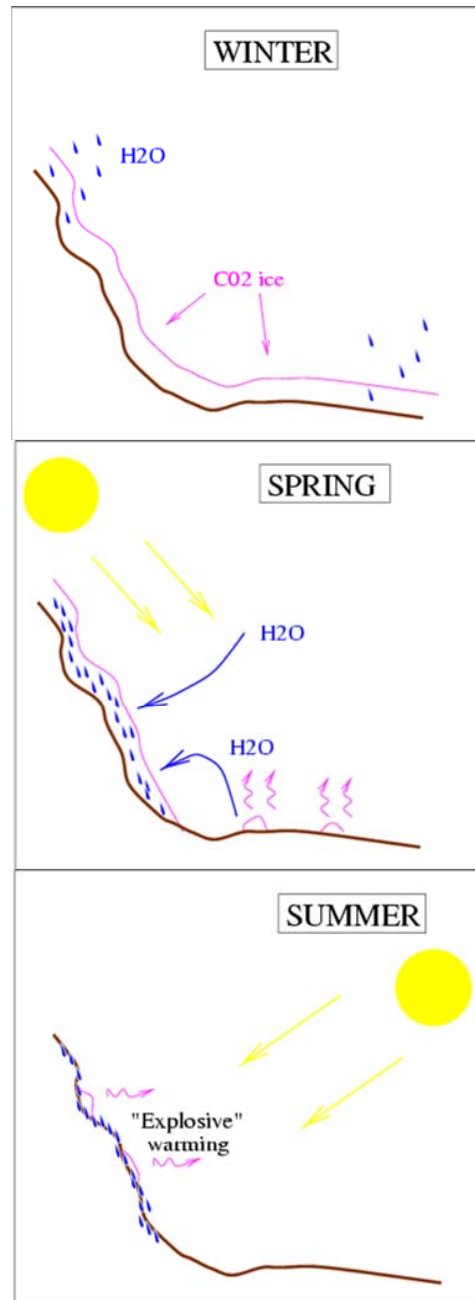
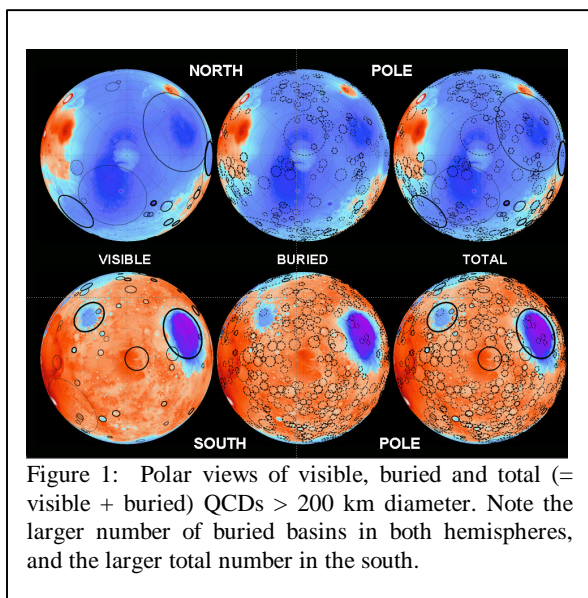


Figure 2: Schematic drawing of the environmental conditions on poleward facing slopes at mid latitude when Mars obliquity is higher than 30° which are thought to favour the formation of gullies.

BURIED IMPACT BASINS AND THE EARLIEST HISTORY OF MARS. H. V. Frey, Geodynamics Branch, Goddard Space Flight Center, Greenbelt, MD 20771, Herbert.V.Frey@nasa.gov.

Introduction: The “Quasi-Circular Depressions” (QCDs) seen in MOLA data which have little or no visible appearance in image data have been interpreted as buried impact basins on Mars [1,2]. These have important implications for the age of the lowland crust, what mechanisms could produce the crustal dichotomy, and the existence of crust older than the oldest observed surface units on Mars [3,4]. A global survey of large QCDs using high resolution MOLA data now available [5,6] has provided further details of the earliest history of Mars. The lowlands are of Early Noachian age, slightly younger than the buried highlands and definitely older than the exposed highland surface. A depopulation of large visible basins at diameters 800 to 1300 km suggests some global scale event early in martian history, maybe related to the formation of the lowlands and/or the development of Tharsis. A suggested early disappearance of the global magnetic field can be placed within a temporal sequence of formation of the very largest impact basins.

QCDs > 200 km Diameter: Figure 1 shows polar views of QCDs > 200 km diameter. The diameter cut-off for this global survey was motivated by several factors: (a) the total number found (~560) was tractable; (b) features of this size are difficult to bury completely (rim heights 1-1.5 km, depths ~4 km [7]) and therefore might be expected to survive over all of martian history; and (c) this is an appropriate size for comparison with other data such as the distribution of gravity and magnetic anomalies [8-10].



The buried population is much greater than the visible population in both the northern lowlands and in the southern highlands. The density of all (visible+buried) basins is also much greater in the highlands than in the lowlands, by roughly a factor 4 (much larger than their areal ratio).

There is a significant population of very large basins ($D > 1000$ km), equally divided between the two hemispheres, including two Utopia-size buried features. One is near but not identical to an earlier proposed “Daedalia Basin” [11,12] and the other centered near 4N, 16W. This “Ares” basin has independent support. The Uzboi-Ladon-Arden Valles through Margaritifer-Iani Chaos depressions form a nearly continuous northward channel system that is radial down toward the exact center of the Ares Basin. Ares Vallis itself drains exactly radially away from this center NW into Chryse.

Cumulative Frequency Curves and Crater Retention Ages: Global and separated highland/lowland cumulative frequency curves show similar characteristics. There is a small (~10) population of very large basins ($D = 1300-3000$ km) which follow a -2 power law slope on the log-log cumulative frequency plots. At $D < \sim 500$ km the total populations in both highlands and lowlands again follow a -2 slope; for the planet-wide visible population this is the same slope as for the very large diameter basins. On a regional basis, the total lowland population for $D < 600$ km lies above the visible highland population, but below the buried (and total) highland population. This suggests that globally the buried lowland crust is slightly younger than the original (now buried) highland crust.

This is consistent with our earlier result that the buried lowlands were older than the visible highlands in the extended “Arabia” area [2] and that, based on direct comparison with the oldest exposed surface units on Mars (Nh_1 , SE of Hellas [3,4]), the buried lowland crust is Early Noachian in age [13].

At intermediate diameters (1300 to about 800 km) the global visible population of falls off the -2 slope before recovering at smaller diameters. The visible and total populations of the highlands have a similar depletion, but the buried population in the highlands does not. We speculate that this depletion of intermediate size basins is the signature of some global-scale event very early in martian history. Candidates are the formation of the slightly younger lowlands, and the

growth of Tharsis, both of which could have removed pre-existing intermediate-size basins.

Implications for the Age and Origin of the Crustal Dichotomy: Unless there is some way to preserve the large population of Early Noachian (now buried) impact craters while lowering the crust in the northern third of Mars, it appears the lowland crust not only formed in the Early Noachian but also became low during that time [2,13]. The slight crater age difference (which could be a very short absolute time interval), does suggest the lowlands formed after the highlands were in place and preserving craters. It may be hard to form the lowlands by endogenic processes in the short time available. Most mechanisms suggested [14-16] have a relatively late formation of the lowlands. Even if degree one convection does occur, it appears to take hundreds of millions of years to become established, even with extreme viscosity gradients [16]. Three large “lowland-making” QCDs (Utopia, Acidalia and Chryse) do not account for all the lowland area of Mars, but are responsible for much of it and provide a simple mechanism for the early formation of a topographic dichotomy on Mars [7].

Comparison with Magnetic Anomalies: We compared the distribution of QCDs (both buried and visible) with the distribution of magnetic anomalies, both modeled [17,18] and directly observed [9,10]. As shown in Figure 2, most of the very large basins do not have prominent magnetic anomalies lying within

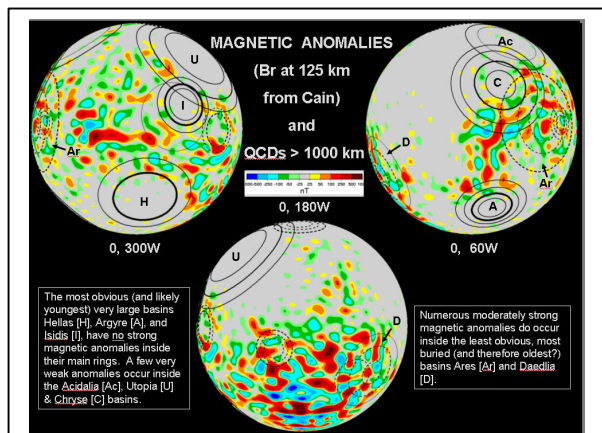


Figure 2. Crustal magnetic anomalies from Cain [11] with QCDs > 1000 km diameter superimposed. Note only Daedalia [D] and Ares [Ar] have prominent anomalies lying inside their main (darker) rings. These two may have formed when the global magnetic field was still present.

their main ring, as had been previously suggested for the Hellas and Argyre Basins [9,19]. This is also true for many of the less obvious large basins detected in this study, and consistent with earlier suggestions that

these basins may have formed after the global dynamo died [9,19]. But two very large basins, Daedalia and Ares, do have prominent anomalies lying within their main rings (Figure 2). These two are also the oldest of the population, based on their much more subdued nature and larger number of superimposed smaller basins. Daedalia and Ares likely predate the disappearance of the global magnetic field. The “lowland-making” basins Utopia, Acidalia and Chryse have a few moderate amplitude anomalies within their main ring, and based on superposed smaller basins appear to be of intermediate age between Ares and the younger Hellas, Argyre and Isidis basins (see below).

A Chronology of Major Events in the Early History of Mars: We use the cumulative number of basins larger than 200 km diameter per million square km [N(200)] to place the large diameter basins in a chronology (Figure 3). The highland total N(200) age is [4.53]. The very ancient Ares Basin is slightly older [3.98] than the buried highland surface [3.89]. The three basins which contribute most to the topography of the lowlands (“lowland-making” basins Acidalia, Utopia, and Chryse), are all older [N(200) ~ 3.12-3.27] than the buried and total lowland crust [2.39-2.47], as they should be. Argyre [2.21] and Isidis [1.39] formed after the lowland crust, but Hellas [2.68] may have formed before.

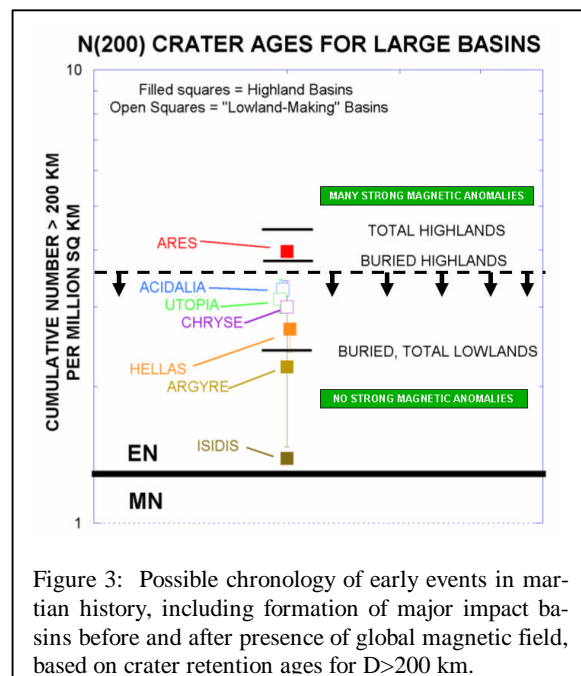


Figure 3: Possible chronology of early events in martian history, including formation of major impact basins before and after presence of global magnetic field, based on crater retention ages for D>200 km.

Another age of interest in this chronology can be derived by extrapolation from the largest impact basins, which, before the depopulation at D<1300 km,

roughly follow a -2 powerlaw. Extending this to $D=200$ gives an $N(200)$ age of $\sim 6-8$, significantly older than the buried and total highlands. This probably represents the oldest $N(200)$ age that can be estimated, but is not oldest age on Mars. There must be still older crust if the oldest large basins are preserved as recognizable structures (see discussion below).

The relative basin sequence is fairly secure and consistent with regional ages based on counts of superimposed impact basins. The line dividing the magnetic field/no-magnetic field eras is less so. We place it at $N(200) \sim 3.5$, before the formation of the “lowland-making” basins. The few weak anomalies in Utopia, Acidalia and Chryse may represent partial remagnetization of the crust in a dying field following formation of these intermediate age basins. This is an extension of the idea that basins without anomalies formed after the field disappeared [9,19]. If some process other than impact demagnetized the crust [e.g., 20], then this line could be substantially lower in Figure 3 and later in martian history.

The scheme described above is a relative chronology, loosely constrained by cumulative frequency data for QCDs of large size. It does not, except through modeling studies, provide information on absolute ages or dates for major events. Buried impact basins do provide some information on the limitations on our ability to estimate absolute ages, as described below.

Pre-Noachian Crust?: The “Early Noachian” (EN) used in geologic mapping [21-23] is undefined at the early end, but it is often assumed in absolute chronologies [24,25] to extend back to 4.6 BYA. This assumption was explored by searching for evidence of buried impact basins, [3,4] in the largest occurrences of Early Noachian terrain. If such basins exist, they indicate crust which must pre-date the surface units mapped as the oldest on Mars, and those units must then be less than 4.6 BY old. We show that such older basins and crust do indeed exist. Also a number of Noachian terrains on Mars appear to have a common total (visible + buried) crater retention age. This might be either the age of an original (planet-wide?) crust of Mars, or may indicate crater saturation.

Buried Basins near Hellas and Isidis: The two largest occurrences of EN materials on Mars are the basin rim materials of Hellas (Nh_1 , about 1.2 million sq. km) and Isidis (Npl_1 , about 0.6 million sq km). We searched MOLA data for Quasi-Circular Depressions (QCDs) >25 km diameter in the Hellas [3,4] and >15 km in the Isidis [4,26] areas, and found a significant population of QCDs not visible on images that we assume are buried impact basins. Cumulative frequency curve shape supports this assumption.

The total (cumulative) population near Hellas is about 1.6 times the visible population [3,4]. Isidis [4,26] shows a total population about 3-3.5 times the visible population over the same diameter range. Our counts suggest Isidis rim material is younger than Hellas rim material in terms of visible crater populations, but has a larger buried population. The total cumulative populations for Hellas and Isidis rim materials are similar, implying a common age older than the Early Noachian visible crater retention age.

Total Populations Compared: Figure 4 compares these total populations with other Noachian units, including MN Npl_1 near Hellas and a very large “Arabia” area (~ 17 million sq km, average MN age) used previously for comparison with our lowland study [2]. Because of its very large area, the “Arabia” statistics are very good, and the “Arabia” total population closely follows a -2 power law over the entire diameter range 50-500 km. Over a more limited range where their smaller area statistics are also good, the total population curves for EN terrain at Isidis and for EN and MN terrain at Hellas closely overlap and follow the same -2 slope as for “Arabia”. In all three regions, despite radically different sampling areas, the total crater retention age is similar.

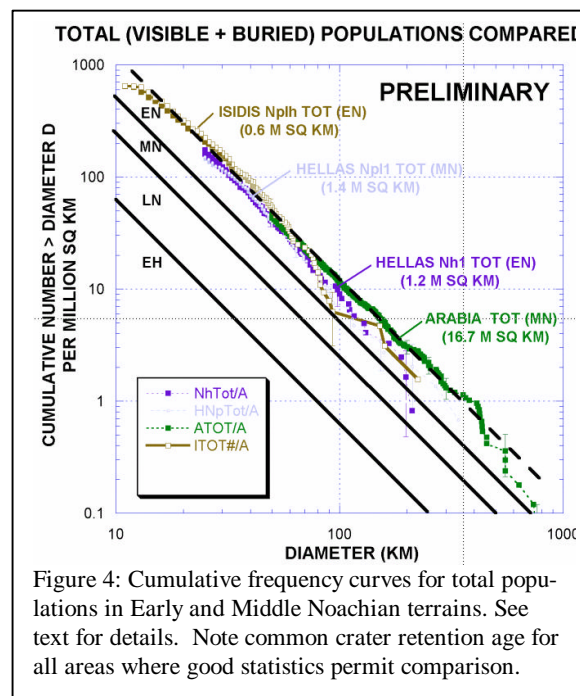


Figure 4: Cumulative frequency curves for total populations in Early and Middle Noachian terrains. See text for details. Note common crater retention age for all areas where good statistics permit comparison.

Similar total crater retention ages could suggest either (a) a common age for the underlying surface which, if not the age of the primordial crust on Mars, is certainly older than the surface units mapped as Early Noachian, or (b) crater saturation [4,26]. To

test the second of these we show in Figure 5 the same total population data in an incremental frequency plot and compare it with curves of martian ages from [25].

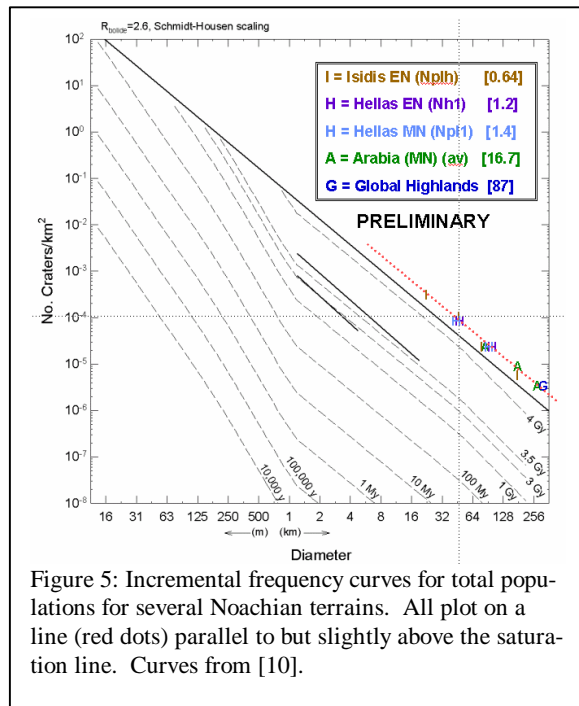


Figure 5: Incremental frequency curves for total populations for several Noachian terrains. All plot on a line (red dots) parallel to but slightly above the saturation line. Curves from [10].

Over the diameter ranges for which we have data the total population points define a straight line (red in Figure 5) which parallels a saturation curve, but lies above it. However, the curves in Figure 5 depend on a number of model assumptions, especially the scaling factor R . The absolute ages shown are probably accurate to a factor 2 [27]. Note our data does lie within a factor 2 of the saturation line in Figure 5. The total population data shown here may well indicate saturation in the underlying crust [13,26]. It is interesting to speculate that data such as presented here, if supported by similar results from other Noachian terrains around Mars, might be used to “calibrate” the model curves.

Conclusions: Buried impact basins on Mars provide evidence that: (1) The buried lowland crust is Early Noachian in age, slightly younger than the buried highlands but definitely older than the exposed highland surface. This constrains the mechanisms by which the crustal dichotomy formed and favors those which operate very early and very quickly. Impact processes may have been the cause of the lowlying topography in many areas. (2) Very large visible basins show a depopulation (relative to a -2 power law) at intermediate diameters (1300 down to about 800 km) that may be the signature of some early global scale event. The formation of the lowlands or Tharsis

(or both) are obvious candidates. (3) While most very large impact basins have few or no strong magnetic anomalies inside their main rings, the two oldest (based on superposed smaller basins) do have prominent anomalies, suggesting they formed before the global magnetic field died. Weak anomalies in the “lowland-making” basins may indicate partial remagnetization in a dying field following formation of these intermediate age basins. (4) The oldest visible surface units are not the oldest crust and cannot date from 4.6 billion years ago. There is a “pre-Noachian” history recorded by buried basins found underlying the oldest visible terrains on Mars. (5) A number of old terrains appear to have similar total population crater retention ages, which could be a common-age earlier crust or could indicate saturation cratering.

References. [1] Frey, H. et al., GRL 26, 1657-1660, 1999. [2] Frey, H. et al., GRL 29, 10.1029 /2001 GL013832, 2002. [3] Frey, E.L. and H.V. Frey, AGU Paper P32A-01. [4] Frey, H. et al., LPSC 34 abstract #1848, 2003. [5] Frey, H., GSA Fall 2002 Meeting paper 26-3, 2002. [6] Frey, H. LPSC 34, abstract # 1838, 2003. [7] Garvin, J.B. et al. LPSC 33, abstract 1255, 2002. [8] Smith, D.E. et al., Science 286, 94-97, 1999. [9] Acuna, M.H., et al., Science 284, 790-793, 1999. [10] Connerney, J.E.P. et al., GRL 28, 4015-4018, 2001. [11] Craddock, R.A. et al., JGR 95, 10729-10741, 1990. [12] Schultz, R. A. and H.V. Frey, JGR 95, 14,175-14,189,1990. [13] Frey, H. et al. LPSC abstract #1680, 2002. [14] Wise, D.U. et al., JGR 84, 7934-7939, 1979. [15] McGill, G.E. and A.M. Dimitriou, JGR 95, 12595-12605, 1990. [16] Zhong, S. and M.T. Zuber, Earth Planet. Sci. Lettr. 189,75-84,2001. [17] Purucker, M.E. et al., GRL 27, 2449-2452, 2000. [18] Cain, J. unpublished data, 2001. [19] Hood, L.L. et al., LPSC 33, abstract #1125, 2002. [20] Solomon, S.C. et al., LPSC 34, abstract #1382, 2003. [21] Scott D. H. and K. L. Tanaka, U.S.G.S. Misc. Inv. Series Map I-1802-A , 1986. [22] Greeley, R. and J. E. Guest, U.S.G.S. Misc. Inv. Series Map I-1802-B, 1987. [23] Tanaka, K. L. and D. H. Scott, U.S.G.S Misc. Inv. Series I-1802-C, 1987. [24] Tanaka, K. L et al., Chap. 11 in *Mars*, Kieffer et al. (ed.), 1992. [25] Hartmann, W.K. and G. Neukum, Space Sci. Rev., 96, 1-30, 2001. [26] Frey, E.L. et al., GSA Fall 2002 Meeting paper 26-2, 2002. [27] Hartmann, W.K., personal communication, 2002.